

Electrostatic Comb Drive for Resonant Sensor and Actuator Applications

By

William Chi-Keung Tang

**B.S. (University of California) 1980
M.S. (University of California) 1982**

DISSERTATION

Submitted in partial satisfaction of the requirements for the degree of

DOCTOR OF PHILOSOPHY

in

**ENGINEERING
ELECTRICAL ENGINEERING AND COMPUTER SCIENCES**

in the

GRADUATE DIVISION

of the

UNIVERSITY OF CALIFORNIA at BERKELEY

Approved:

Chair:

Roger T. Howe November 21, 1990 . . .

Albert P. Pisano Date 21 Nov. 90 . . .

R. M. White 21 Nov. 90 . . .

Electrostatic Comb Drive
for
Resonant Sensor and Actuator Applications

Copyright © 1990

William Chi-Keung Tang

ELECTROSTATIC COMB DRIVE

FOR

RESONANT SENSOR AND ACTUATOR APPLICATIONS

by

William Chi-Keung Tang

ABSTRACT

Interdigitated finger (comb) structures are demonstrated to be effective for electrostatically exciting the resonance of polycrystalline-silicon (polysilicon) microstructures parallel to the plane of the substrate. Linear plates suspended by a pair of folded-cantilever truss as well as torsional plates suspended by spiral and serpentine springs are fabricated from a 2 μm -thick phosphorus-doped low-pressure chemical-vapor deposited (LPCVD) polysilicon film. Three experimental methods are used to characterize quasi-static and resonant motions: microscopic illumination, observation with a scanning-electron microscope (SEM), and capacitive sensing using a frequency-modulation technique. Resonant frequencies of the laterally-driven structures range from 8 kHz to 80 kHz and quality factors range from 20 to 130 at atmospheric pressure, to about 50,000 in vacuum (10^{-7} torr). For linear structures suspended with compliant springs, a static electro-mechanical transfer function of $40 \text{ nm}\cdot\text{V}^{-2}$ is demonstrated. Resonant vibration amplitudes of up to 20 μm peak-to-peak are observed.

First-order mechanical theory is found to be adequate for calculating spring constants and resonant frequencies, using a Young's modulus between 140 and 150 GPa and neglecting residual strain in the released structures. Finger gap is found to have a more pronounced effect on comb characteristics than finger width or length, as expected from simple theory. A finite-element program is used to simulate the vertical levitation associated with the comb drive. This phenomenon is due to electrostatic repulsion by image charges mirrored in the ground plane beneath the suspended structure and is characterized as an electrostatic spring. As a result, the applied dc bias modulates the vertical resonant frequency. By electrically isolating alternating drive-comb fingers and applying voltages of equal magnitude and opposite sign, levitation can be reduced by an order of magnitude, while reducing the lateral drive force by less than a factor of two. These results agree well with first-order theory incorporating results from finite-element simulation.

A two-dimensional manipulator based on an orthogonally coupled comb-drive pair is designed and analyzed for use with a resonant micromotor and a microdynamometer. These devices can be fabricated and tested with the same technology and methods as the basic comb-drive structures.

Approved by Roger T. Howe
Committee Chairman

DEDICATION

To our parents

and

the memory of my father.

ACKNOWLEDGEMENTS

The successful completion of this thesis critically depends on the countless contributions from people throughout my academic life, including my formative years as an undergraduate at Berkeley. I am forever in debt to the many who provided me with friendship and comradeship, whom I cannot acknowledge by their names here.

Prof. Roger T. Howe, my research advisor, has not only provided the necessary financial support and technical guidance, but has also inspired me with his broad vision on the field of micromechanics and his enthusiasm towards life. Without his invaluable encouragement and suggestions, this work would never be possible.

I am also grateful to the other professors at the Berkeley Sensor & Actuator Center, Prof. Richard S. Muller, Prof. Albert P. Pisano, and Prof. Richard M. White, whose expertise from different perspectives of engineering greatly enriched my intellectual development. My appreciation also goes to the many industrial members of BSAC, whose active interest and critical reviews on the subject stimulated major motivation to pursue the research in light of potential engineering applications.

I would like to thank many current and former BSAC students who gave much needed assistance to this project. Clark Nguyen helped with electrical characterization; Jon Bernstein suggested the modulation technique; Jeff Chang, Dave Schultz and Mike Judy shared laborious time looking through the microscope; Charles Hsu, Reid Brennen and Martin Lim kept me company in the microfabrication laboratory; Long-Sheng Fan,

Leslie Field, Carlos Mastrangelo and Yu-Chong Tai made many important suggestions on processing details; and Tanya Faltens assisted with the SEM testing. In addition, Richard Moroney, Bob Ried, Mike Judy, Charles Hsu and Leslie Field helped to make my job to manage the ever-growing student population in 373 Cory easier, especially in matters of sanitation, recycling and library organization.

I am proud of the Berkeley Microfabrication Laboratory staff, whose diligent efforts in maintaining and improving the performance of the many complicated equipments is instrumental not only to the completion of this project, but also to many forefront researches in other disciplines in the Department of EECS.

I thank my family, especially Victor, who labored hard during our difficult years as new immigrants to support my college education. My father-in-law Rev. Yuen has become one of the laymen who understand micromechanics through his constant concern for my graduate life. The fellowship I enjoyed from many friends was invaluable in maintaining a balanced life, especially the time I spent with Albert and Liz Mak, Kelvin and May Chau, Alein and Melissa Chun, René Chun, Velda Mark, Kevin Chan, Ivan Chiang and Tony Chan.

Lastly and most importantly I thank my wife Pauline for her genuine understanding and encouragement when I had to spend long nights in the lab. She took care of my needs so I could concentrate on my work. When papers were due, she shared the tedious work of cutting and pasting. She is one of the other laymen who understand micromechanics through repeatedly listening to my practice talks. “Thanks,” from my heart!

TABLE OF CONTENTS

LIST OF FIGURES.....	vii
LIST OF TABLES.....	xiii
Chapter 1 INTRODUCTION	1
1.1 Sensors and Actuators for Micromechanical Systems	1
1.2 Vertical vs Lateral Drive Approaches.....	4
1.3 Dissertation Outline	9
Chapter 2 THEORY OF ELECTROSTATIC COMB DRIVE	10
2.1 Lateral Mode of Motion.....	11
2.1.1 Lateral-Mode Linearity of Comb Drive	11
2.1.2 Finite-Element Simulation of $\partial C/\partial x$	11
2.1.3 Transfer Function.....	16
2.2 Vertical Mode of Motion	22
2.2.1 Origin of Induced Vertical Motion.....	22
2.2.2 Finite-Element Simulation	27
2.2.3 Vertical Transfer Function	32
2.2.4 Vertical Resonant Frequency.....	33
2.2.5 Levitation Control Method.....	39
2.3 Mechanical Analysis	42
2.3.1 Linear Lateral Resonant Structures.....	42
2.3.1.1 Spring Constant of Folded-Beam Support.....	44
2.3.1.2 Spring Constant of Double-Folded Beams	50
2.3.1.3 Lateral Resonant Frequency	53
2.3.1.4 Quality Factor.....	57
2.3.2 Torsional Lateral Resonant Structures.....	59
2.3.2.1 Spiral Support.....	61
2.3.2.2 Serpentine Support.....	61
2.3.2.3 Resonant Frequency and Quality Factor.....	63

2.4	Summary.....	65
Chapter 3	LATERAL STRUCTURE FABRICATION	66
3.1	Fabrication Sequence	66
3.2	Fabrication Characteristics and Performance	74
3.2.1	Thin-Film Stress Consideration and Control Method	74
3.2.2	Thin-Film Etching and Vertical Sidewalls	79
3.2.3	Single-Mask Process	83
3.3	Summary.....	87
Chapter 4	TESTING TECHNIQUES AND RESULTS	88
4.1	Testing Techniques	89
4.1.1	Direct Observations.....	89
4.1.2	Electrical Testing	94
4.2	Microstructural Parameters.....	99
4.2.1	Thickness of Deposited Polysilicon Film	99
4.2.2	Plasma-Etching Results.....	101
4.3	Lateral-Mode Measurements.....	104
4.3.1	Resonant Frequencies and Young's Modulus.....	107
4.3.2	Lateral-Mode Quality Factors	109
4.3.3	Capacitance Gradient, $\partial C/\partial x$	115
4.4	Vertical-Mode Measurements.....	119
4.4.1	DC Levitation Results	123
4.4.2	Vertical and Lateral Drive Capacities.....	129
4.4.3	Vertical Resonant Frequencies.....	131
4.5	Summary.....	134
Chapter 5	ACTUATOR APPLICATION EXAMPLE	135
5.1	Two-Dimensional Manipulator	135
5.2	Resonant Micromotor Application	138
5.3	Stability and Design Considerations	143
5.4	Summary.....	150

Chapter 6 CONCLUSIONS	151
6.1 Evaluation of Thin-Film Electrostatic-Comb Drive.....	151
6.2 Scaling Consideration and Alternative Process	153
6.3 Future Research.....	155
REFERENCES.....	156
Appendix A PROCESS FLOW.....	164
Appendix B C-PROGRAMMING SOURCE CODES.....	176
B.1 Manhattan Archimedean Spiral	176
B.2 Rotated-Box Archimedean Spiral.....	182
B.3 Rotated-Box Concentric Comb Drive.....	188
B.4 Manhattan Lateral Comb Drive.....	196
B.5 Manhattan-to-Rotated-Box Conversion.....	201
B.6 Rotated-Box Sawtooth.....	206

LIST OF FIGURES

Chapter 1

1.1	A typical electrostatically excited microbridge.	4
1.2	A microbridge with vertical differential drive.	6
1.3	Layout of a linear lateral resonator.	7

Chapter 2

2.1	Electric field distribution in a comb-finger gap.....	12
2.2	Electric field distribution after the movable finger displaces by Δx into the slot.	12
2.3	Cross section of a movable comb finger with two adjacent electrodes and an underlying ground plane for electrostatic simulation.	13
2.4	Simulated $\partial C/\partial x$ vs g at different h , with $w = 4 \mu\text{m}$ and $d = 2 \mu\text{m}$	14
2.5	A linear resonator electrostatically driven from one side and sensed capacitively at the other side.....	17
2.6	A conceptual pawl-ratchet resonant motor using the comb drive as the actuating element.	23
2.7	Cross section of the ratchet wheel and pawl tip after unbalanced levitation force is induced on the comb structure.....	24
2.8	Cross section of the potential contours (dashed) and electric fields (solid) of a comb finger under levitation force induced by two adjacent electrodes.	26
2.9	<i>Maxwell</i> output showing potential contours at $z = 0$	28
2.10	<i>Maxwell</i> output at $z = 1 \mu\text{m}$	29

2.11	<i>Maxwell</i> output at $z = 2 \mu\text{m}$	30
2.12	Simulated F_z vs z at different V_P . F_z is normalized to per-comb-finger (finger dimensions: $h = g = 2 \mu\text{m}$, $w = 4 \mu\text{m}$).....	31
2.13	The vertical forces acting on a movable comb finger.....	32
2.14	Theoretical levitation (z) vs V_P on dimensionless axes. The scales on each axis are to be fitted to experimental results.....	34
2.15	Theoretical frequency ratio ω_l / ω_0 vs V_P on dimensionless axes. The scales on each axis are to be fitted to experimental results.....	38
2.16	Cross section of the potential contours (dashed) and electric fields (solid) around a movable comb finger when differential bias is applied to the two adjacent electrodes.....	40
2.17	Potential contours (dashed) and electric fields (solid) around a movable comb finger when differential bias is applied to the two adjacent electrodes and the striped ground conductors.....	40
2.18	Crossover layout for electrical isolation of alternating drive electrodes.....	41
2.19	Layout of a linear resonant structure supported by a pair of folded-beam suspensions.....	43
2.20	Mode shape of a folded-beam support when the resonant plate is displaced by X_0 under a force of F_x	44
2.21	Mode shape of segment [AB].....	45
2.22	Cross section of a beam as a result of nonideal plasma-etching process for polysilicon.....	47
2.23	Crab-leg flexure design [47].....	50
2.24	Resonant structure suspended by a pair of double-folded beams.....	51
2.25	Mode shape of a double-folded suspension when the resonant plate is displaced by X_0 under a force of F_x	52

2.26	Major dissipative processes of a laterally-driven resonant plate.	58
2.27	Layout of a torsional resonator with two spirals.....	60
2.28	Dimensions of the serpentine spring.	62

Chapter 3

3.1	Process sequence of a lateral resonant structure.	67
3.2	SEM of a linear resonator with 140 μm -long folded beams.	69
3.3	Optical micrograph of the alternating-comb structure with striped ground conductors underneath the comb fingers.....	70
3.4	SEM of the alternating-comb drive showing the crossover structure.....	70
3.5	SEM of the close-up view of the crossover structure.....	71
3.6	SEM of the close-up view of the linear comb-drive fingers, showing the surface topography of the deposited polysilicon film.	71
3.7	SEM of two, two-turn Archimedean spirals supporting a torsional resonant plate.....	72
3.8	SEM of one of the four serpentine springs supporting a torsional resonant plate.....	72
3.9	SEM of the concentric comb structure.....	73
3.10	SEM of a structure supported by a pair of double-folded beams.	73
3.11	SEM of a constrained structure fabricated without stress anneal.	75
3.12	SEM of a set of clamped-clamped diagnostic bridges, each beam is 10 μm wide and 2 μm thick, with the length varying from 100 μm to 300 μm	75

3.13	Optical micrograph of a set of diagnostic microbridges from an unannealed wafer. Nomaski illumination reveals that bridges 120 μm and longer are buckled.....	77
3.14	Optical micrograph of a set of microbridges from an annealed wafer. Nomaski illumination shows a buckling length of 220 μm	77
3.15	Optical micrograph of a wafer with PSG blistering on top of silicon-rich nitride as a result of one-hour annealing at 1050°C.....	78
3.16	Cross section of the comb fingers as a result of nonideal plasma etching, reducing the drive efficiency.....	79
3.17	Optical micrograph of a structure with enlarged anchors as a result of wet etching.....	82
3.18	Single-mask processing steps.....	84
3.19	Layout of a single-mask resonator.....	85

Chapter 4

4.1	Test setup for a linear resonator.....	90
4.2	Test setup for a torsional resonator.....	91
4.3	Test setup using an SEM.....	93
4.4	Electrical test setup with modulation technique.....	96
4.5	Electrical test setup using frequency-doubling effect.....	97
4.6	Position of the wafers inside the LPCVD polysilicon tube.....	100
4.7	SEM of a microstructure etched with excessive energy.....	102
4.8	SEM of a microstructure etched with insufficient energy.....	102
4.9	SEM of a microstructure etched with optimum energy.....	103
4.10	Comb-structure dimensions.....	104

4.11	Measured and calculated Q vs beam length.....	110
4.12	Q vs finger gap.....	112
4.13	SEM of a vibrating structure under high vacuum (10^{-7} torr).....	113
4.14	Time- and frequency-domain methods for Q evaluation.....	114
4.15	Measured and calculated values of the transfer functions.....	116
4.16	$\partial C/\partial x$ vs. finger gap.....	117
4.17	Optical micrograph of prototype V1 with 15 drive fingers.....	121
4.18	Optical micrograph of prototype V2 with 13 drive fingers.....	122
4.19	Optical micrograph of prototype V4 with 12 drive fingers.....	122
4.20	Levitation as a result of a common voltage applied to all electrodes.....	124
4.21	SEM of a V2 prototype comb levitated under 10 V dc bias. Note that the drive fingers, because of the positive bias, appear darkened in the SEM.....	125
4.22	The three forces acting on the movable comb finger.....	125
4.23	Measured and calculated levitation for prototype V1.....	127
4.24	Vertical displacement of prototype V1 for varying voltage on one electrode from -15 V to +15 V, while holding the other electrode fixed at +15 V.....	128
4.25	SEM of prototype V1 under ± 10 V balanced biasing on the alternating drive fingers, indicating almost no levitation. Fingers at higher potentials appear darkened due to voltage-contrast effect in SEM.....	129
4.26	SEM of prototype V1 driven into vertical resonance under a 50 mV ac drive on top of a 5 V dc bias.....	131

4.27	Measured and fitted vertical resonant frequencies of prototype V1 as a function of dc bias.....	132
------	-------------------------------------------------------------------------------------------------	-----

Chapter 5

5.1	Basic design of an orthogonally coupled comb-drive pair to form a two-dimensional manipulator.....	136
5.2	Resonant-structure micromotor concept [30].	139
5.3	Resonant micromotor implemented with the comb drive as the actuating element.	140
5.4	Pawl and gear wheel in resting position.....	141
5.5	Pawl and gear wheel interference.....	141
5.6	Improved pawl-ratchet engagement with elliptical pawl motions.....	142
5.7	Modified resonant micromotor with differential elliptical drives.....	143
5.8	Push-pull comb-drive actuator.....	145
5.9	Mode shape of an orthogonally coupled serpentine spring pair under a force F_x	146
5.10	Microdynamometer with Archimedean spiral supports.	149

LIST OF TABLES

2.I	Adjusted α and β at different h	15
2.II	Simulation results of serpentine springs with $W_m = 28 \mu\text{m}$, and a $2 \mu\text{m} \times 2 \mu\text{m}$ cross section.....	63
2.III	Simulation results of serpentine springs with $N_m = 8$ at different $W_m [\mu\text{m}]$	63
4.I	Polysilicon film thickness profile	99
4.II	Polysilicon film thickness profile from a two-step deposition experimental run	100
4.III	Comb drive features of types A and B, with comb width = $4 \mu\text{m}$, length = $40 \mu\text{m}$, overlap = $20 \mu\text{m}$	105
4.IV	Type C comb dimensions	106
4.V	Predicted and measured resonant frequencies of prototypes A and B	107
4.VI	Predicted and measured resonant frequencies of the torsional structures.....	107
4.VII	Predicted and measured resonant frequencies of the C-series prototypes	108
4.VIII	Different comb designs for levitation control.....	121
4.IX	Normalized γ_z and γ_x per drive finger for V-series prototypes	130

Chapter 1

INTRODUCTION

1.1 SENSORS AND ACTUATORS FOR MICROMECHANICAL SYSTEMS

In the past decade, the application of bulk- and surface-micromachining techniques greatly stimulated research in micromechanical structures and devices [1–5]. Advancements in this field are motivated by potential applications in batch-fabricated integrated sensors and silicon microactuators. These devices promise new capabilities, as well as improved performance-to-cost ratio over conventional hybrid sensors. Micromachined transducers that can be fabricated compatibly with an integrated circuit process are the building blocks for integrated microsystems with added functionality, such as closed-loop control and signal conditioning. Furthermore, miniaturized transducers are powerful tools for research in the micron-sized domain in the physical, chemical and biomedical fields.

As one class of microactuators, rotary electrostatic micromotors have been studied extensively over the past several years [6–9]. They have served as vehicles for research on friction and electrostatic control and modelling techniques in the micron-sized domain. Another class of microactuators includes deformable diaphragms, such as those used in micropumps and microvalves [10–15]. The diaphragms are actuated perpendicular to the surface of the silicon substrate, using an embedded piezoelectric film [13], electrostatic

forces [14], or thermal expansion [11, 15]. These devices can easily be made an order of magnitude smaller than the conventionally manufactured pumps and valves, and thus can be potentially applied in the biomedical field.

Integrated-sensor research is rigorously pursued because of the broad demand for low-cost, high-precision, and miniature replacements for existing hybrid sensors. In particular, resonant sensors are attractive for precision measurements because of their high sensitivity to physical or chemical parameters and their frequency-shift output. These devices utilize the high sensitivity of the frequency of a mechanical resonator to physical or chemical parameters that affect its potential or kinetic vibrational energy [16–19]. Existing hybrid resonant sensors include quartz mechanical resonators [19, 20], quartz bulk-wave resonators [21, 22], and surface-acoustic-wave oscillators [23, 24]. Resonant microsensors promise better reproducibility through well-controlled material properties and precise matching of micromachined structures. Furthermore, batch fabrication with existing IC technology should reduce manufacturing cost of resonant microsensors. Microfabricated resonant structures for sensing pressure [25–27], acceleration [28], and vapor concentration [29] have been demonstrated.

Besides high-precision measurement, resonant structures can also be used as actuators. An example is the resonant-structure micromotor concept, where a tuning-fork-like resonator is used to turn a gear wheel with the vibrational energy [30]. Mechanical vibration of microstructures can be excited in several ways, including piezoelectric films [25], thermal expansion [28, 31], electrostatic forces [16, 26, 32, 33], and magnetostatic

forces [27]. Vibration can be sensed by means of piezoelectric films [25], piezoresistive strain gauges [31], optical techniques [31, 33, 34], and capacitive detection [16, 26, 29, 32]. Electrostatic excitation combined with capacitive (electrostatic) detection is an attractive approach for silicon microstructures because of simplicity and compatibility with micromachining technology [16, 17].

1.2 VERTICAL vs LATERAL DRIVE APPROACHES

Previous resonant microstructures are typically driven vertically; i.e., in a direction perpendicular to the silicon substrate. Figure 1.1 illustrates a vertically-driven microbridge made of deposited polysilicon film. The bridge is typically 1 to 2 μm thick, and is separated from the underlying electrode and the substrate by a distance of 1 to 2 μm . Vibration is excited in the z direction electrostatically with the bridge forming a parallel-plate-capacitor drive with the underlying electrode. Motion can be detected electrostatically by sensing the change in capacitance.

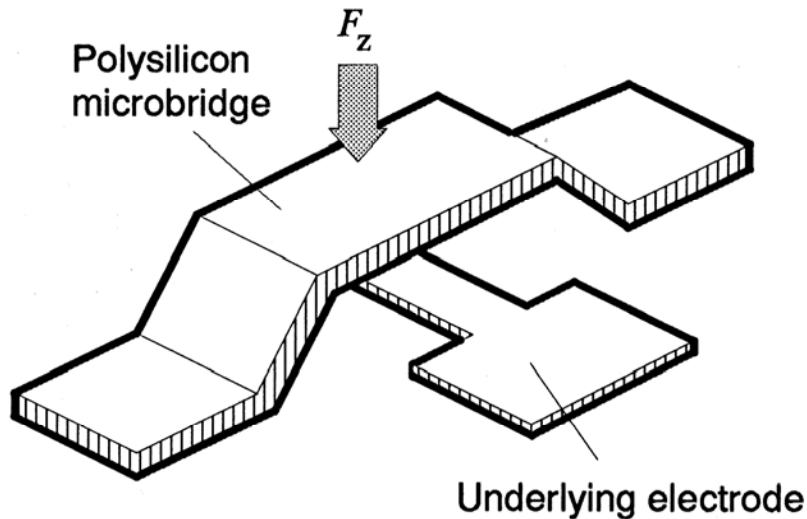


Figure 1.1 A typical electrostatically excited microbridge.

There are several drawbacks to the vertical driving and sensing of micromechanical structures. First, the electrostatic force is nonlinear unless the amplitude of vibration is limited to a small fraction of the capacitor gap. The electrostatic force in the z direction is given by

$$F_z = \frac{\partial E}{\partial z} = \frac{1}{2}V^2 \frac{\partial C}{\partial z} \quad (1.1)$$

where E is the stored energy in the capacitor, C is the capacitance, and V is the applied voltage. For an idealized parallel-plate capacitor, the capacitance is given by

$$C = \frac{\epsilon A}{z} \quad (1.2)$$

where ϵ is the permittivity, and A is the plate area. Therefore, $\partial C / \partial z$ is a nonlinear, time-dependent parameter; and thus the vibration amplitude must be limited to a small fraction of the average capacitor gap to maintain useful linearity. Frequency-jump phenomena have been observed when a microbridge is driven into large-amplitude oscillation [35].

Second, the quality factor Q of the resonance is very low at atmospheric pressure because of squeeze-film damping in the micron-sized capacitor gap [36, 37]. A quality factor limited only by internal damping in the bridge material can be obtained by resonating the structure in vacuum. However, in this case, the parallel-plate excitation is often so efficient that steady-state ac excitation voltages must be limited to the mV range. Such low voltage levels complicate the design of the sustaining amplifier [35]. Third, in actuator applications, it is difficult to mechanically couple small vertical motions to perform useful work. Adding vertical features leads to a complicated fabrication process

and yield loss due to mask-to-mask misalignment. For example, in order to drive a microbridge differentially, another electrode must be added on top of the bridge, as illustrated in Fig. 1.2. This involves two extra masking steps, one to pattern the anchor for the top electrode, and the other to pattern the top electrode itself.

Driving planar microstructures parallel to the substrate addresses the above problem [38–40]. The flexibility of planar design can be exploited to incorporate a variety of elaborate geometric structures, such as differential capacitive excitation and detection, without an increase in process complexity. Figure 1.3 shows the layout of a linear resonant structure which can be driven electrostatically from one side and sensed capacitively at the other side with interdigitated finger (comb) structures. Alternatively, the structure can be driven differentially (push-pull) using the two combs, with the motion

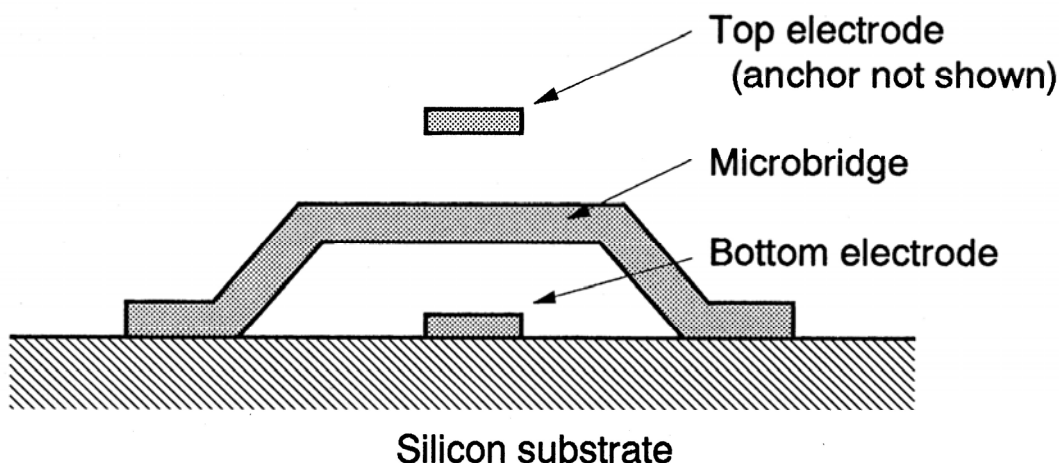


Figure 1.2 A microbridge with vertical differential drive.

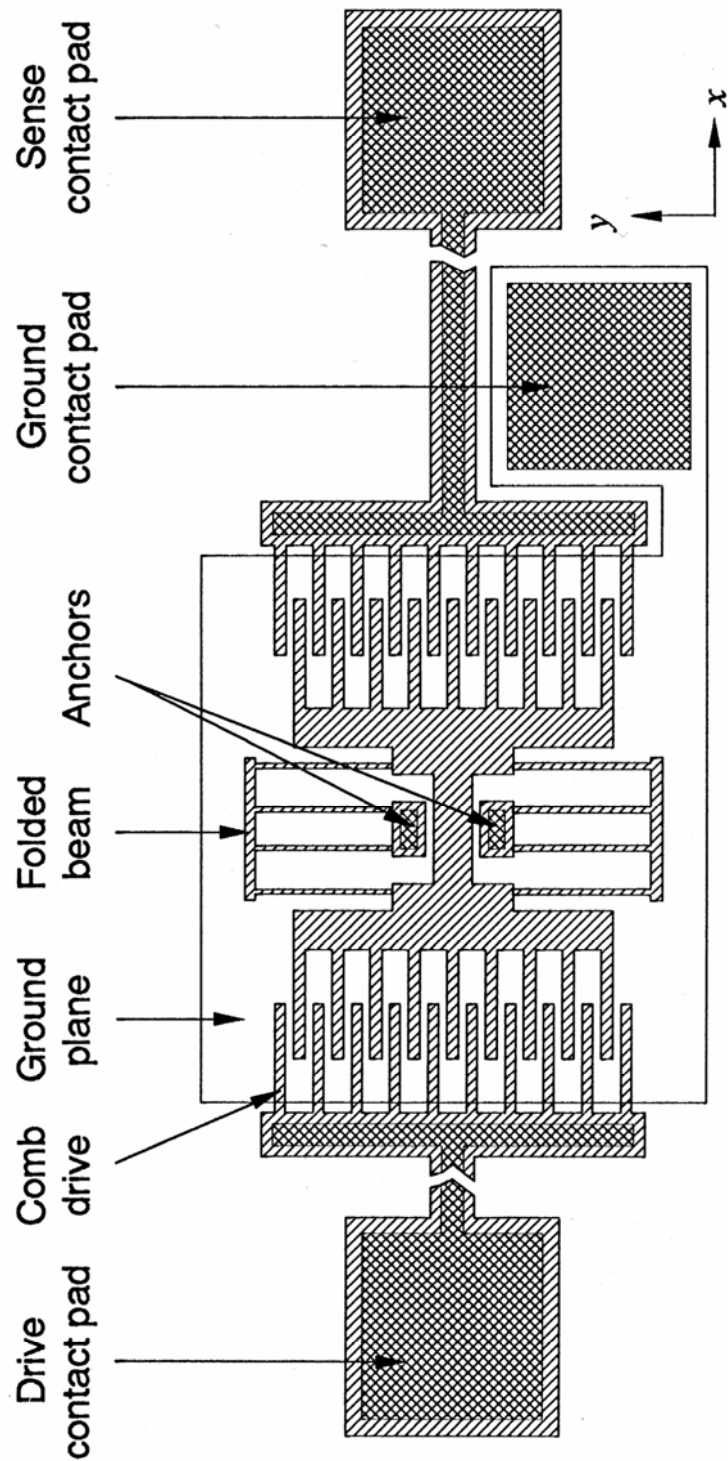


Figure 1.3 Layout of a linear lateral resonator.

sensed by the impedance shift at resonance [35]. The resonator is fabricated using deposited film and sacrificial layer technique. The resonant plate and the stationary electrodes are formed with a layer of 2 μm -thick deposited polysilicon film anisotropically etched from one masking step, eliminating mask-to-mask misalignment. The separation of the structure from the substrate is determined by the thickness of the sacrificial layer, which is typically 2 to 3 μm .

Another advantage of the laterally-driven structure is that the vibration amplitude can be of the order of 10 to 20 μm for certain comb and suspension designs, making them attractive for actuator applications. The use of weaker fringing fields to excite resonance is advantageous for high- Q structures (resonating in vacuum), since this results in larger steady-state ac excitation voltages. Furthermore, the quality factor for lateral vibration at atmospheric pressure is substantially higher than for vibration normal to the substrate [36, 37]. Couette flow in the gap between the structure and the substrate occurs for lateral motion of the structure, which is much less dissipative than squeeze-film damping.

1.3 DISSERTATION OUTLINE

The goal of this thesis is to establish a foundation for electrostatically exciting and sensing suspended micromachined transducer elements based on the comb-drive technology, with the perspectives on potential resonant sensor and actuator applications. In-depth theoretical studies and finite-element simulations on the normal lateral mode of operation as well as the vertical-mode behavior of the comb drive and spring suspensions are first presented. The surface-micromachining techniques employed in this study are then described, with a discussion of fabrication issues affecting the performance of the suspended resonators. Comparisons of the experimental results on static and dynamic behaviors of the resonant structures with theories on both the lateral and vertical characteristics are presented and evaluated, followed by the discussion of an example of applying the comb drive as an actuator. Finally, a discussion on the scaling issues of surface-micromachined comb drives leads to a consideration on potential future research.

Chapter 2

THEORY OF ELECTROSTATIC COMB DRIVE

Because of the inherent linearity of the electrostatic comb-drive structures, the analysis of the first-order 2-dimensional theory is relatively straightforward. In the previous chapter, we showed that the operation of the vertically-driven microbridge is nonlinear by discussing the time-dependent characteristics of the capacitance variation with respect to the direction of motion ($\partial C / \partial z$). In this chapter, we first establish the first-order linearity of the electrostatic comb drive in its normal lateral mode of motion by analyzing $\partial C / \partial x$ and then derive the lateral transfer function. Although we are mainly interested in the lateral-mode operation, vertical motions are frequently observed, and may serve significant purposes in certain applications [40]. In any case, it is desirable to control vertical motions while lateral motions are excited. We present the initial results of the electrostatic simulations of the vertical behavior of the comb drive with a 2-D finite-element program, which lead to the development of the first-order theory for the vertical mode of motion. Finally, a mechanical analysis of the spring suspensions for both linear and torsional resonators is presented, with special emphasis on the folded-beam design as an attractive suspension for linear resonant structures.

2.1 LATERAL MODE OF MOTION

2.1.1 Lateral-Mode Linearity of Comb Drive

The electrostatic-comb structure can be used either as a drive or a sense element [38].

The induced driving force and the output sensitivity are both proportional to the variation of the comb capacitance C with the lateral displacement x of the structure, $\partial C / \partial x$. A key feature of the electrostatic-comb drive is that $\partial C / \partial x$ is a constant independent of the displacement Δx , as long as Δx is less than the finger overlap. We can model the capacitance between the movable comb fingers and the stationary fingers as a parallel combination of two capacitors, one due to the fringing fields, C_f , and the other due to the normal fields, C_n (Figs. 2.1 and 2.2). Figure 2.2 illustrates the change in the field distribution after the comb finger in Fig. 2.1 is displaced into the slot between the two adjacent electrodes. By considering the difference between Figs. 2.1 and 2.2, it becomes obvious that C_f is independent of the displacement, Δx , while C_n is linearly proportional to Δx . In a more realistic 3-dimensional modelling, both C_f and C_n contain out-of-plane fringing fields. However, the argument for linearity remains the same. The fact that $\partial C / \partial x$ is independent of Δx will be referred to frequently in the transfer function analysis.

2.1.2 Finite-Element Simulation of $\partial C / \partial x$

The complete modelling of the electrostatic-comb structure requires the use of a 3-dimensional finite-element program. However, since we are interested in motions only on the x - y plane, we can reduce the problem to a 2-dimensional one.

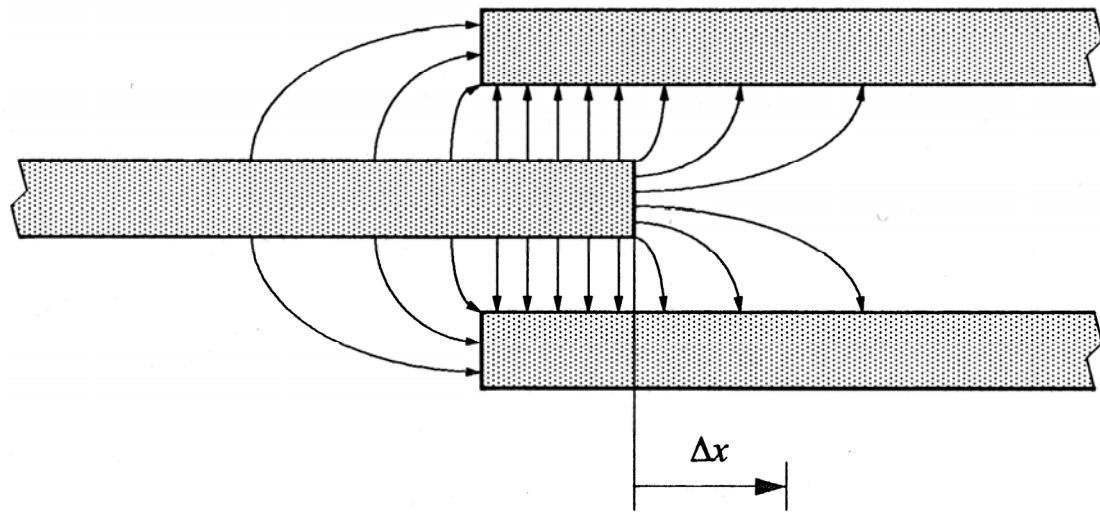


Figure 2.1 Electric field distribution in a comb-finger gap.

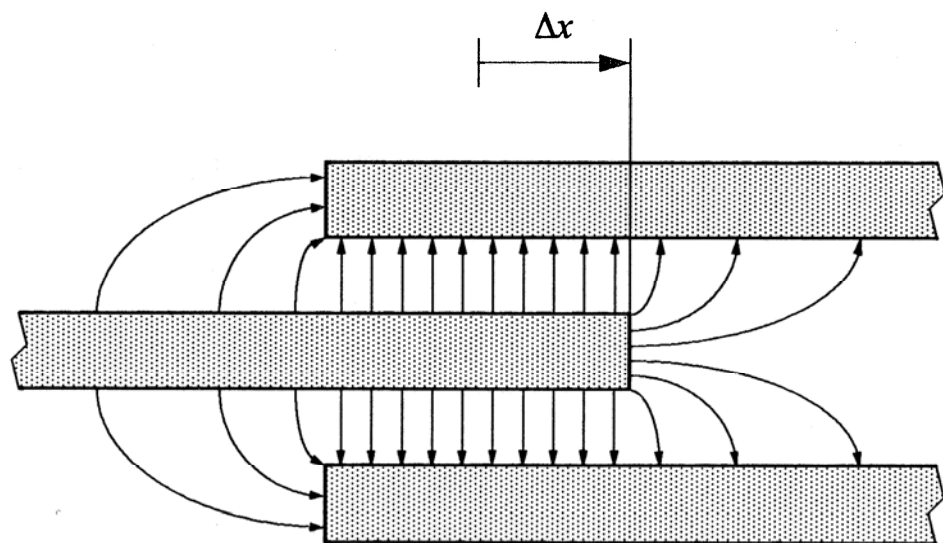


Figure 2.2 Electric field distribution after the movable finger displaces by Δx into the slot.

In this approach, we use the 2-D electrostatic package *Maxwell* [41] to simulate the cross section along the y - z plane through the comb fingers, as shown in Fig. 2.3. The output of the simulation is the per-unit-length capacitance between the comb finger and the two adjacent electrodes. The results are the capacitance gradient $\partial C / \partial x$, the capacitance for a given unit length (along the x direction) of the comb fingers as a function of the finger width (w), finger thickness (h), finger gap (g), and separation from the substrate ground plane (d). The most significant results are plotted in Fig. 2.4.

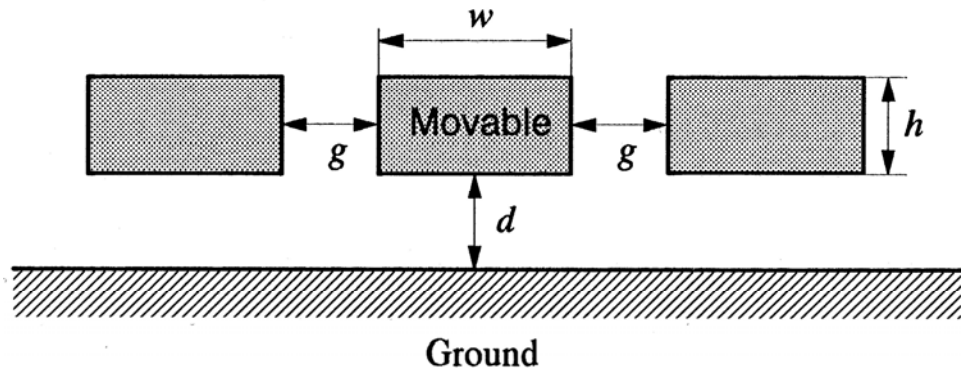


Figure 2.3 Cross section of a movable comb finger with two adjacent electrodes and an underlying ground plane for electrostatic simulation.

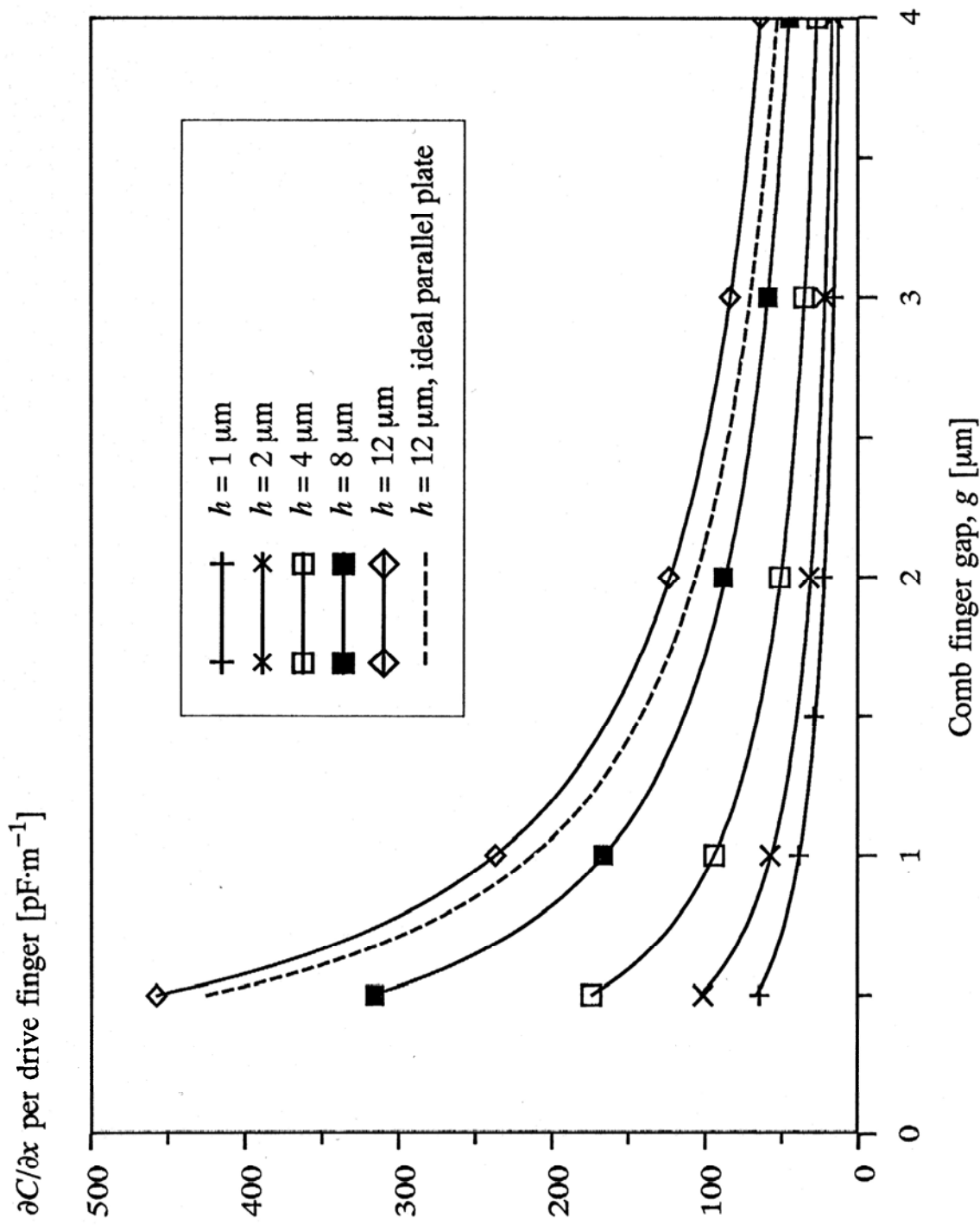


Figure 2.4 Simulated $\partial C / \partial x$ vs. g at different h , with $w = 4\text{ }\mu\text{m}$ and $d = 2\text{ }\mu\text{m}$.

Although the 2-D simulation results may not be numerically accurate, nevertheless, it provides some qualitative insights. In particular, $\partial C / \partial x$ changes substantially with h and $g^{-\beta}$. The curves at different values of h in Fig. 2.4 are obtained by fitting with the following equation to the simulation points, with α and β as the adjustable parameters:

$$\frac{\partial C}{\partial x} = 2\alpha\epsilon hg^{-\beta} \quad (2.1)$$

where ϵ is the permittivity, with a value of $8.854 \text{ pF}\cdot\text{m}^{-1}$ used in the simulation. The adjusted values of α and β are listed in Table 2.I below.

Table 2.I Adjusted α and β at different h

	$h = 1 \mu\text{m}$	$h = 2 \mu\text{m}$	$h = 4 \mu\text{m}$	$h = 8 \mu\text{m}$	$h = 12 \mu\text{m}$
α	2.19	1.61	1.33	1.17	1.12
β	0.78	0.85	0.89	0.93	0.95

When the value of h is increased to over $8 \mu\text{m}$, both α and β approach 1, as expected of a parallel combination of two identical, idealized parallel-plate capacitors. The presence of the ground plane at $2 \mu\text{m}$ distance ($d = 2 \mu\text{m}$) weakens $\partial C / \partial x$ by roughly 30% for the nominal $h = 2 \mu\text{m}$; while varying the finger width to any value over $1 \mu\text{m}$ has little effect on $\partial C / \partial x$. In order to obtain an efficient comb drive, a large $\partial C / \partial x$ is desirable, and can be achieved by designing dense comb fingers with narrow finger gaps from thick polysilicon films.

2.1.3 Transfer Function

With the linearity and $\partial C / \partial x$ established, we now proceed with the derivation of the lateral transfer function. The linear resonator shown in Fig. 1.3 can be driven electrostatically with the comb structure from one side and sensed capacitively at the other side as illustrated in Fig. 2.5. Alternatively, the structure can be driven differentially (push-pull) using the two combs, with the motion sensed by the impedance shift at resonance [35]. In analyzing the electromechanical transfer function, we consider the former, two-port configuration.

At the drive port, the induced electrostatic force in the x direction, F_x , is given by

$$F_x = \frac{1}{2} \frac{\partial C}{\partial x} v_D^2 \quad (2.2)$$

where v_D is the drive voltage across the structure and the stationary drive electrode. For a drive voltage $v_D(t) = V_p + v_d \sin(\omega t)$, where V_p is the dc bias at the drive port and v_d is the ac drive amplitude, Eq. (2.2) becomes

$$\begin{aligned} F_x &= \frac{1}{2} \frac{\partial C}{\partial x} \left[V_p^2 + 2V_p v_d \sin(\omega t) + v_d^2 \sin^2(\omega t) \right] \\ &= \frac{1}{2} \frac{\partial C}{\partial x} \left[V_p^2 + \frac{1}{2} v_d^2 + 2V_p v_d \sin(\omega t) - \frac{1}{2} v_d^2 \cos(2\omega t) \right] \end{aligned} \quad (2.3)$$

Note that the right-hand side of this equation is a constant plus a sum of two harmonic functions. Given the system spring constant in the x direction, k_x , and a damping factor, c ,

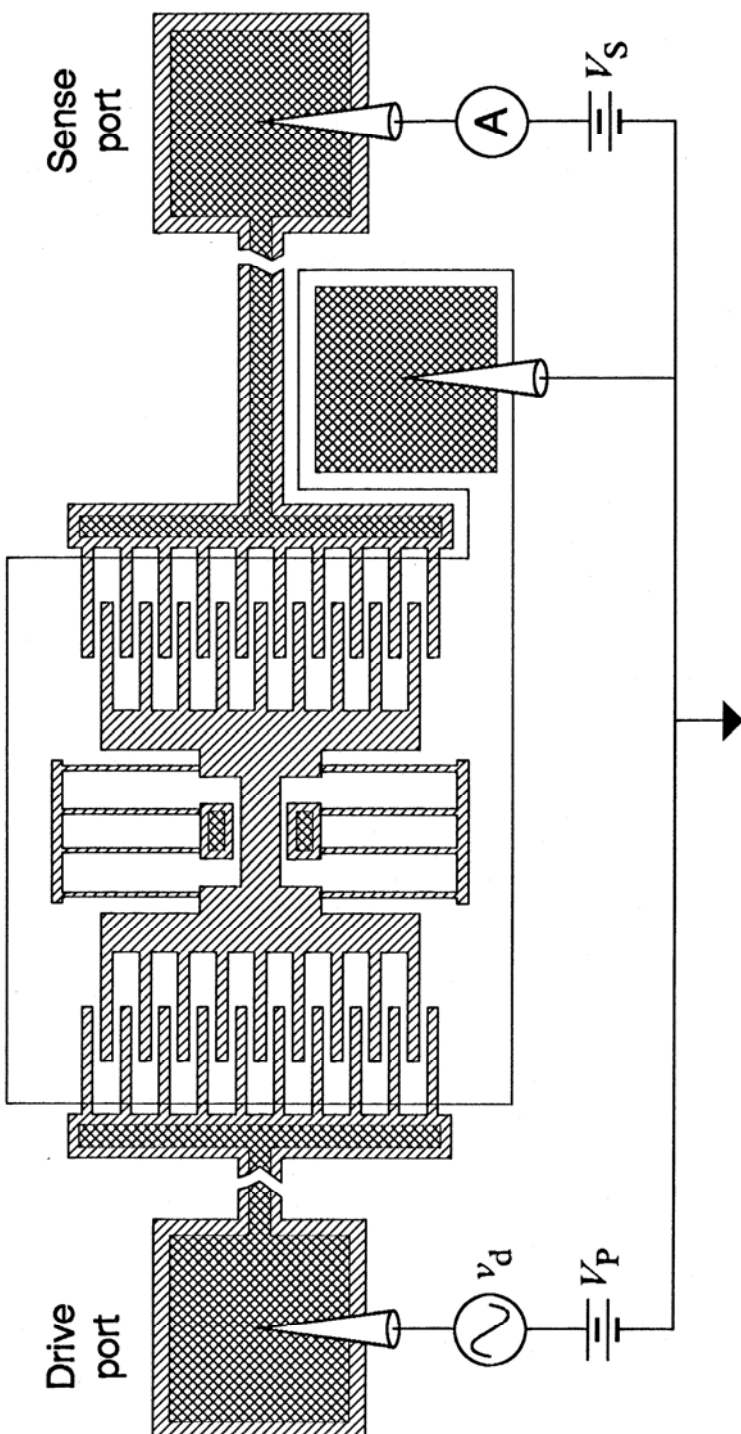


Figure 2.5 A linear resonator electrostatically driven from one side and sensed capacitively at the other side.

the equation of motion is a second-order-differential equation given by

$$M\ddot{x} + c\dot{x} + k_x x = F_x(t) \quad (2.4)$$

where M is the effective mass of the structure. Using the principle of superposition, the steady-state solution of Eq. (2.4) is the sum of the steady-state solutions of the following equations [42]:

$$M\ddot{x} + c\dot{x} + k_x x = \frac{1}{2} \frac{\partial C}{\partial x} \left(V_p^2 + \frac{1}{2} v_d^2 \right) \quad (2.5)$$

$$M\ddot{x} + c\dot{x} + k_x x = \frac{\partial C}{\partial x} V_p v_d \sin(\omega t) \quad (2.6)$$

$$M\ddot{x} + c\dot{x} + k_x x = -\frac{1}{4} \frac{\partial C}{\partial x} v_d^2 \cos(2\omega t) \quad (2.7)$$

Therefore, the steady-state response is given by

$$\begin{aligned} x(t) &= \frac{1}{2k_x} \frac{\partial C}{\partial x} \left(V_p^2 + \frac{1}{2} v_d^2 \right) \\ &+ \frac{(\partial C / \partial x) V_p v_d}{\sqrt{(k_x - M \omega^2)^2 + c^2 \omega^2}} \sin(\omega t - \phi_1) \\ &- \frac{(\partial C / \partial x) v_d^2}{4\sqrt{(k_x - 4M \omega^2)^2 + 4c^2 \omega^2}} \cos(2\omega t - \phi_2) \end{aligned} \quad (2.8)$$

where

$$\phi_1 = \tan^{-1} \left(\frac{c\omega}{k_x - M\omega^2} \right), \text{ and } \phi_2 = \tan^{-1} \left(\frac{2c\omega}{k_x - 4M\omega^2} \right) \quad (2.9)$$

The second-harmonic term on the right-hand side of the solution is negligible if $v_d \ll V_p$.

Furthermore, if a push-pull drive is used, the second term on the right-hand side of Eq. (2.3) results in a common-mode force, and is canceled to first order. With the complementary drive voltage $v_{D-}(t) = V_p - v_d \sin(\omega t)$ applied to the opposing comb, F_x becomes

$$\begin{aligned} F_x &= \frac{1}{2} \frac{\partial C}{\partial x} (v_D^2 - v_{D-}^2) \\ &= 2 \frac{\partial C}{\partial x} V_p v_d \sin(\omega t) \end{aligned} \quad (2.10)$$

In this case, the steady-state response in x is a simple harmonic function given by

$$x(t) = \frac{2(\partial C / \partial x)V_p v_d}{\sqrt{(k_x - M\omega^2)^2 + c^2\omega^2}} \sin(\omega t - \phi_1) \quad (2.11)$$

The motion is sensed by detecting the short-circuit current through the time-varying comb capacitor with a dc bias [16]. At the sense port, harmonic motion of the structure in Fig. 2.5 results in a sense current, i_s , which is given by

$$i_s = V_s \frac{\partial C}{\partial x} \cdot \frac{\partial x}{\partial t} \quad (2.12)$$

where V_s is the bias voltage between the structure and the stationary sense electrode.

Finally, the transconductance of the resonant structure is defined by $G(j\omega) = I_S / V_d$.

Substituting the time derivative of Eq. (2.8) into Eq. (2.12), we can express the output i_s in terms of the input v_d :

$$\begin{aligned} i_s(t) &= \frac{(\partial C / \partial x)^2 V_p V_s v_d \omega}{\sqrt{(k_x - M \omega^2)^2 + c^2 \omega^2}} \cos(\omega t - \phi_1) \\ &\quad + \frac{(\partial C / \partial x)^2 V_s v_d^2 \omega}{2 \sqrt{(k_x - 4M \omega^2)^2 + 4c^2 \omega^2}} \sin(2\omega t - \phi_2) \end{aligned} \quad (2.13)$$

At this point, we simplify the analysis by assuming $v_d \ll V_p$, and thus the second-harmonic term can be ignored. Therefore,

$$G(j\omega t) = \frac{(\partial C / \partial x)^2 V_p V_s \omega}{\sqrt{(k_x - M \omega^2)^2 + c^2 \omega^2}} e^{j(\omega t - \phi)} \quad (2.14)$$

The magnitude of $G(j\omega t)$ is doubled for the case of a push-pull drive. At mechanical resonance, $\omega^2 = \omega_r^2 = k_x / M$, and the magnitude of the transconductance is evaluated to be

$$|G(j\omega_r t)| = \omega_r V_p V_s \frac{Q}{k_x} (\partial C / \partial x)^2 \quad (2.15)$$

where Q is the quality factor of the system, and is given by [42]

$$Q = \frac{k_x}{c \omega_r} \quad (2.16)$$

The value of $(\partial C / \partial x)$ of the resonators can be evaluated experimentally by measuring

the quality factor and the transconductance at resonance and substituting the results in Eq. (2.15).

2.2 VERTICAL MODE OF MOTION

One of the potential applications of lateral resonators actuated with the electrostatic comb drive is resonant microactuators [30]. Figure 2.6 illustrates a schematic surface-micromachined resonant micromotor based on a pawl-ratchet mechanism. For efficient mechanical coupling between the vibrating pawl and the toothed wheel, it is essential that both structures remain co-planar. However, 2 μm -thick polysilicon resonators with compliant folded-beam suspensions have been observed to levitate over 2 μm when driven by an electrostatic comb biased with a dc voltage of 30 V. The comb levitation results in an unbalanced upward force applied to one side of the folded-beam suspension, causing the pawl tip to deflect downward and to miss the ratchet wheel completely. Figure 2.7 shows a possible outcome if the comb is levitated by more than the thickness of the polysilicon film. This effect must be understood in order to design functioning resonant microactuators, with the possibility that levitation by the comb structures may offer a convenient means for selective pawl engagement.

In this section, the electrostatic forces responsible for levitation are analyzed, along with the discussion of the modified comb design with independently biased fingers for levitation control.

2.2.1 Origin of Induced Vertical Motion

Levitation phenomenon of the comb-drive structure is due to electrostatic repulsion by image charges mirrored in the ground plane beneath the suspended structure. The ground

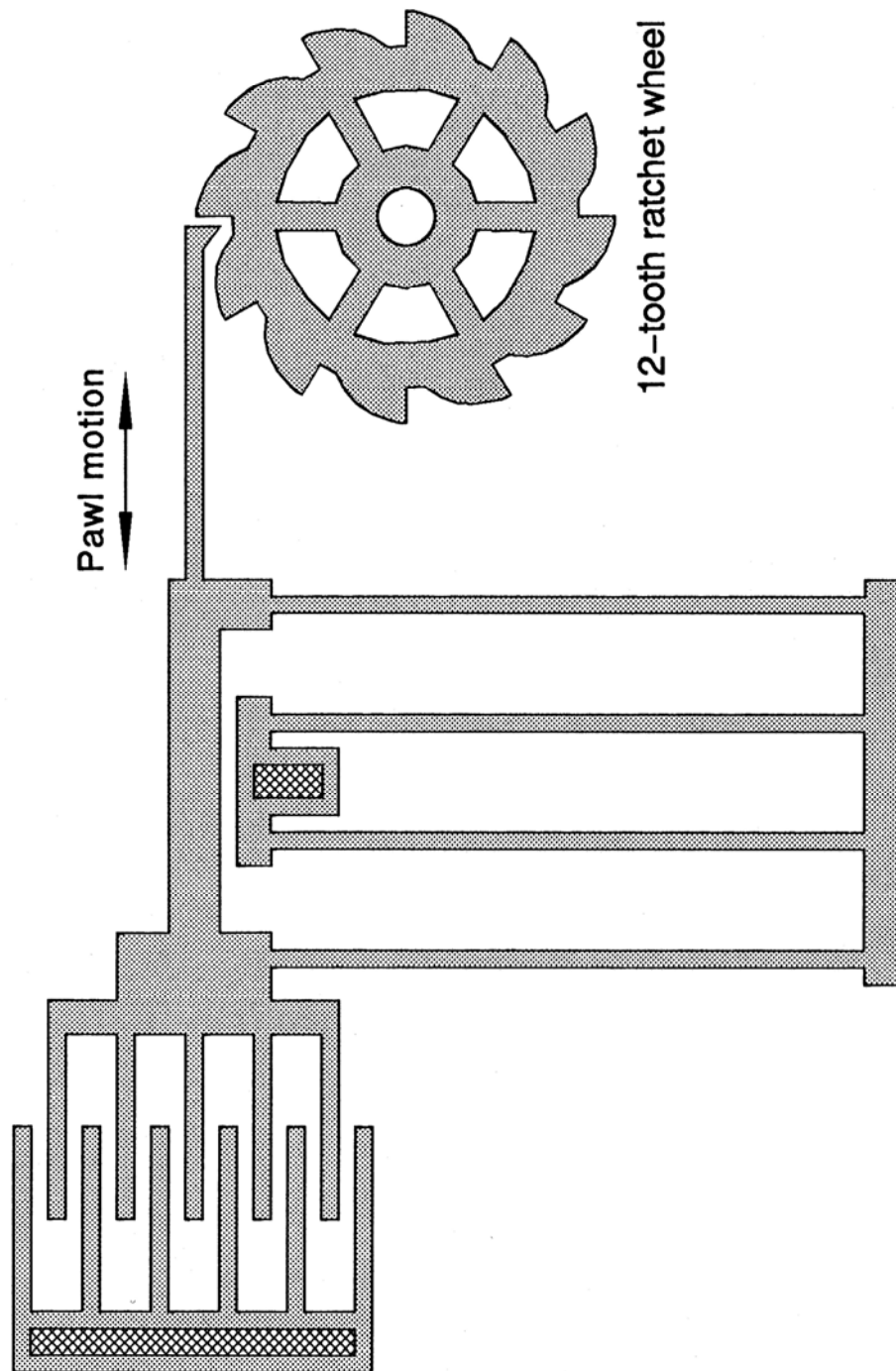


Figure 2.6 A conceptual pawl-ratchet resonant motor using the comb drive as the actuating element.

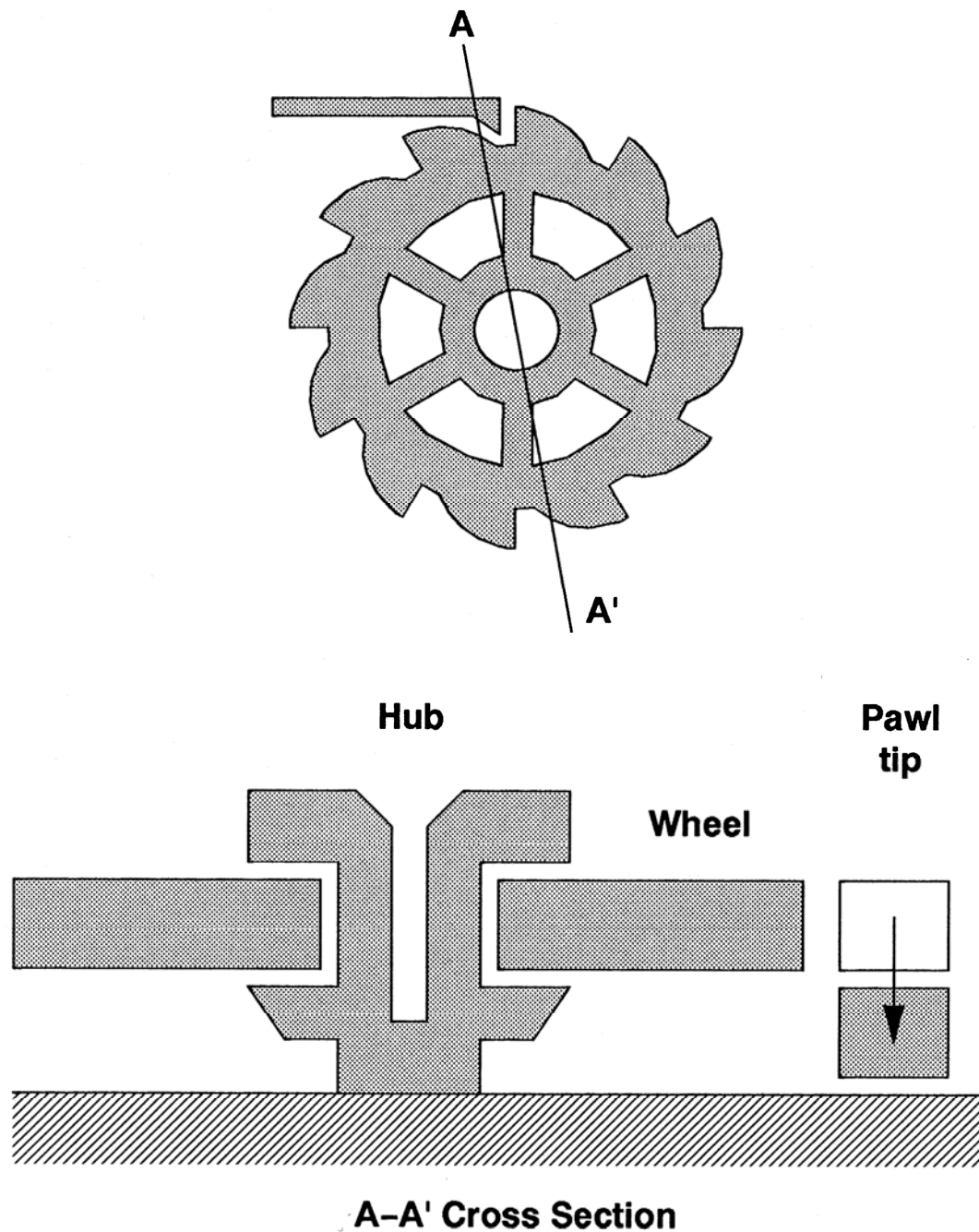


Figure 2.7 Cross section of the ratchet wheel and pawl tip after unbalanced levitation force is induced on the comb structure.

plane is essential for successful electrostatic actuation of micromechanical structures because of the need to shield the structures from relatively large vertical fields [43, 44]. It has been observed that if the underlying nitride and oxide passivation layers are not covered with a grounded polysilicon shield, the application of a dc bias voltage will cause the structures to be stuck down to the substrate. Furthermore, varying the bias voltage causes the structures to behave unpredictably.

In previous studies of the electrostatic-comb drive, a heavily doped polysilicon film underlies the resonator and the comb structure. However, this ground plane contributes to an unbalanced electrostatic field distribution, as shown in Fig. 2.8 [41]. The imbalance in the field distribution results in a net vertical force induced on the movable comb finger. The positively biased drive comb fingers induce negative charges on both the ground plane and the movable comb finger. These like charges yield a vertical force which repels or levitates the structure away from the substrate. The net vertical force, F_z , can be evaluated using the energy method:

$$E = q\Phi \quad (2.17)$$

where E is the stored electrostatic energy, q is the charge induced on the movable finger, and Φ is the potential. Differentiating with respect to the normal direction z yields

$$F_z = \frac{\partial E}{\partial z} = q \frac{\partial \Phi}{\partial z} + \Phi \frac{\partial q}{\partial z} \quad (2.18)$$

However, we have that

$$q \neq 0 \text{ and } \frac{\partial \Phi}{\partial z} \neq 0, \quad (2.19)$$

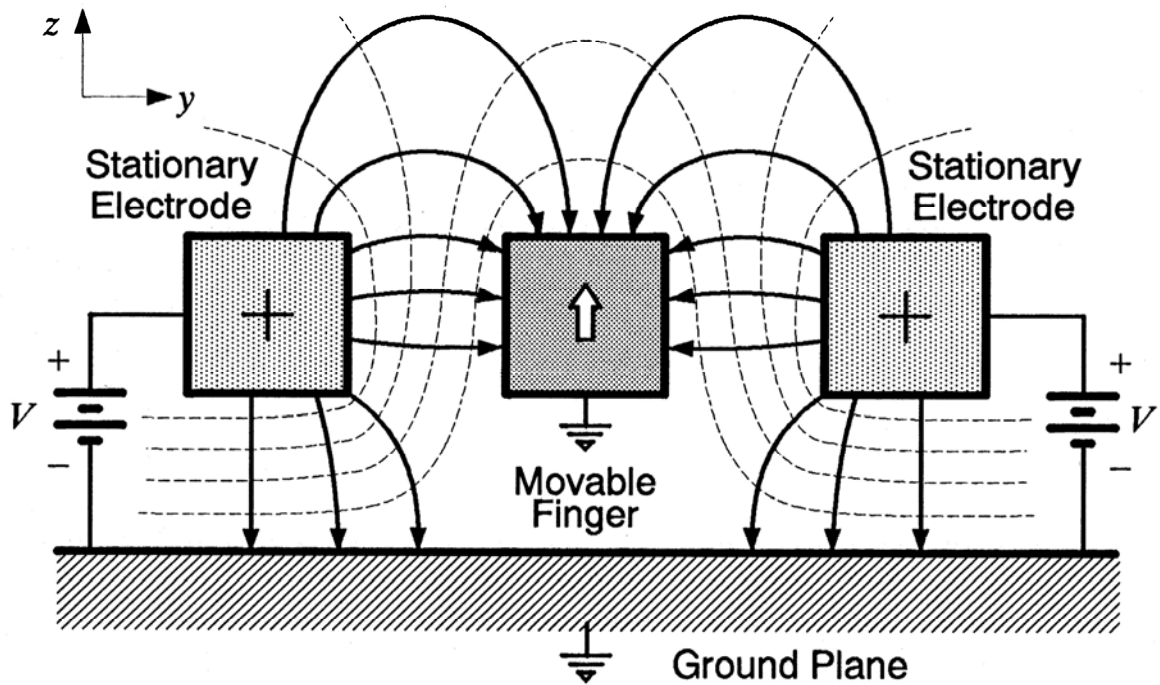


Figure 2.8 Cross section of the potential contours (dashed) and electric fields (solid) of a comb finger under levitation force induced by two adjacent electrodes.

and thus,

$$F_z \neq 0. \quad (2.20)$$

Whether this force causes significant static displacement or excites a vibrational mode of the structure depends on the compliance of the suspension and the quality factor for vertical displacements.

2.2.2 Finite-Element Simulation

Using *Maxwell* [41] to simulate the cross section of the comb fingers biased with a dc voltage, we obtain the potential contour plots at different elevations, three of which are shown in Figs. 2.9 to 2.11. The simulations provide simultaneous outputs of the vertical force induced on the movable comb fingers. The vertical force, F_z , is then plotted against levitation, z , at different dc bias voltages, resulting in Fig. 2.12.

There are several important observations from Fig. 2.12. First, the stable equilibrium levitation, z_0 , is the same for any nonzero bias voltages. Thus, in the absence of a restoring spring force, the movable comb fingers will be levitated to z_0 upon the application of a dc bias. Second, given z , F_z is proportional to the square of the applied dc bias, V_p^2 . And at any V_p , F_z is roughly proportional to $(-z)$ as long as z is less than z_0 . Thus,

$$F_z \propto V_p^2 \frac{(z_0 - z)}{z_0} \Rightarrow F_z \approx \gamma_z V_p^2 \frac{(z_0 - z)}{z_0} \quad \text{for } z < z_0 \quad (2.21)$$

where the constant of proportionality, γ_z [$\text{pN}\cdot\text{V}^{-2}$], is defined as the vertical drive capacity.

An important interpretation of Eq. (2.21) is that since $F_z \propto (-z)$, the levitation force behaves like an electrostatic spring, such that $F_z = k_e(z_0 - z)$, where k_e is the

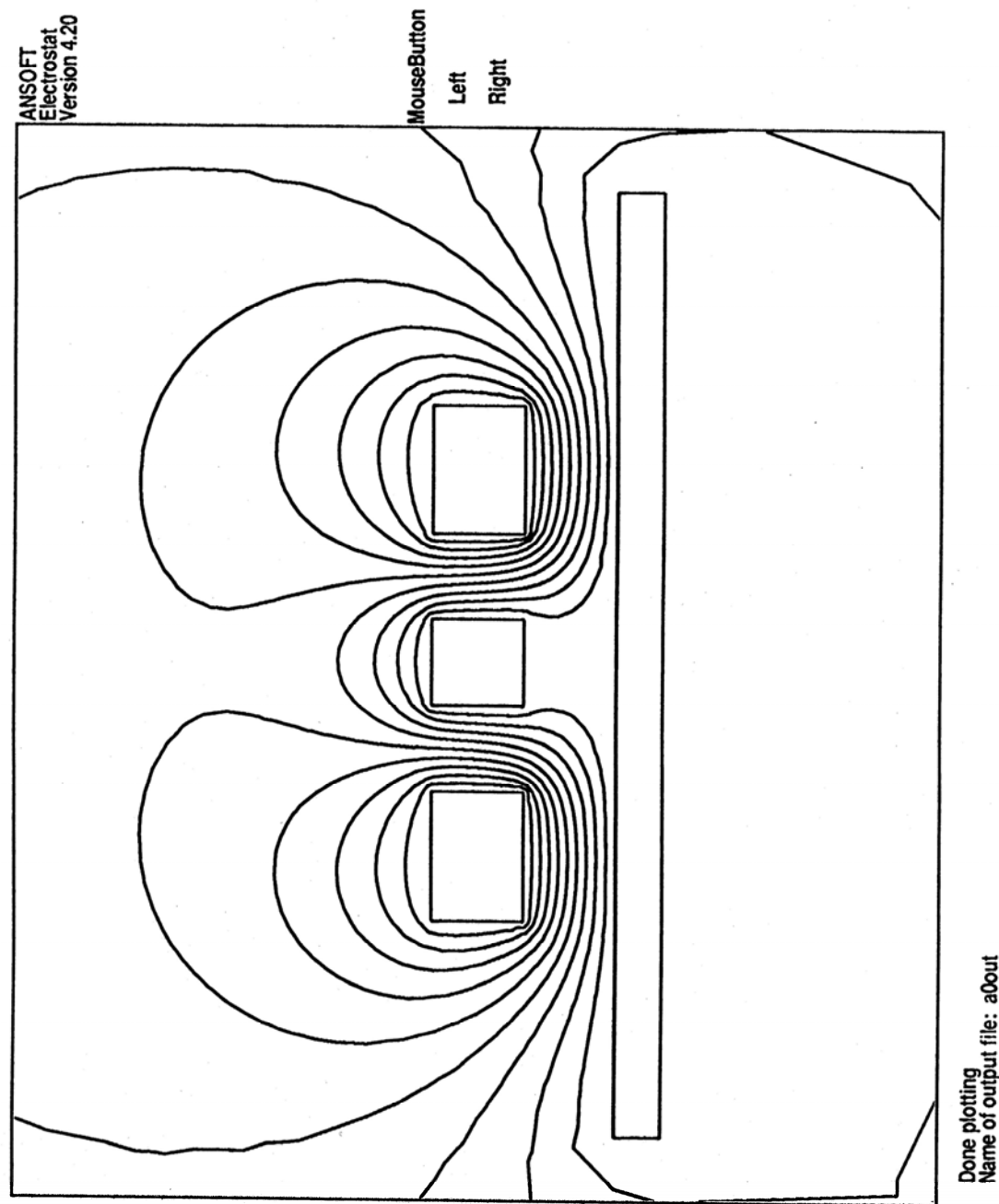


Figure 2.9 Maxwell output showing potential contours at $z = 0$.

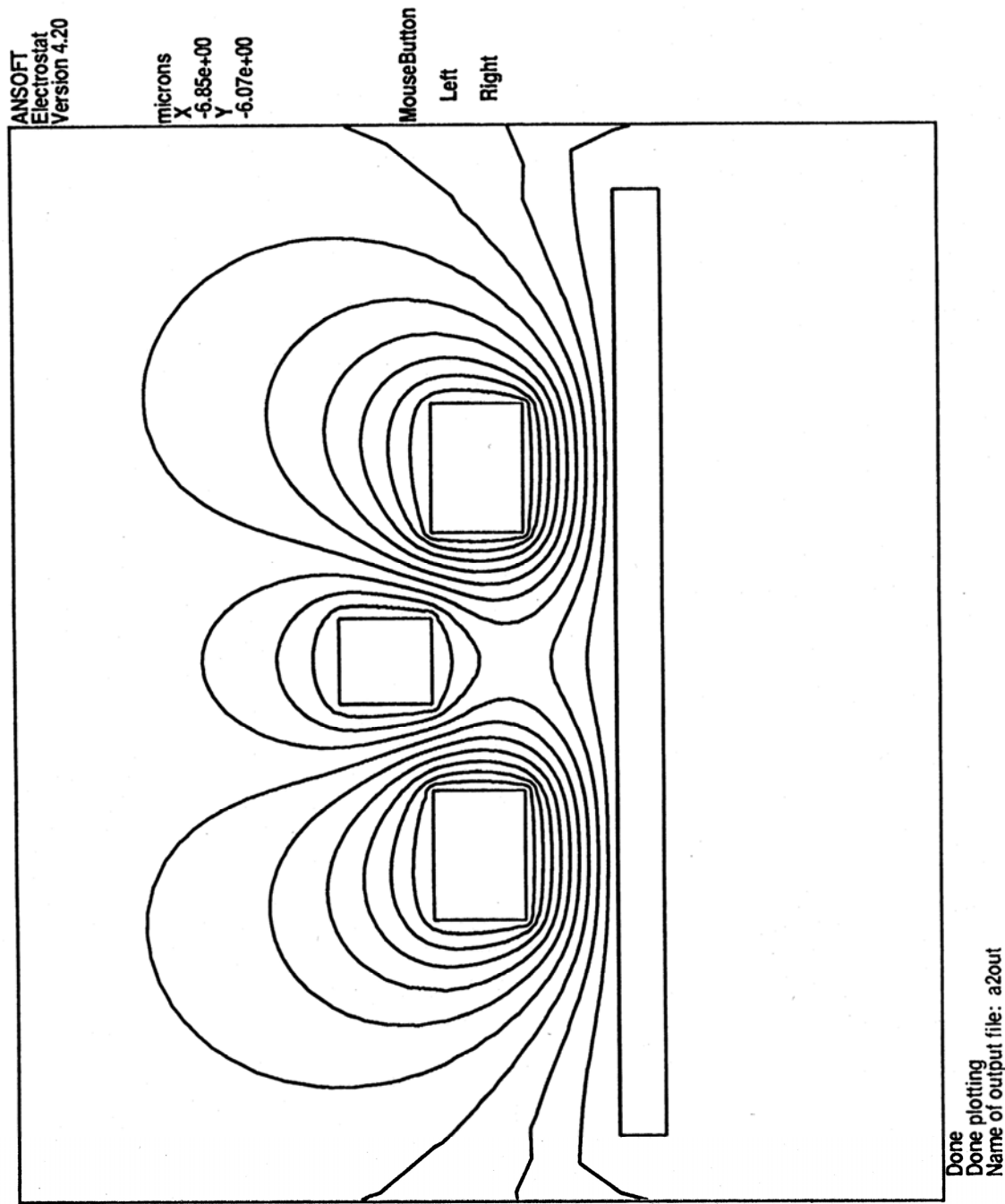


Figure 2.10 Maxwell output at $z = 1 \mu\text{m}$.

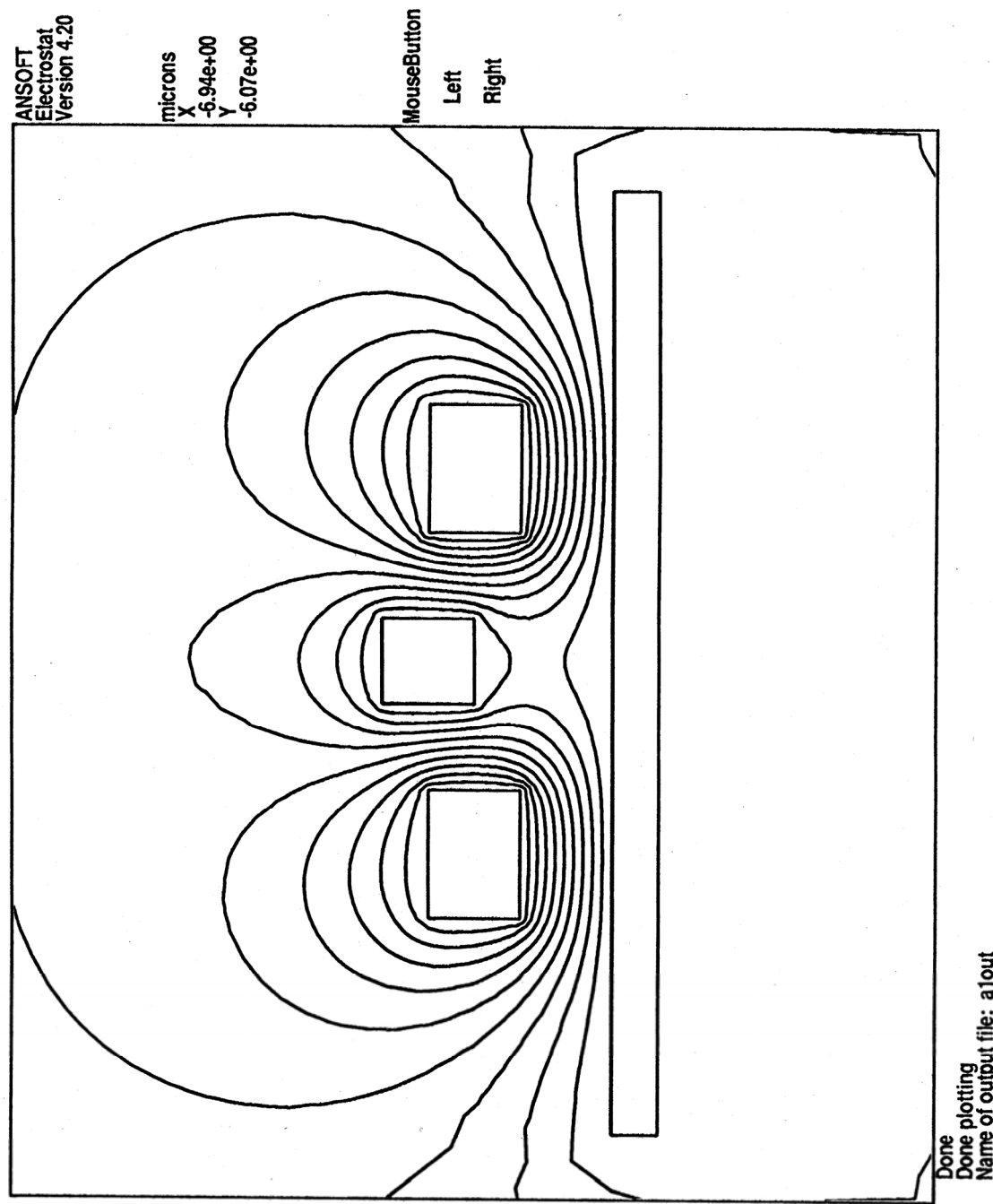


Figure 2.11 Maxwell output at $z = 2 \mu\text{m}$.

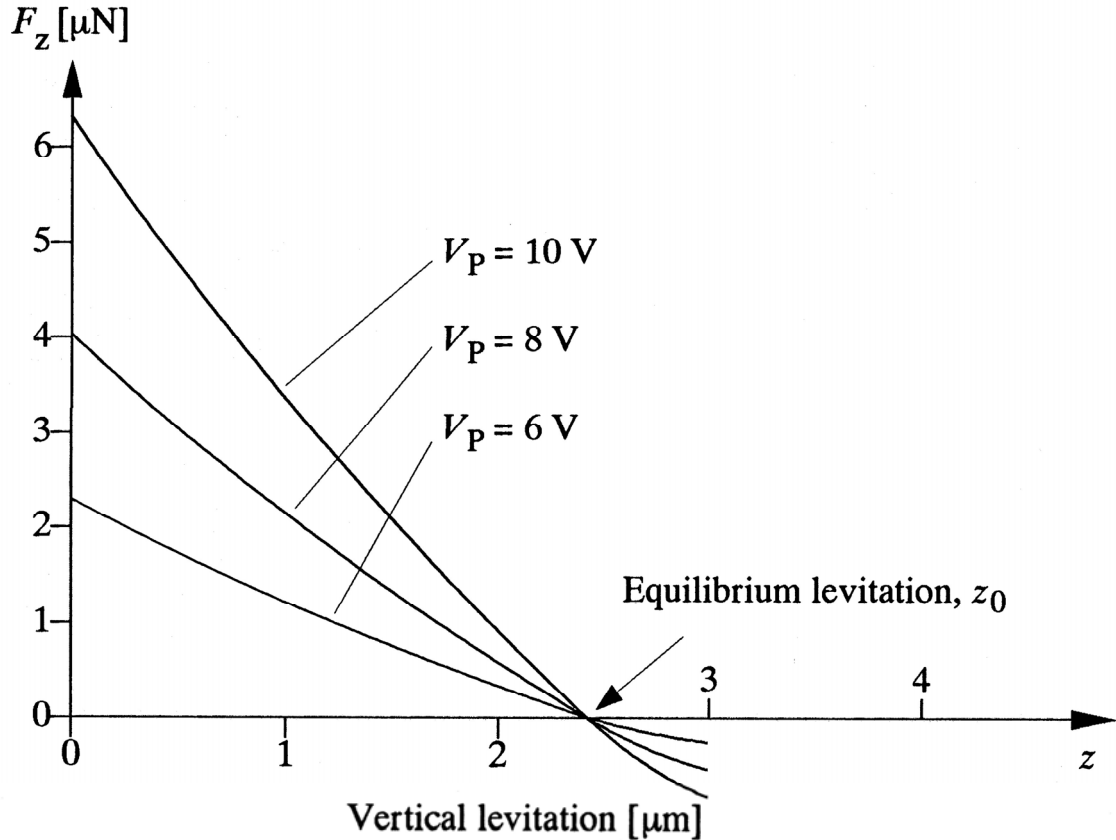


Figure 2.12 Simulated F_z vs z at different V_p . F_z is normalized to per-comb-finger (finger dimensions: $h = g = 2 \mu\text{m}$, $w = 4 \mu\text{m}$).

electrostatic spring constant,

$$k_e = \gamma_z \frac{V_p^2}{z_0} \quad (2.22)$$

Both Eqs. (2.21) and (2.22) will be used extensively in the following discussions on vertical transfer function and vertical resonance.

2.2.3 Vertical Transfer Function

The total vertical force acting on the comb fingers includes the levitation force, F_z , and the passive restoring spring force, F_k , generated by the mechanical suspensions of the system, as illustrated in Fig. 2.13. The vertical dc transfer characteristics can be evaluated by solving

$$F_{\text{net}} = F_z - F_k = 0 \quad (2.23)$$

where F_{net} is the net force acting on the movable comb finger, and

$$F_k = k_z z \quad (2.24)$$

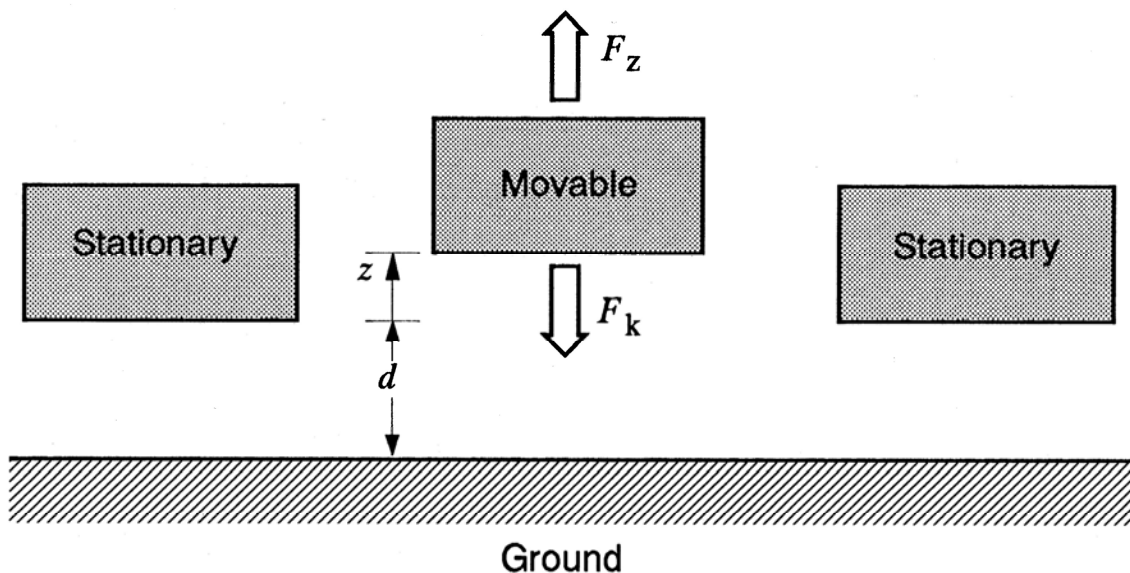


Figure 2.13 The vertical forces acting on a movable comb finger.

where k_z is the vertical spring constant. Substituting Eqs. (2.21) and (2.24) into Eq. (2.23) we have

$$\gamma_z V_p^2 \frac{(z_0 - z)}{z_0} - k_z z = 0 \quad (2.25)$$

Solving for z in terms of V_p yields

$$z = \frac{z_0 \gamma_z V_p^2}{k_z z_0 + \gamma_z V_p^2} \quad (2.26)$$

Equation (2.26) is plotted in Fig. 2.14. The initial slope of the curve is largely dependent on γ_z , which determines the threshold voltage where levitation reaches 90% of the maximum, and the asymptotic value approaches z_0 . Therefore, in certain applications where vertical levitation is undesirable, both γ_z and z_0 should be minimized. The method to control vertical levitation is discussed in section 2.2.5 of this chapter.

2.2.4 Vertical Resonant Frequency

In this section, we consider the case where the resonators are not damped vertically, such as for the case of vibrations in vacuum. This assumption is justified on the ground that the levitation force is much weaker than the force generated by a conventional vertically-driven microbridge with an efficient parallel-plate-capacitor drive [16]. Therefore, because of squeeze-film damping, vertical vibration in air is not significant for the weak levitation force.

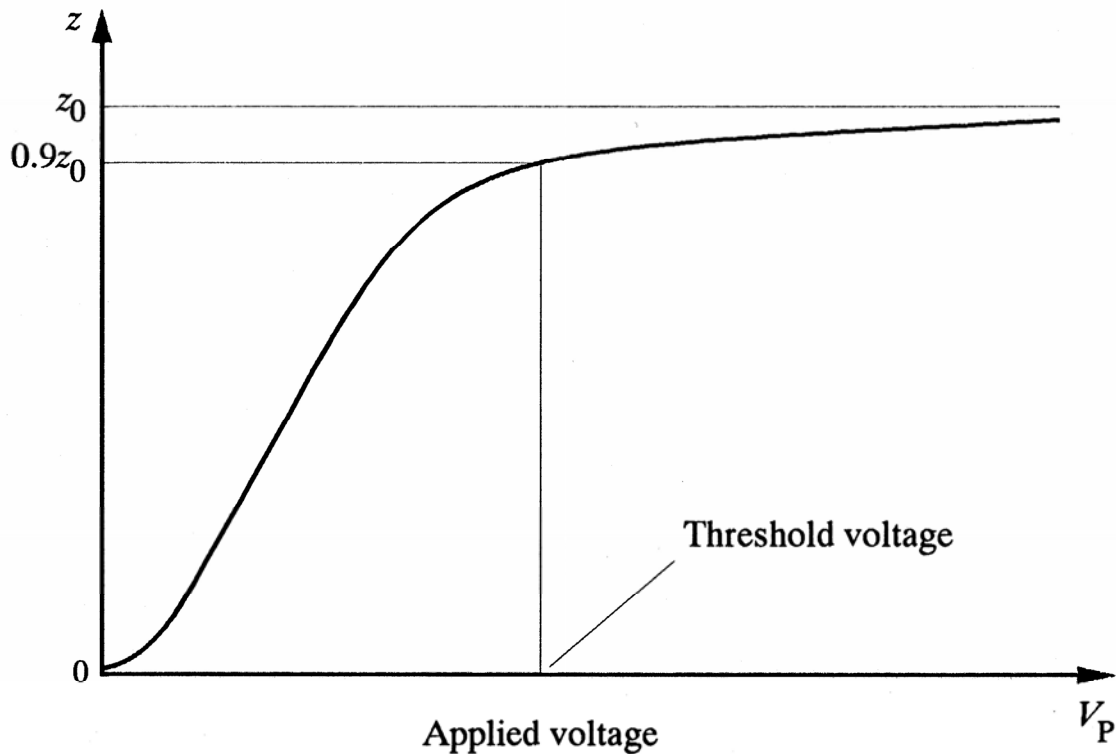


Figure 2.14 Theoretical levitation (z) vs V_p on dimensionless axes. The scales on each axis are to be fitted to experimental results.

Thus, in the absence of damping, the governing equation of motion is a second-order-differential equation, given by

$$F_{\text{net}} = M \frac{\partial^2 z}{\partial t^2} \quad (2.27)$$

where M is the effective mass of the vibrating structure.

The net vertical force, F_{net} , which is zero in dc analysis [Eq. (2.23)], is now a sinusoidal function when the bias voltage, V_p , is replaced with a generalized drive

voltage, $v_D(t)$:

$$F_{\text{net}} = F_z - F_k = \gamma_z \frac{(z_0 - z)}{z_0} v_D^2 - k_z z \quad (2.28)$$

Thus, Eq. (2.27) becomes

$$\gamma_z \frac{(z_0 - z)}{z_0} v_D^2 - k_z z = M \frac{\partial^2 z}{\partial t^2} \quad (2.29)$$

For a drive voltage $v_D(t)$ given by

$$v_D(t) = V_p + v_d \sin(\omega t) \quad (2.30)$$

where V_p is the dc bias and v_d is the ac drive amplitude, we can assume the sinusoidal steady-state solution in z to be

$$z(t) = z_p + z_d \sin(\omega t - \phi) \quad (2.31)$$

where z_p is the average dc levitation, z_d is the vibration amplitude, and ϕ is the phase difference between the electrical drive signal and the mechanical response.

Substituting Eqs. (2.30) and (2.31) into Eq. (2.29) yields

$$\begin{aligned} -M\omega^2 z_d \sin(\omega t - \phi) &= \gamma_z \frac{z_0 - [z_p + z_d \sin(\omega t - \phi)]}{z_0} [V_p + v_d \sin(\omega t)]^2 \\ &\quad - k_z [z_p + z_d \sin(\omega t - \phi)] \end{aligned} \quad (2.32)$$

Since F_{net} is zero when only dc bias is applied, we have

$$F_{\text{net}}|_{\text{d.c.}} = \gamma_z \frac{(z_0 - z_p)}{z_0} V_p^2 - k_z z_p = 0 \quad (2.33)$$

Using Eq. (2.33) to eliminate dc terms in Eq. (2.32) leads to

$$\begin{aligned} -M\omega^2 z_d \sin(\omega t - \phi) &= \frac{\gamma_z}{z_0} [z_0 - z_p - z_d \sin(\omega t - \phi)] [2V_p v_d \sin(\omega t) + v_d^2 \sin^2(\omega t)] \\ &\quad - \frac{\gamma_z}{z_0} z_d \sin(\omega t - \phi) V_p^2 - k_z z_d \sin(\omega t - \phi) \end{aligned} \quad (2.34)$$

At this point, in order to find the linear resonant behavior, we eliminate the second-order terms:

$$-M\omega^2 z_d \sin(\omega t - \phi) = 2\gamma_z \frac{z_0 - z_p}{z_0} V_p v_d \sin(\omega t) - \left(\frac{\gamma_z}{z_0} V_p^2 + k_z \right) z_d \sin(\omega t - \phi) \quad (2.35)$$

Expressing z_d in terms of v_d :

$$z_d \sin(\omega t - \phi) = \frac{2\gamma_z \frac{z_0 - z_p}{z_0} V_p v_d}{\frac{\gamma_z}{z_0} V_p^2 + k_z - M\omega^2} \sin(\omega t) \quad (2.36)$$

which describes a classical undamped system under harmonic force. The undamped vertical resonant frequency, ω_1 , under the influence of applied voltage can then be solved as

$$\omega_1 = \left(\frac{k_z + \gamma_z V_p^2 / z_0}{M} \right)^{\frac{1}{2}} \quad (2.37)$$

and ϕ is identically zero for $\omega \neq \omega_1$.

An important observation is that the vertical resonant frequency is a strong function of the applied dc bias, V_p . If we define the mechanical resonant frequency (under zero bias) as ω_0 , such that

$$\omega_0 = \left(\frac{k_z}{M} \right)^{\frac{1}{2}} \quad (2.38)$$

We can quantify the frequency shift as a ratio given by

$$\frac{\omega_1}{\omega_0} = \left(\frac{k_z + \gamma_z V_p^2 / z_0}{k_z} \right)^{\frac{1}{2}} \quad (2.1)$$

which is plotted in Fig. 2.15. The frequency ratio ω_1 / ω_0 asymptotically approaches a straight line, such that

$$\lim_{V_p \rightarrow \infty} \left(\frac{\omega_1}{\omega_0} \right) = \left(\frac{\gamma_z}{z_0 k_z} \right)^{\frac{1}{2}} \quad (2.2)$$

Equation (2.39) is consistent with the observation made in section 2.2.2, that the levitation force behaves like an electrostatic spring, with a spring constant $k_e = \gamma_z V_p^2 / z_0$

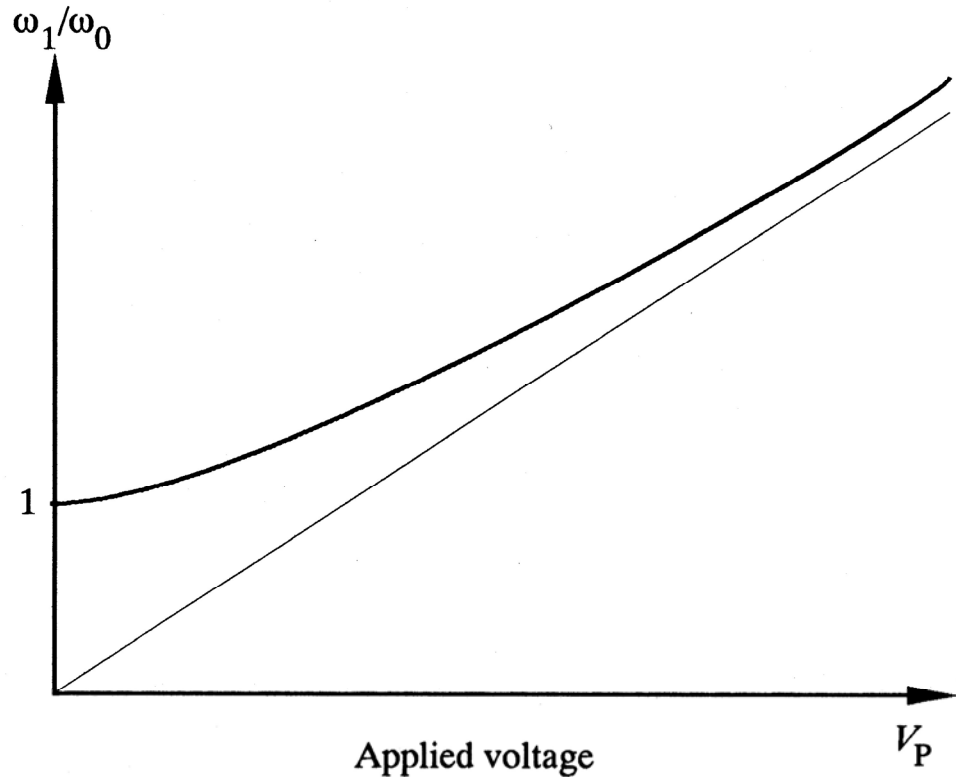


Figure 2.15 Theoretical frequency ratio ω_1/ω_0 vs. V_p on dimensionless axes. The scales on each axis are to be fitted to experimental results.

[Eq. (2.22)]. If we substitute Eq. (2.22) into Eq. (2.39), we then have

$$\frac{\omega_1}{\omega_0} = \left(\frac{k_z + k_e}{k_z} \right)^{\frac{1}{2}} \quad (2.3)$$

which shows that the electrostatic spring constant adds to the mechanical spring constant for determining the resonant frequency.

The comb can therefore be useful for controlling the vertical resonance. In the case where the vertical mechanical spring constant of the suspension is very close to the

lateral one, i.e., $k_z \approx k_x$, the undesirable simultaneous excitation of both vertical and lateral modes of motion can be conveniently avoided by shifting away the vertical resonant frequency with a dc bias voltage.

2.2.5 Levitation Control Method

In addition to shifting the vertical resonant frequency, it is desirable to control the dc levitation effect as well. There are several means to reduce the levitation force. By eliminating the ground plane and removing the substrate beneath the comb structures with bulk-micromachining techniques, the field distribution becomes balanced. Alternatively, a top ground plane suspended above the comb drive will achieve a balanced vertical force on the comb. However, both of these approaches require significantly more complicated fabrication sequences.

A simpler solution is to modify the comb drive itself. Reversing the polarity on alternating drive fingers results in an altered field distribution, as shown in Fig. 2.16. Following the analysis in Eqs. (2.17) to (2.20), we now have $\Phi = 0$ and $\partial\Phi / \partial z \approx 0$, and thus

$$F_z = \frac{\partial E}{\partial z} = q \frac{\partial \Phi}{\partial z} + \Phi \frac{\partial q}{\partial z} \approx 0 \quad (2.4)$$

To further suppress levitation, the ground plane is modified such that underneath each comb finger there is a strip of conductor biased at the same potential, as illustrated in Fig. 2.17. The polysilicon layer is used to form the crossovers to electrically isolate

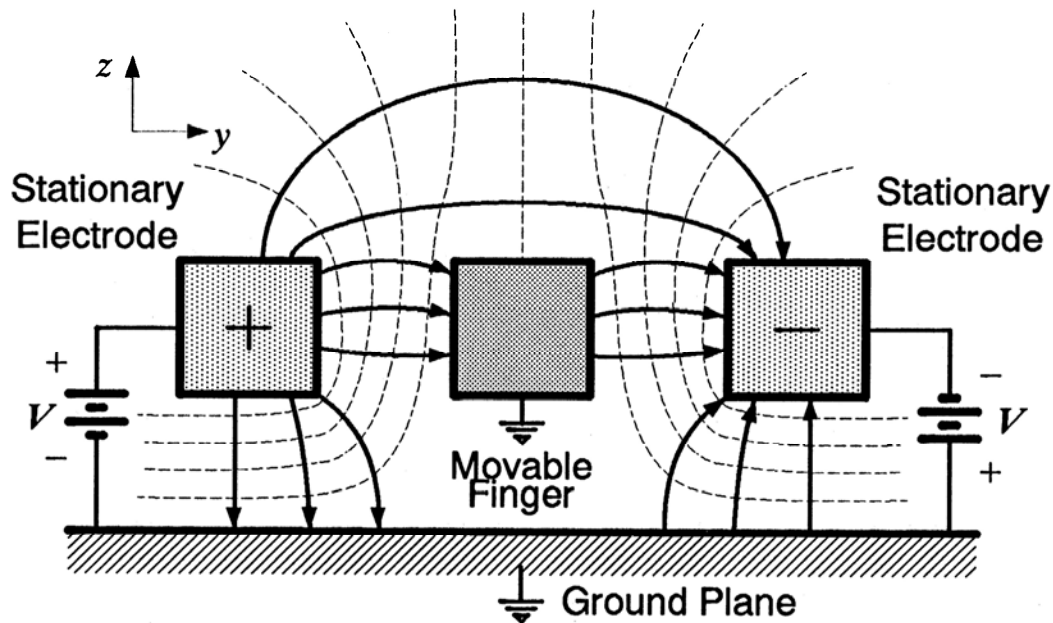


Figure 2.16 Cross section of the potential contours (dashed) and electric fields (solid) around a movable comb finger when differential bias is applied to the two adjacent electrodes.

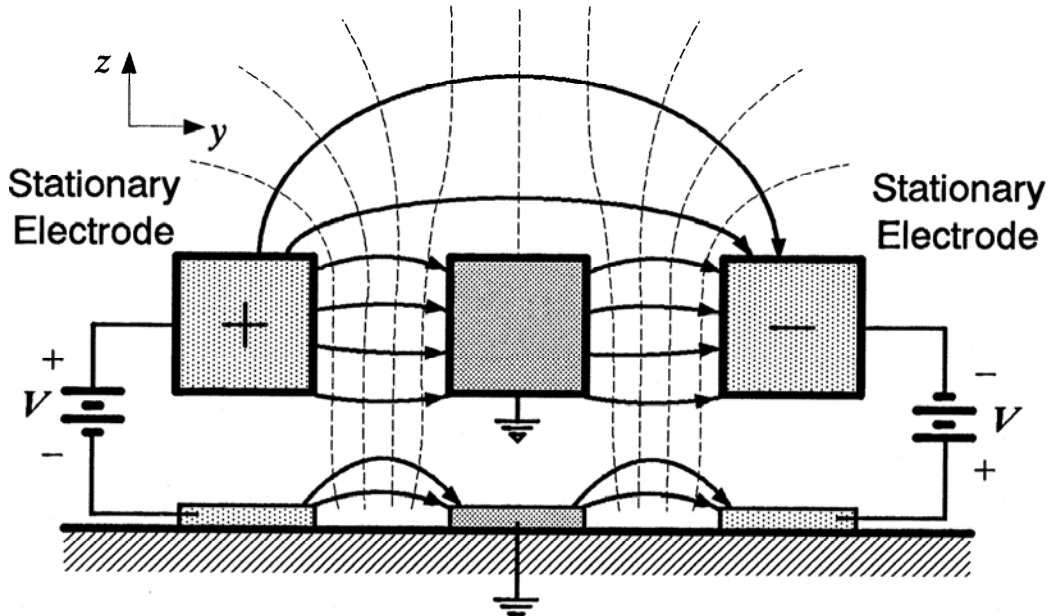


Figure 2.17 Potential contours (dashed) and electric fields (solid) around a movable comb finger when differential bias is applied to the two adjacent electrodes and the striped ground conductors.

alternating comb fingers (Fig. 2.18). Simulation shows that the levitation force is suppressed by over an order of magnitude compared to the original biasing scheme.

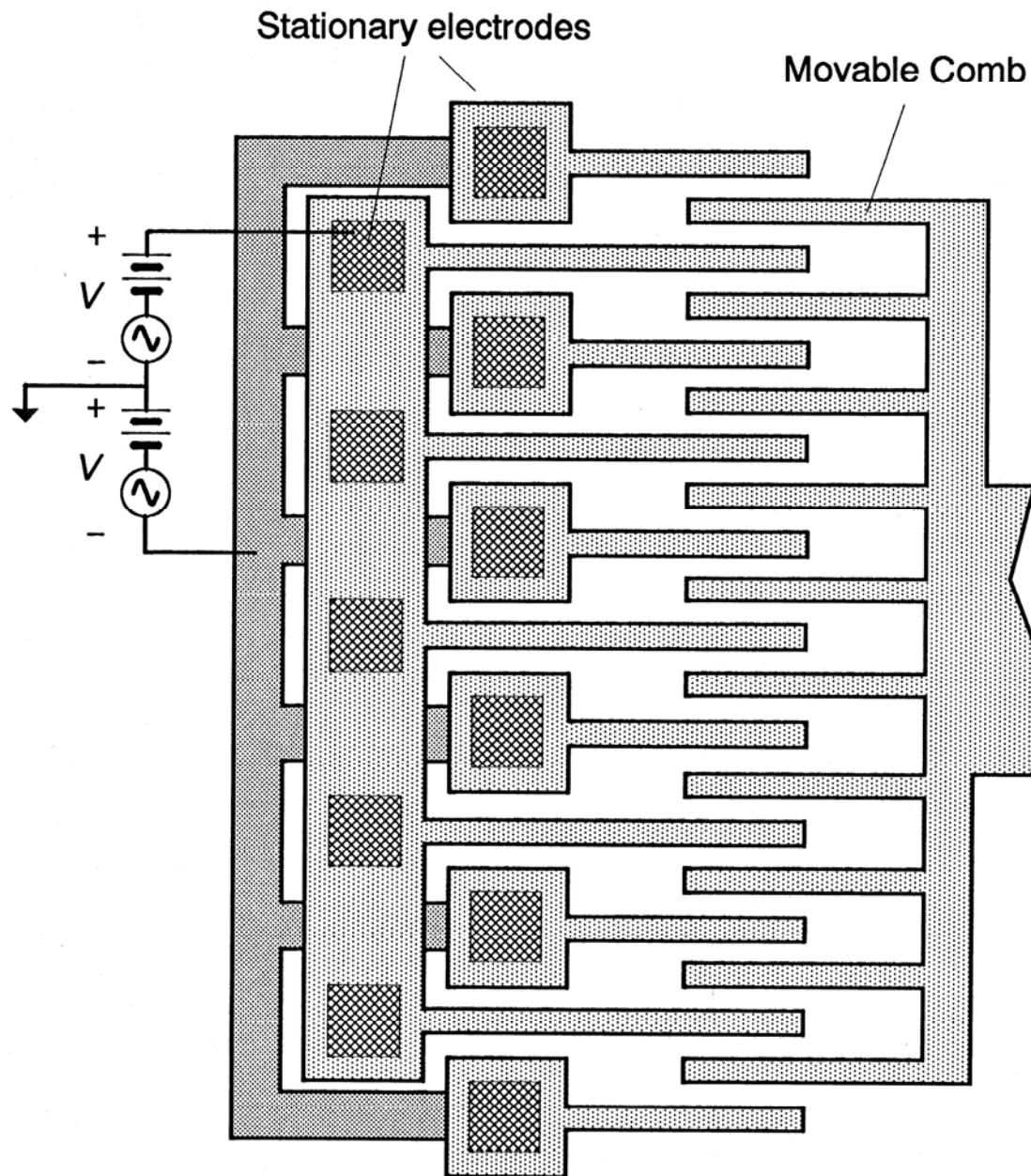


Figure 2.18 Crossover layout for electrical isolation of alternating drive electrodes.

2.3 MECHANICAL ANALYSIS

In the previous sections, we have completed the analysis for both the lateral and vertical electrostatic characterizations of the comb drive, using the terms k_x and k_z to represent the mechanical spring constants. In this section, we will analyze various mechanical spring designs for both classes of linear and torsional resonators, deriving equations for the spring constants as well as for the lateral resonant frequencies. Finally, we will discuss the quality factor Q .

2.3.1 Linear Lateral Resonant Structures

The design criteria for the suspensions of a large-amplitude, lateral resonator actuated with comb drives are two-fold. First, the suspensions should provide freedom of travel along the direction of the comb-finger motions (x), while restraining the structure from moving sideways (y) to prevent the comb fingers from shorting to the drive electrodes. Therefore, the spring constant along the y direction must be much higher than that along the x direction, i.e., $k_y \gg k_x$. Second, the suspensions should allow for the relief of the built-in stress of the structural polysilicon film as well as axial stress induced by large vibrational amplitudes.

Folded-beam suspension design fulfills these two criteria. Figure 1.3 (repeated here as Fig. 2.19 for convenience) is the layout of a linear resonant structure supported by a pair folded-beam suspensions. As we will show, this design allows large deflection in the x direction (perpendicular to the length of the beams) while providing stiffness in

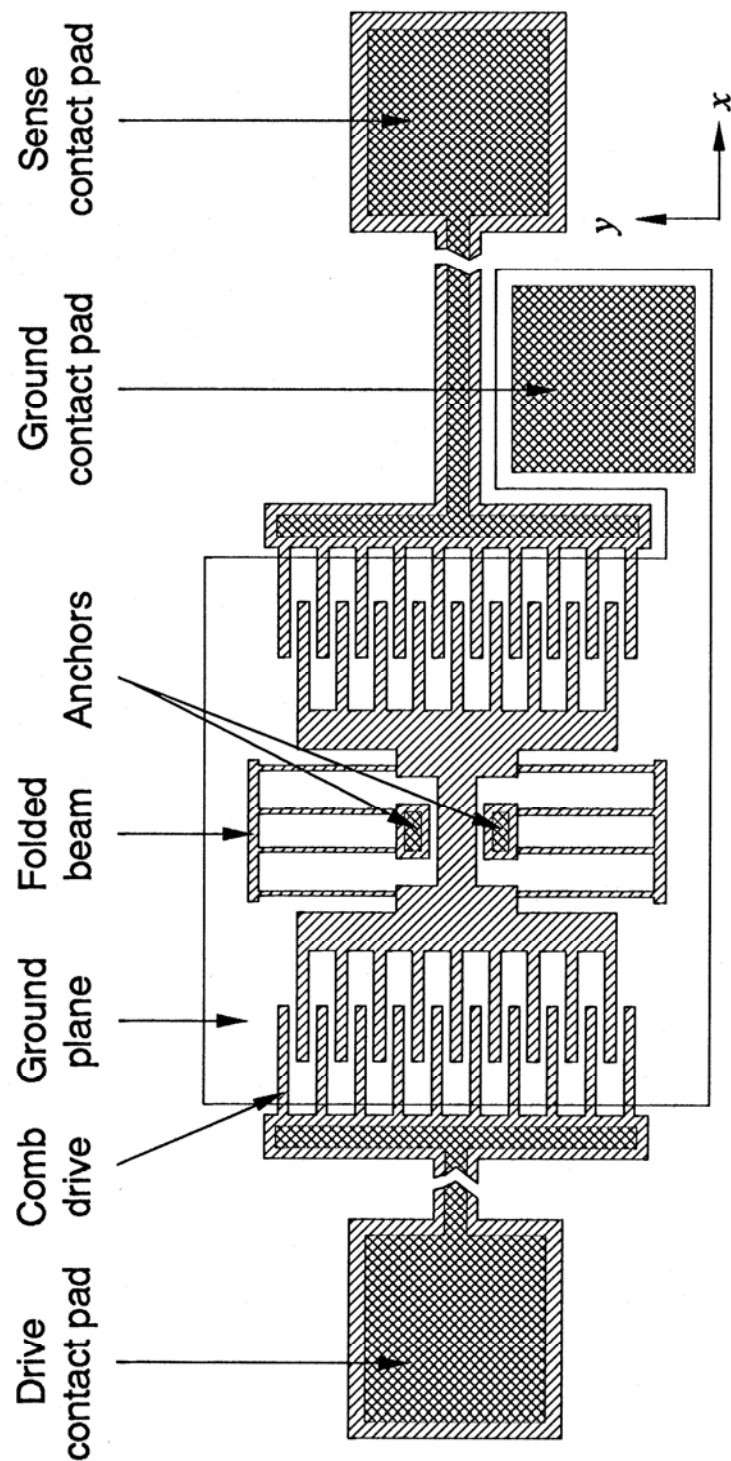


Figure 2.19 Layout of a linear resonant structure supported by a pair of folded-beam suspensions.

the y direction (along the length of the beams). Furthermore, the only anchor points for the whole structure are near the center, thus allowing the parallel beams to expand or contract in the y direction, relieving most of the built-in and induced stress. This section describes the analysis of the spring constant of the folded-beam support, the lateral resonant frequency and the quality factor of lateral resonators similar to Fig. 2.19.

2.3.1.1 Spring Constant of Folded-Beam Support

Figure 2.20 shows the mode shape of the folded-beam support when the resonant plate is statically displaced by a distance X_0 under an applied force F_x in the positive x

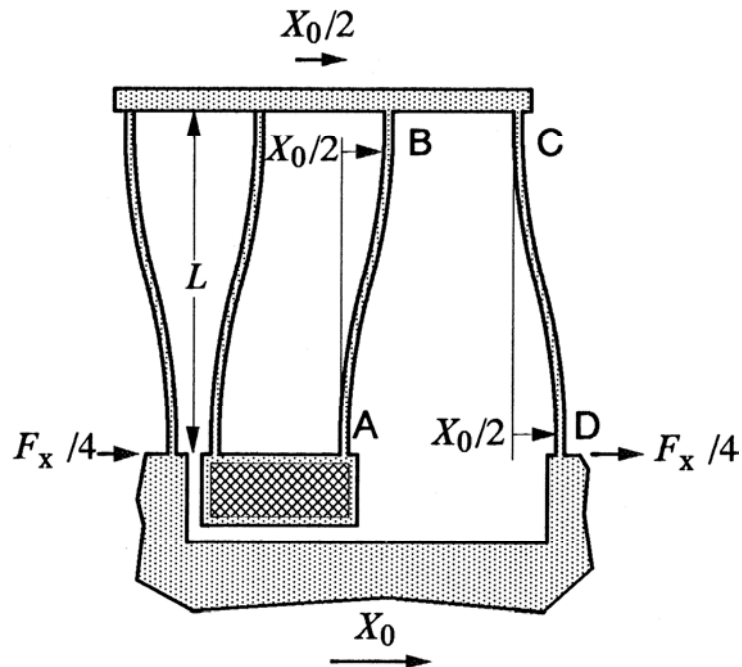


Figure 2.20 Mode shape of a folded-beam support when the resonant plate is displaced by X_0 under a force F_x .

direction. Each of the beams has a length L , width w , and thickness h . We can simplify the analysis by considering segment [AB], which is illustrated in Fig. 2.21. The following analysis assumes that the outer connecting truss for the 4 beam segments is rigid, which is justified because of its wider design. Therefore, as part of the boundary conditions, the slopes at both ends of the beams are identically zero. Also, since geometric shortening in the y direction is identical for all 4 beams, there is no induced axial stress as a result of large deflections.

Since the resonant plate is supported by 4 identical beams, the force acting on

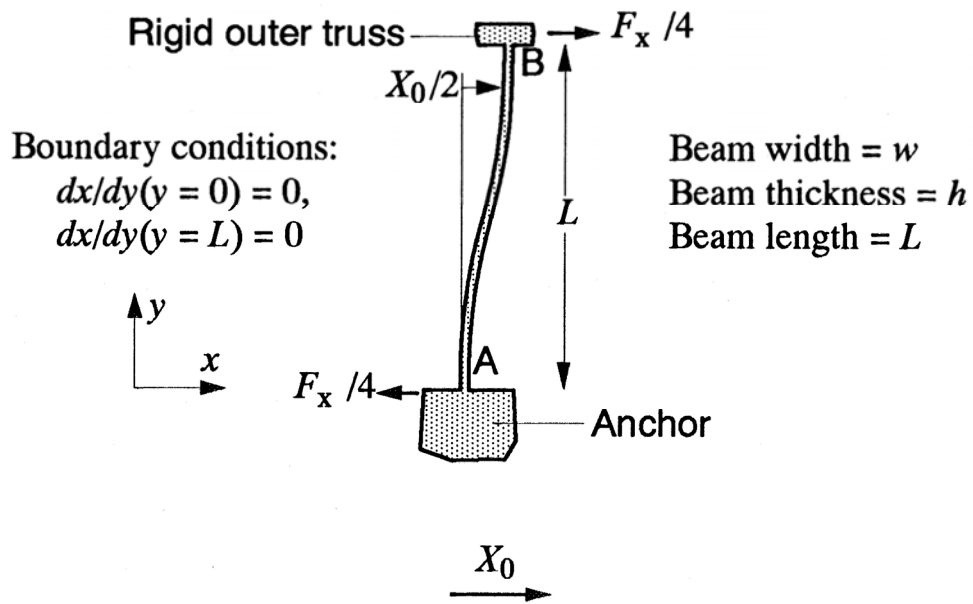


Figure 2.21 Mode shape of segment [AB].

each beam is $F_x / 4$. The equation of deflection for [AB] is given by [45]

$$x(y) = \frac{F_x}{4(12EI_z)} (3Ly^2 - 2y^3) \quad \text{for } 0 \leq y \leq L \quad (2.43)$$

where E is the Young's modulus for polysilicon and I_z is the moment of inertia of the beam cross section with respect to the z axis. Note that since this beam segment has a slope of zero at either ends, it cannot be considered as a cantilever beam. Examining Fig. 2.20, we know that segment [AB] is deflected by $X_0 / 2$ at point B. So with the boundary condition of $x(L) = X_0 / 2$, we have

$$\begin{aligned} \frac{X_0}{2} &= \frac{F_x}{48EI_z} (3L^3 - 2L^3) \\ \Rightarrow X_0 &= \frac{F_x L^3}{24EI_z} \end{aligned} \quad (2.44)$$

Thus, the system spring constant in the x direction is

$$k_x = \frac{F_x}{X_0} = \frac{24EI_z}{L^3} \quad (2.45)$$

Similarly, the equation for vertical deflection under an induced vertical force, F_z , is given by

$$z(y) = \frac{F_z}{48EI_x} (3Ly^2 - 2y^3) \quad \text{for } 0 \leq y \leq L \quad (2.46)$$

where I_x is the moment of inertia with respect to the x axis. The vertical spring constant,

k_z , is

$$k_z = \frac{24EI_x}{L^3} \quad (2.47)$$

Finally, to complete the evaluation, we need to express the moments of inertia I in terms of physical dimensions. For an ideal beam with rectangular cross section, having a width w and a thickness h , the moments of inertia are [45]:

$$I_z = \frac{hw^3}{12} \quad \text{and} \quad I_x = \frac{h^3w}{12} \quad (2.48)$$

However, due to fabrication difficulties, the cross section of the beams may be slightly trapezoidal (Fig. 2.22). With the dimensions indicated in Fig. 2.22, we can derive I_z and I_x by evaluating the following integrals over the area of the cross section:

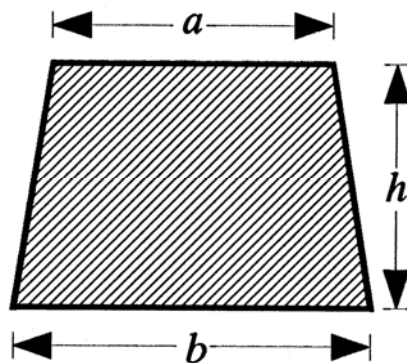


Figure 2.22 Cross section of a beam as a result of nonideal plasma-etching process for polysilicon.

$$\begin{aligned} I_z &= \int x^2 dA = \frac{h}{48} (a+b)(a^2 + b^2) \\ I_x &= \int z^2 dA = \frac{h^3 (a^2 + 4ab + b^2)}{36(a+b)} \end{aligned} \quad (2.49)$$

It should be noted that since the cross sections of the beams are not far from being rectangular, the shift in the neutral axis is negligible. Otherwise, second order effects must be considered in stress calculations [46].

Due to the parallel-beam design, the suspension is very stiff in the y direction. One possible mechanism that causes the resonant plate and the comb fingers to move sideways is when four of the parallel beams are stretched while the other four are compressed. The spring constant along the length of a beam, k_y , is given by [45]

$$k_y = \frac{AE}{L} \quad (2.50)$$

where A is the cross-sectional area of the beam. As in the previous sections, we can assume that the outer connecting trusses are rigid. Therefore, the ratio of the system spring constant in the y direction ($8k_y$) to that in the x direction [k_x , Eq. (2.45)] is

$$\frac{8k_y}{k_x} = \frac{8AE/L}{24EI_z/L^3} = \frac{4whL^2}{w^3h} = \frac{4L^2}{w^2} \quad (2.51)$$

For a typical folded-beam design with $L = 200 \mu\text{m}$ and $w = 2 \mu\text{m}$, this ratio is evaluated to be 40,000. Thus, motion in the y direction due to beam extension and compression is very unlikely.

Another possible mechanism that causes the structure to move sideways is when at least 4 of the 8 parallel beams buckle under a force applied in the y direction, F_y . As a worst case consideration, we can use Euler's simple buckling criterion to evaluate the critical force, F_y , required to buckle a pinned-pinned beam with length L [45]:

$$F_y = \frac{\pi^2 EI_z}{L^2} \quad (2.52)$$

Comparing Eqs. (2.45) and (2.52), for a typical resonant structure with 200 μm -long folded beams, the force F_y required to buckle 4 of the supporting beams is over 60 times higher than the force F_x required to pull the structure statically by 5 μm in the x direction. During vibration, F_x required to sustain resonance is reduced by the quality factor Q , which is typically between 20 to 100 in air, and 50,000 in vacuum. Furthermore, the most probable origin of F_y is comb-finger misalignment, which is very minimal because all the critical features are defined with one mask during fabrication. Therefore, the folded-beam design is attractive for structures actuated with dense comb drives.

An alternative suspension design for linear resonant structures is the “crab-leg” flexure illustrated in Fig. 2.23 [47]. The advantage of this suspension is that the k_y / k_x ratio can be designed to a given value by adjusting the dimensions of the crab-leg segments. However, built-in stress is not relieved with this design because the suspensions are anchored on the outer perimeter of the structure. Also, extensional axial stress may become dominant during large-amplitude vibration.

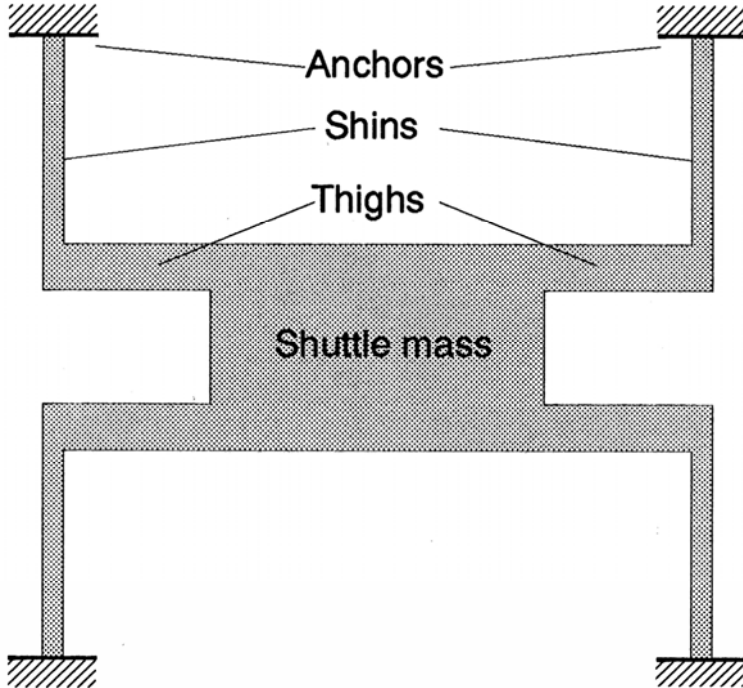


Figure 2.23 Crab-leg flexure design [47].

2.3.1.2 Spring Constant of Double-Folded Beams

A natural extension of the folded-beam suspension concept is the double-folded beam design illustrated in Fig. 2.24. This design provides the advantage of compactness in addition to all the benefits realized with the single-folded design. The spring constant for the double-folded beam can be evaluated by recognizing that each of the 8 pairs of parallel beams deflect by $X_0/4$ (compared to $X_0/2$ for the single-folded design), and each of them experiences a force of $F_x/4$ (Fig. 2.25). Thus, one of the boundary conditions

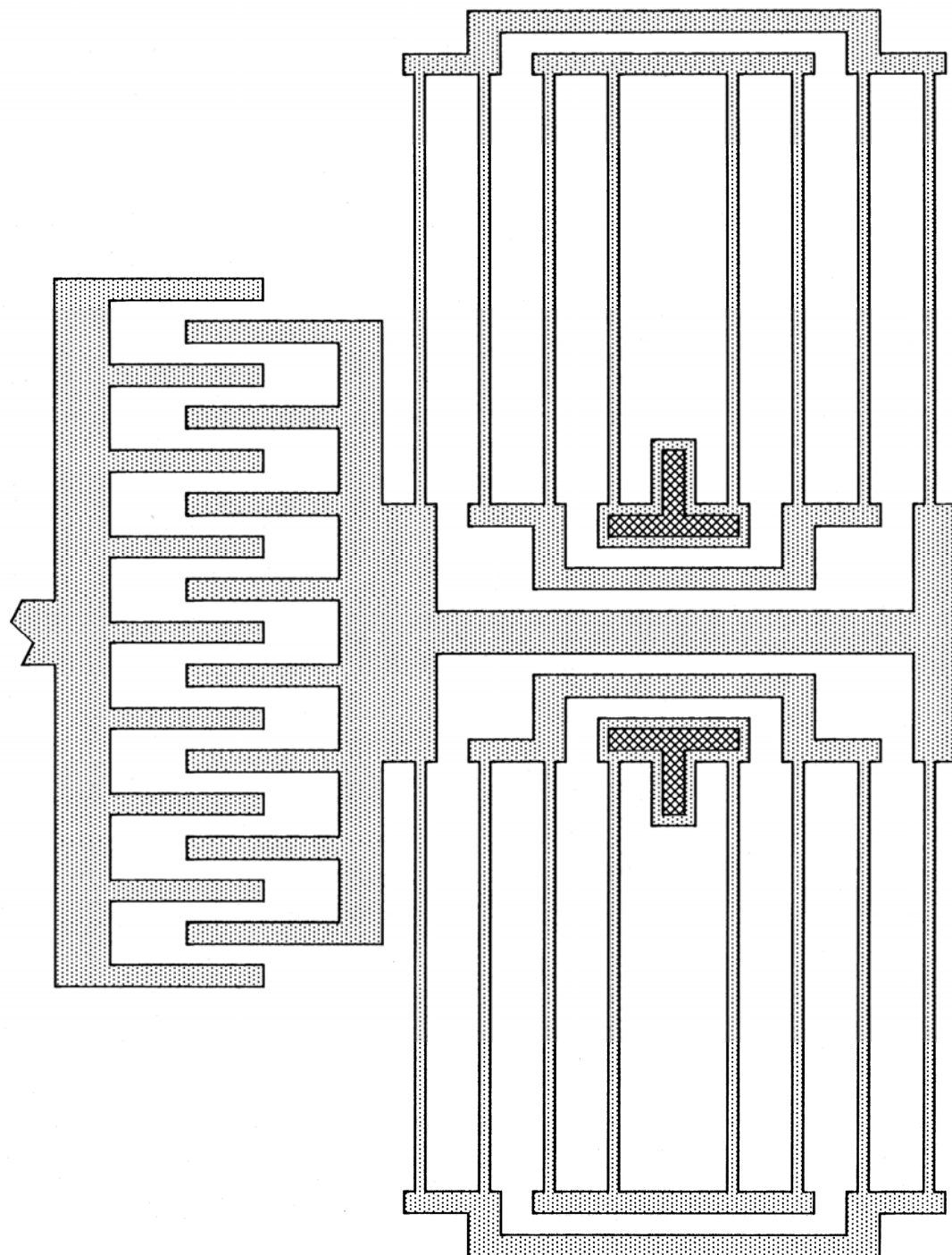


Figure 2.24 Resonant structure suspended by a pair of double-folded beams.

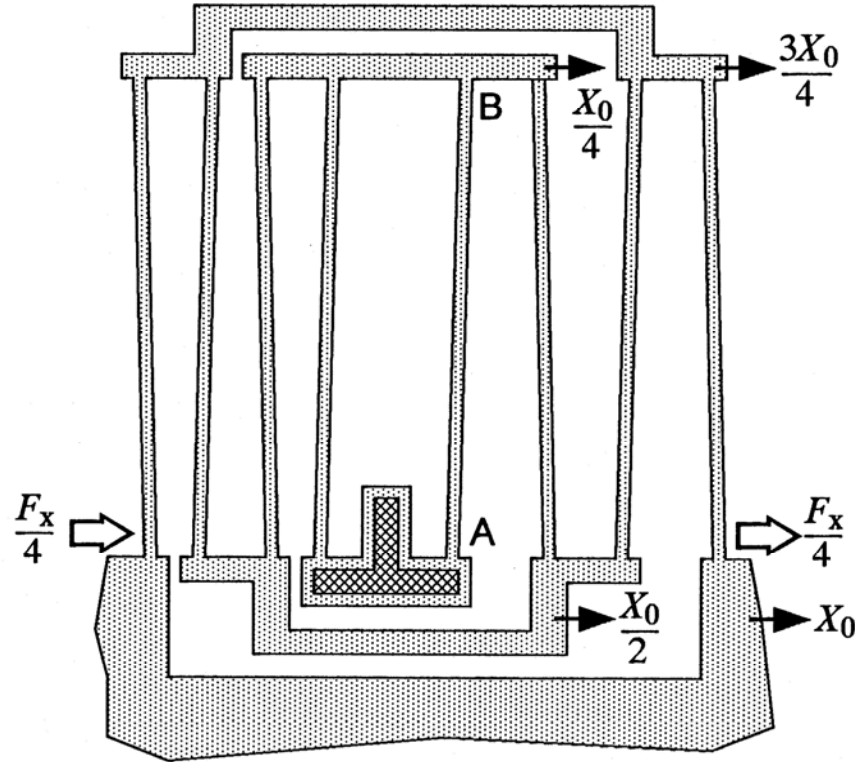


Figure 2.25 Mode shape of a double-folded suspension when the resonant plate is displaced by X_0 under a force of F_x .

for segment [AB] becomes $x(L) = X_0/4$, resulting in

$$\begin{aligned} \frac{X_0}{4} &= \frac{F_x}{48EI_x} (3L^3 - 2L^3) \\ \Rightarrow k_x|_2 &= \frac{F_x}{X_0} = \frac{12EI_z}{L^3} = \frac{k_x}{2} \end{aligned} \quad (2.53)$$

where the subscript 2 denotes a double-folded system. This derivation can be further extended to n -tuple-folded beam designs, each with $4n$ pairs of parallel beams. Upon the application of a force F_x to the system, each beam deflects by $X_0/2n$, leading to a

boundary condition for each beam segment as $x(L) = X_0/2n$. Therefore,

$$\begin{aligned} \frac{X_0}{2n} &= \frac{F_x L^3}{48EI_x} \\ \Rightarrow k_x|_n &= \frac{F_x}{X_0} = \frac{24EI_z}{nL^3} = \frac{k_x}{n} \end{aligned} \quad (2.54)$$

2.3.1.3 Lateral Resonant Frequency

To evaluate the lateral resonant frequency of the original folded-beam system, we use Rayleigh's energy method [16]:

$$K.E_{\max} = P.E_{\max} \quad (2.55)$$

where $K.E_{\max}$ is the maximum kinetic energy during a vibration cycle, and $P.E_{\max}$ is the maximum potential energy. We will first evaluate $K.E_{\max}$.

It is assumed that during the motion, the beams all displace with mode shapes equal to their deflections under static loads. $K.E.$ reaches its maximum when the structure is at maximum velocity, and is given by

$$\begin{aligned} K.E_{\max} &= K.E_p + K.E_t + K.E_b \\ &= \frac{1}{2} v_p^2 M_p + \frac{1}{2} v_t^2 M_t + \frac{1}{2} \int v_b^2 dM_b \end{aligned} \quad (2.56)$$

where M 's and v 's are the masses and maximum velocities, and subscripts p, t and b refer to the plate, the sum of the two horizontal trusses and the sum of the eight parallel beam segments, respectively. Since the horizontal trusses displace at half the velocity of the

plate, we have

$$v_p = \omega X_0 \quad \text{and} \quad v_t = \omega \frac{X_0}{2} \quad (2.57)$$

And so the *K.E.* for the plate and the two horizontal trusses are

$$K.E._p = \frac{1}{2} v_p^2 M_p = \frac{1}{2} X_0^2 \omega^2 M_p \quad (2.58)$$

and

$$K.E._t = \frac{1}{8} X_0^2 \omega^2 M_t \quad (2.59)$$

The velocity profile of the beam segments is proportional to the mode shape at maximum displacement. The mode shape is taken as the static displacement curve under static loading, a common and sufficient assumption given that the beams do not resonate themselves. We first consider beam segment [AB] (Fig. 2.21). The equation of deflection [Eq. (2.43)] and one of the boundary conditions are repeated here for convenience:

$$x(y) = \frac{F_x}{48EI_z} (3Ly^2 - 2y^3) \quad \text{for } 0 \leq y \leq L \quad (2.60)$$

and

$$x(L) = \frac{X_0}{2} = \frac{F_x L^3}{48EI_z} \quad (2.61)$$

Substituting Eq. (2.61) into Eq. (2.60) to eliminate the F/EI_z term, we have

$$x(y) = \frac{X_0}{2} \left[3\left(\frac{y}{L}\right)^2 - 2\left(\frac{y}{L}\right)^3 \right] \quad (2.62)$$

So the velocity profile for segment [AB] is

$$v_b(y)|_{[AB]} = \frac{X_0}{2} \left[3\left(\frac{y}{L}\right)^2 - 2\left(\frac{y}{L}\right)^3 \right] \omega \quad (2.63)$$

leading to the *K.E.* for [AB] as

$$\begin{aligned} K.E._{[AB]} &= \frac{1}{2} \int_0^L \frac{X_0^2 \omega^2}{4} \left[3\left(\frac{y}{L}\right)^2 - 2\left(\frac{y}{L}\right)^3 \right]^2 dM_{[AB]} \\ &= \frac{X_0^2 \omega^2 M_{[AB]}}{8L} \int_0^L \left[3\left(\frac{y}{L}\right)^2 - 2\left(\frac{y}{L}\right)^3 \right]^2 dy \\ &= \frac{13}{280} X_0^2 \omega^2 M_{[AB]} \end{aligned} \quad (2.64)$$

where $M_{[AB]}$ is the mass of the segment [AB].

Similarly, we proceed with evaluating $K.E._{[CD]}$ by first finding the velocity profile:

$$v_b(y)|_{[CD]} = X_0 \left[1 - \frac{3}{2} \left(\frac{y}{L}\right)^2 + \left(\frac{y}{L}\right)^3 \right] \omega \quad (2.65)$$

Then

$$\begin{aligned} K.E._{[CD]} &= \frac{X_0^2 \omega^2 M_{[CD]}}{2L} \int_0^L \left[1 - \frac{3}{2} \left(\frac{y}{L}\right)^2 + \left(\frac{y}{L}\right)^3 \right]^2 dy \\ &= \frac{83}{280} X_0^2 \omega^2 M_{[CD]} \end{aligned} \quad (2.66)$$

where $M_{[CD]}$ is the mass of segment [CD], and is identical to $M_{[AB]}$. Since the total mass of the 8 parallel beams is M_b , we have

$$M_{[AB]} = M_{[CD]} = \frac{1}{8} M_b \quad (2.67)$$

Therefore,

$$\begin{aligned} K.E_{\cdot b} &= 4K.E_{\cdot [AB]} + 4K.E_{\cdot [CD]} \\ &= \frac{13}{560} X_0^2 \omega^2 M_b + \frac{83}{560} X_0^2 \omega^2 M_b \\ &= \frac{6}{35} X_0^2 \omega^2 M_b \end{aligned} \quad (2.68)$$

Collecting the results in Eqs. (2.58), (2.59) and (2.68) and substituting them into Eq. (2.56) yields

$$K.E_{\cdot \max} = X_0^2 \omega^2 \left(\frac{1}{2} M_p + \frac{1}{8} M_t + \frac{6}{35} M_b \right) \quad (2.69)$$

We now evaluate $P.E_{\cdot \max}$ as the work done to achieve maximum deflection:

$$P.E_{\cdot \max} = \int_0^{X_0} F_x dx = \int_0^{X_0} k_x x dx = \frac{1}{2} k_x X_0^2 \quad (2.66)$$

Equating the right-hand sides of Eqs. (2.69) and (2.70) yields the final result for the resonant frequency:

$$\begin{aligned} \frac{1}{2}k_x X_0^2 &= X_0^2 \omega^2 \left(\frac{1}{2}M_p + \frac{1}{8}M_t + \frac{6}{35}M_b \right) \\ \Rightarrow \omega &= \left(\frac{k_x}{M_p + \frac{1}{4}M_t + \frac{12}{35}M_b} \right)^{\frac{1}{2}} \end{aligned} \quad (2.71)$$

The denominator on the right-hand side of this equation can be lumped together as the effective mass of the system, M :

$$M = M_p + \frac{1}{4}M_t + \frac{12}{35}M_b \quad (2.72)$$

such that

$$\omega = \left(\frac{k_x}{M} \right)^{\frac{1}{2}} \quad (2.73)$$

2.3.1.4 Quality Factor

One of the advantages of laterally-driven resonant structures is that the damping in the lateral direction is much lower than in the vertical direction. Therefore, when operated in air, undesired vertical motions are conveniently damped. There are a number of dissipative processes during lateral motion, all of them affecting the quality factor Q . The dominant influences include Couette flow underneath the plate, air drag on the top surface, damping in the comb gaps and direct air resistance related to the thickness of the structure [48] (Fig. 2.26). For a micron-sized gap between the plate and the substrate, energy dissipation through Couette flow underneath the plate dominates strongly over air

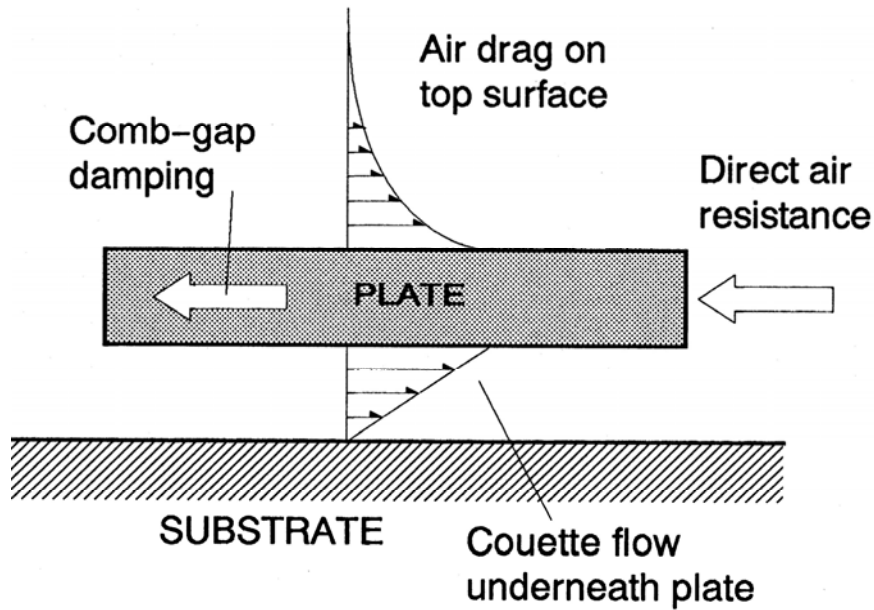


Figure 2.26 Major dissipative processes of a laterally-driven resonant plate.

drag on the top surface. If we consider Couette flow alone, then we can estimate the quality factor Q as [37,48]:

$$Q = \frac{d}{\mu A_p} \sqrt{M k_x} \quad (2.74)$$

where μ is the absolute viscosity of air (typically 1.8×10^{-5} N·s·m $^{-2}$), d is the offset between the plate and the substrate, and M is the effective mass of the resonator.

The other dissipative processes including air friction and turbulent flow generated

in the comb-finger gaps as well as direct air resistance are difficult to analyze. Since some of the comb-drive structures studied in this thesis are designed with as many as 18 movable comb fingers to maximize drive efficiency, air friction between the comb fingers may become the dominant factor in determining Q in air for these structures, and need to be evaluated experimentally [49]. Nevertheless, Eq. (2.74) serves as the upper bound for attainable Q in air.

When resonated in vacuum, vibrational energy is mostly dissipated to the substrate through the anchors [19], or in the polysilicon structure itself. The quality factor in vacuum can be further improved by employing tuning-fork design techniques such that the vibrating structures are dynamically balanced by being anchored only at the nodes of free oscillation [50].

2.3.2 Torsional Lateral Resonant Structures

Another class of structures is driven into torsional resonance by a set of concentric interdigitated electrodes. Figure 2.27 shows one of the designs with two Archimedean spirals as supporting beams. An advantage of the torsional resonant structures is that they are anchored only at the center, enabling radial relaxation of the built-in residual stress in the polysilicon film. Another benefit of the torsional approach is that four or more pairs of balanced concentric-comb structures can be placed at the perimeter of the ring, allowing a high degree of flexibility for differential drive and sense. Since both the drive and the sense ports are differentially balanced, excitation of undesired oscillation modes is avoided and signal corruption by feedthrough is minimized.

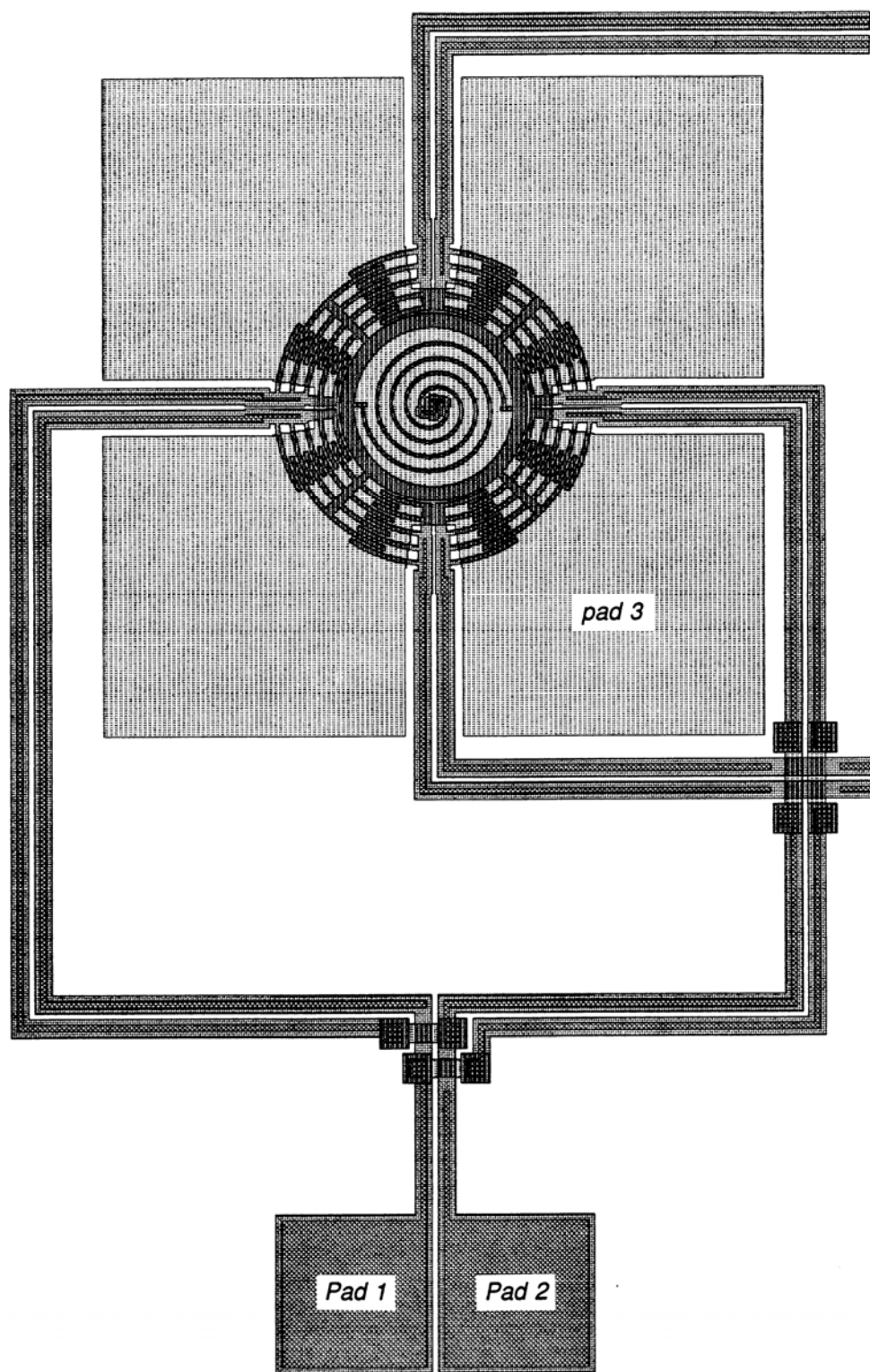


Figure 2.27 Layout of a torsional resonator with two spirals.

2.3.2.1 Spiral Support

The torsional spring constant of the Archimedean spiral is given by [51]:

$$k_\theta = \frac{EhW^3}{12L} \quad [\mu\text{N}\cdot\mu\text{m}\cdot\text{rad}^{-1}] \quad (2.75)$$

where L , W and h are the unfolded length, width and thickness of the spiral, respectively. The advantage of spiral spring is that high compliance can be achieved in a compact space. However, the spring is equally compliant in all directions on the x - y plane [51], making it less ideal as a support where motion restrictions in certain directions are needed.

2.3.2.2 Serpentine Support

An alternative to the spiral spring as a support for torsional resonators is the serpentine spring illustrated in Fig. 2.28. Finite-element program can be used conveniently to evaluate the spring constants for serpentine springs. *SuperSAP* [52] has been used extensively to simulate the spring constants of serpentine springs with various dimensions (Fig. 2.28). Unlike spiral springs, the compliance of serpentine springs is anisotropic. The spring constant along the length of the spring (k_r) is much higher than perpendicular spring constant (k_t). This is particularly advantageous as supports for torsional resonators, where translational motions are undesirable.

The simulation results for k_r and k_t are tabulated in Tables 2.II and 2.III. Increasing the number of meanders (N_m) at the expense of space improves the spring

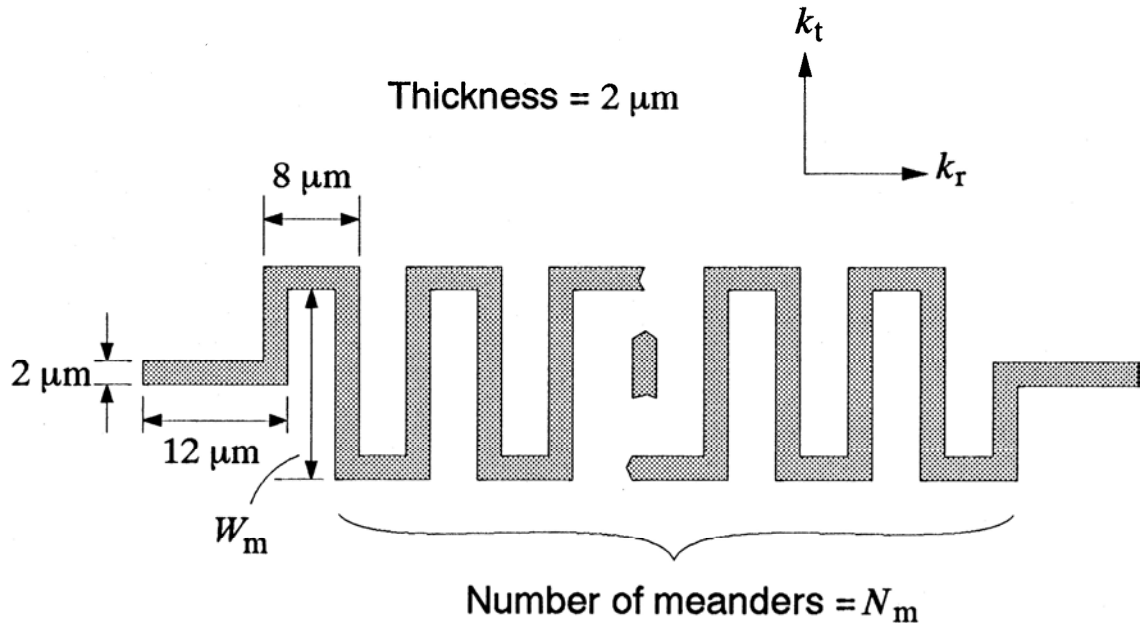


Figure 2.28 Dimensions of the serpentine spring.

constant ratio, k_r/k_t , and also minimizes k_t . Narrowing the meander width (W_m) improves k_r/k_t , but k_t also becomes higher. The spring constant ratio reaches the maximum in the limiting case of $W_m = 0$, where the spring becomes a cantilever beam. For practical design consideration, both the number of meanders (N_m) and W_m should be chosen to obtain an optimally small k_t and a sufficiently large k_r/k_t ratio.

Table 2.II Simulation results of serpentine springs
with $W_m = 28 \mu\text{m}$, and a $2 \mu\text{m} \times 2 \mu\text{m}$ cross section

	$N_m = 8$	$N_m = 10$	$N_m = 12$	$N_m = 14$	$N_m = 16$
$k_r [\text{nN}\cdot\mu\text{m}^{-1}]$	5090	4070	3390	2910	2540
$k_t [\text{nN}\cdot\mu\text{m}^{-1}]$	88	49	30	19	13
k_r/k_t	58	83	113	153	195

Table 2.III Simulation results of serpentine springs
with $N_m = 8$ at different $W_m [\mu\text{m}]$

	$W_m = 8$	$W_m = 12$	$W_m = 16$	$W_m = 20$	$W_m = 28$
$k_r [\text{nN}\cdot\mu\text{m}^{-1}]$	123000	45100	22100	12400	5090
$k_t [\text{nN}\cdot\mu\text{m}^{-1}]$	233	171	139	117	88
k_r/k_t	528	264	159	106	58

2.3.2.3 Resonant Frequency and Quality Factor

The torsional resonant frequency, ω_θ , is evaluated similarly as the linear resonators, replacing the x - y coordinates with the r - θ coordinates. In this case, k_x in Eq. (2.71) is replaced with the torsional spring constant, k_θ , and the masses, M_p , M_t , and M_b with the mass moments of inertia of the plate and the spiral spring, J_p and J_s :

$$\omega_\theta = \left(\frac{k_\theta}{J_p + \frac{1}{3}J_s} \right)^{\frac{1}{2}} \quad (2.76)$$

The value of k_θ is different from k_t , and can be approximated with the same simulation

program. The value of J can be found by evaluating the following integral over the surface area of the structure or the spring:

$$J = \int r^2 dM = \rho h \iint r^3 d\theta dr \quad (2.77)$$

where ρ is the density of polysilicon ($2.3 \times 10^3 \text{ kg}\cdot\text{m}^{-3}$).

The quality factor is estimated similarly to Eq. (2.74) by assuming Couette flow underneath the plate to be the dominant dissipation, and is given by

$$Q = \frac{d}{\mu \int r^2 dA_p} \sqrt{J k_\theta} \quad (2.78)$$

The same consideration concerning the role of air friction between the comb fingers applies.

2.4 SUMMARY

We have discussed the first-order theory for the electrostatic characteristics of comb-drive structures with respect to both the normal lateral mode of vibration as well as vertical levitation effects. The results of these analyses form the foundation for designing laterally-driven actuators with controlled vertical motion. The linearity of the lateral mode and the frequency-shifting effect of the vertical mode greatly simplify the mode-decoupling procedures. Differential biasing on alternating comb drive fingers can be employed to suppress dc levitation by an order of magnitude. Finally, the mechanical-spring supports including the folded-beam suspension for linear resonators and the spiral and serpentine springs for torsional-resonant structures are analyzed. The folded-beam support (and the extension to n -tuple-folded beams) is particularly advantageous for large-displacement linear actuator applications.

Chapter 3

LATERAL STRUCTURE FABRICATION

The fabrication process for the electrostatic-comb drives and associated lateral structures is a straightforward application of the surface-micromachining technology. Both plasma and wet-chemical etchings are used to define features on different low-pressure chemical-vapor-deposited (LPCVD) thin films, concluding with a final removal of a sacrificial layer to free the suspended microstructures. This chapter highlights the important processing steps, followed by a discussion on various performance-related fabrication issues. The step-by-step process flow is detailed in Appendix A.

3.1 FABRICATION SEQUENCE

The structures are fabricated with the five-mask process illustrated in Fig. 3.1 [38,39]. A significant advantage of this technology is that all the critical features are defined with one mask, eliminating errors due to mask-to-mask misalignment. The process begins with a standard POCL_3 blanket $n+$ diffusion, which defines the substrate ground plane, after which the wafer is passivated with a layer of 1500 Å-thick LPCVD nitride deposited on top of a layer of 5000 Å-thick thermal SiO_2 . Contact windows to the substrate ground plane are then opened [Fig. 3.1(a)] using a combination of reactive-ion etching (RIE) in an SF_6 plasma and wet etching in 5:1 buffered-HF bath.

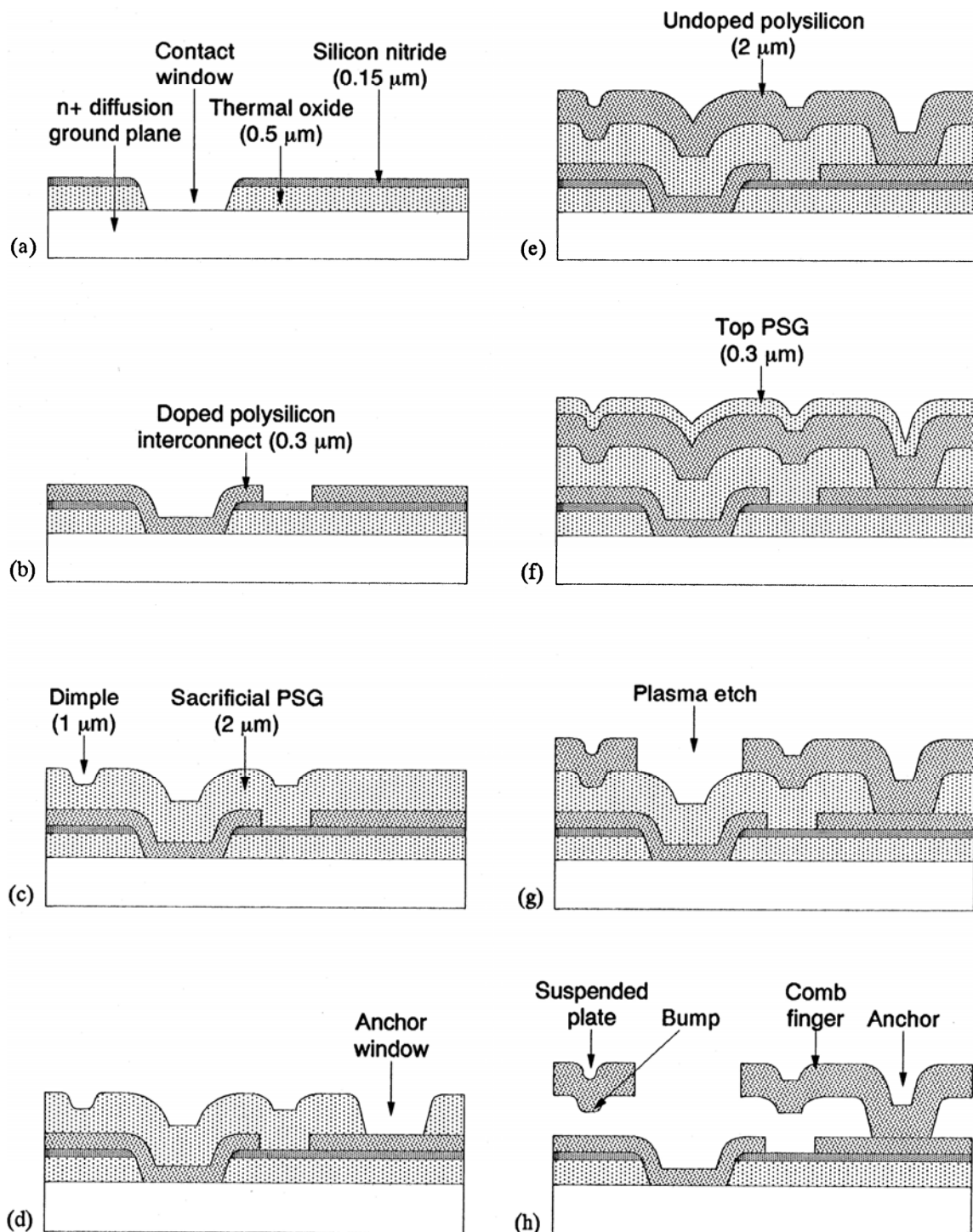


Figure 3.1 Process sequence of a lateral resonant structure.

The next steps involve deposition and definition of the first polysilicon layer. A layer of 3000 Å-thick, *in situ* phosphorus-doped polysilicon is deposited by LPCVD at 650°C then patterned with the second mask by RIE in a CCl₄-O₂ plasma [Fig. 3.1(b)]. This layer serves as an electrostatic shield, contact to the *n*⁺ diffusion, and electrical interconnection. A 2 μm-thick LPCVD sacrificial phosphosilicate glass (PSG) layer is deposited and densified at 950°C for one hour [Fig. 3.1(c)], followed by the third and fourth masking steps on this layer. The third one defines the 1 μm-deep, 2 μm × 2 μm dimples [Fig. 3.1(c)] formed by timed-etch in a CHF₃-CF₄ plasma, which serve as molds for forming the standoff bumps on the underside of the second polysilicon layer. These standoff bumps help reduce sticking of the structural-polysilicon layer to the substrate after the final wet-etching step [8]. The anchors of the microstructures to the underlying polysilicon interconnection [Fig. 3.1(d)] are then patterned with the fourth mask; first with RIE, then with wet etching.

The 2 μm-thick, undoped polysilicon structural layer is then deposited by LPCVD at 610°C [Fig. 3.1(e)]. The structural layer is doped by depositing another layer of 3000 Å-thick PSG [Fig. 3.1(f)] and then annealing at 1050°C in N₂ for one hour. This doping process is designed to dope the polysilicon symmetrically by diffusion from the top and the bottom layers of PSG, and to simultaneously stress anneal the layer. The annealing temperature is lower than 1100°C in order to avoid loss of adhesion between the PSG and the Si₃N₄ layer [35,53].

After stripping the top PSG layer in buffered HF, the plates, beams and

electrostatic-comb drive and sense structures are defined in the final masking step [Fig. 3.1(g)]. The structures are anisotropically patterned by RIE in a CCl_4 plasma, in order to achieve nearly vertical sidewalls. Figure 3.1(h) illustrates the final cross section after the wafer is immersed in 5:1 buffered HF to remove the sacrificial PSG. The wafer is then left immersed in stagnant deionized (DI) water for at least two hours [54] followed by repeated rinse until water resistivity reaches $16 \text{ M}\Omega\text{-cm}$. The process concludes with drying the wafer under an IR lamp for 10 minutes. Figures 3.2-3.10 are scanning-electron and optical micrographs of the completed structures.

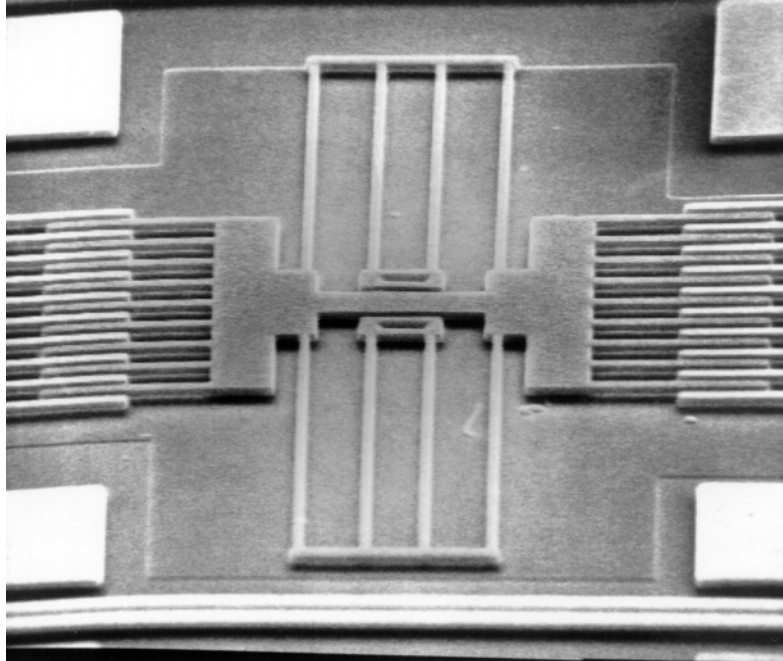


Figure 3.2 SEM of a linear resonator with $140 \mu\text{m}$ -long folded beams.

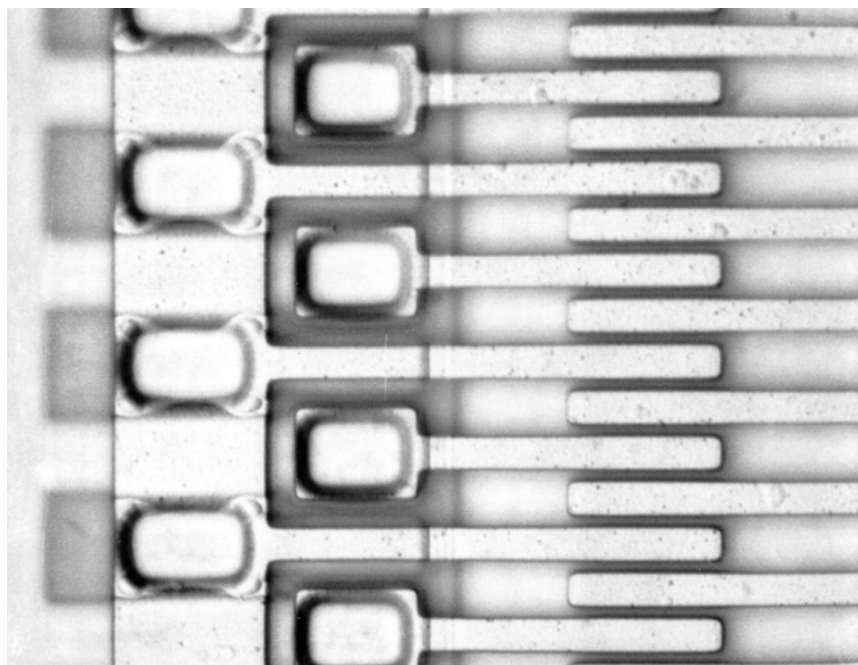


Figure 3.3 Optical micrograph of the alternating-comb structure with striped ground conductors underneath the comb fingers.

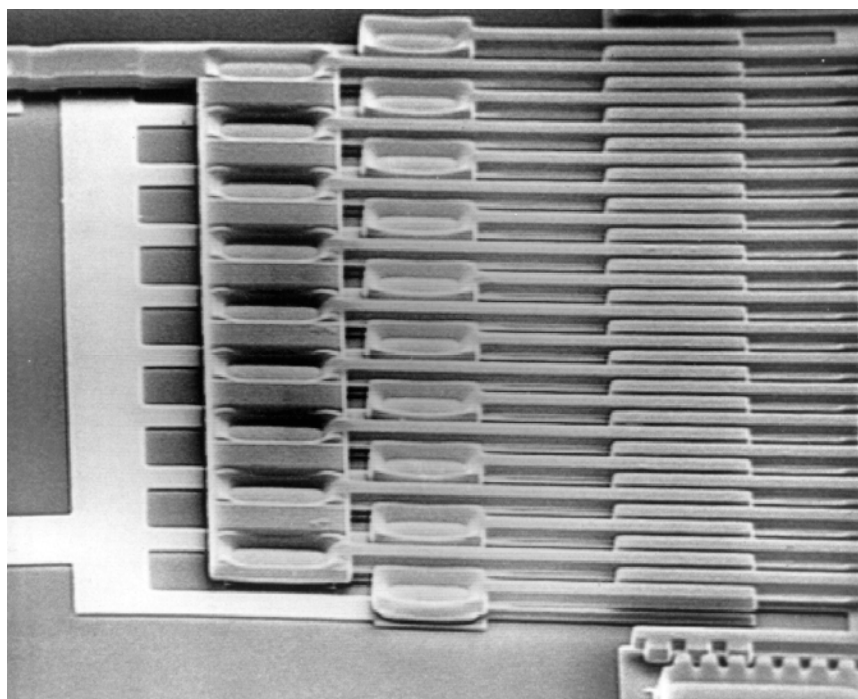


Figure 3.4 SEM of the alternating-comb drive showing the crossover structure.

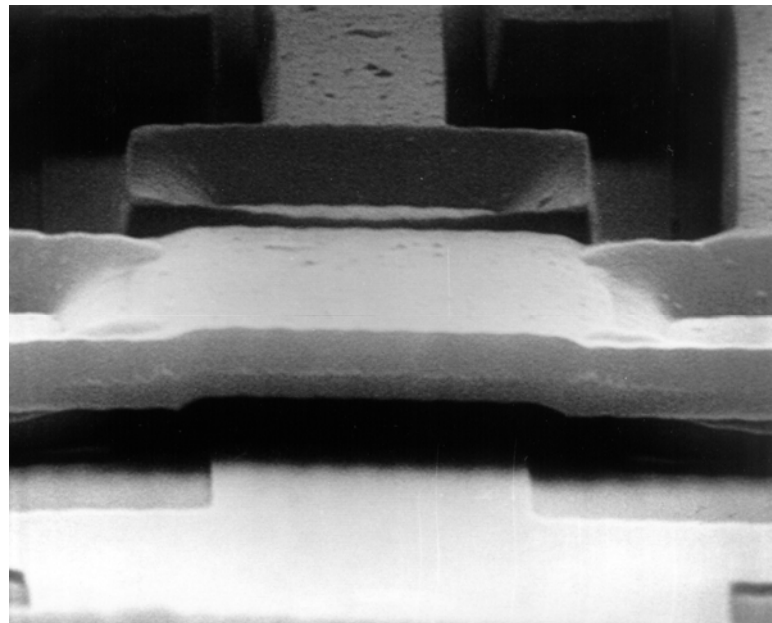


Figure 3.5 SEM of the close-up view of the crossover structure.

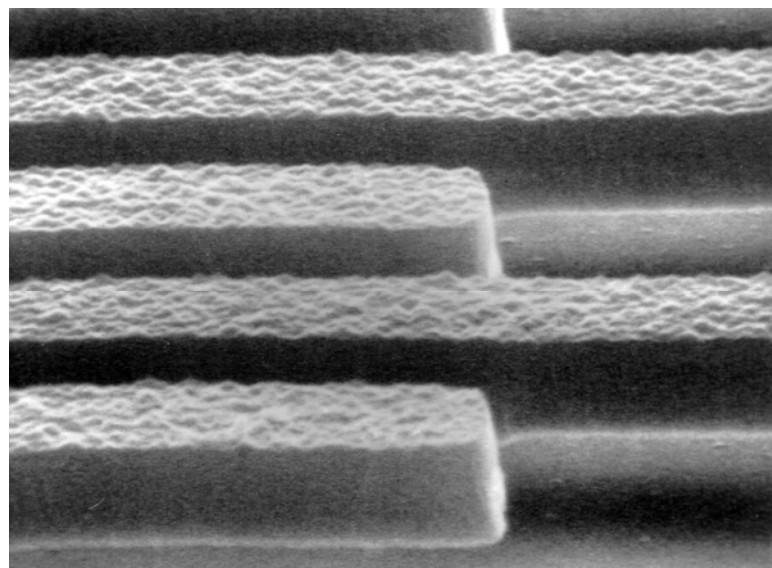


Figure 3.6 SEM of the close-up view of the linear comb-drive fingers, showing the surface topography of the deposited polysilicon film.

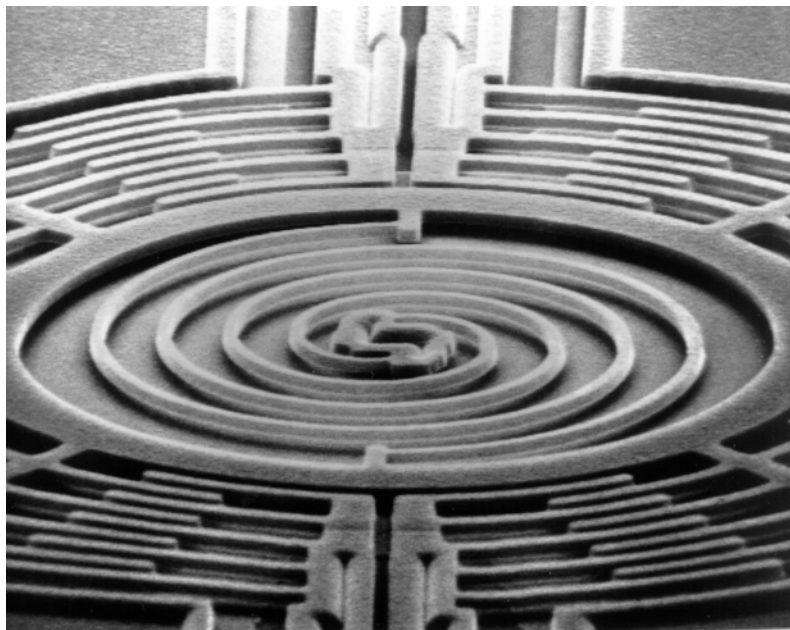


Figure 3.7 SEM of two, two-turn Archimedean spirals supporting a torsional resonant plate.

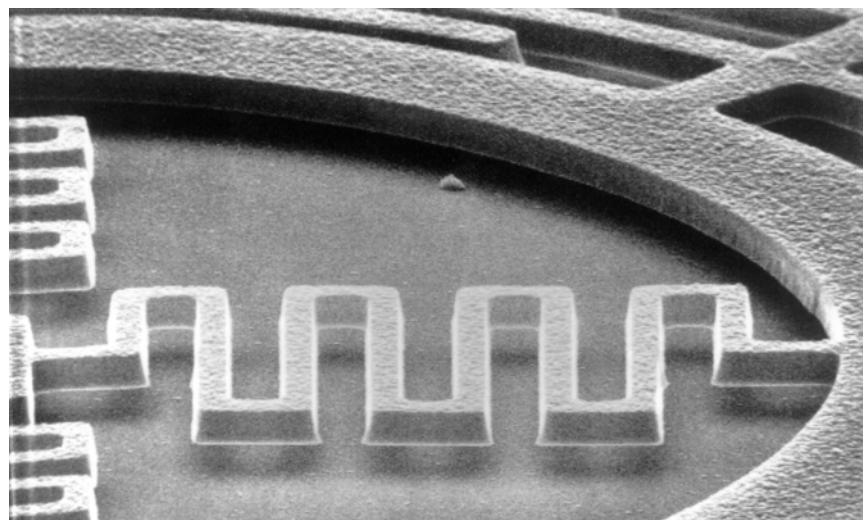


Figure 3.8 SEM of one of the four serpentine springs supporting a torsional resonant plate.

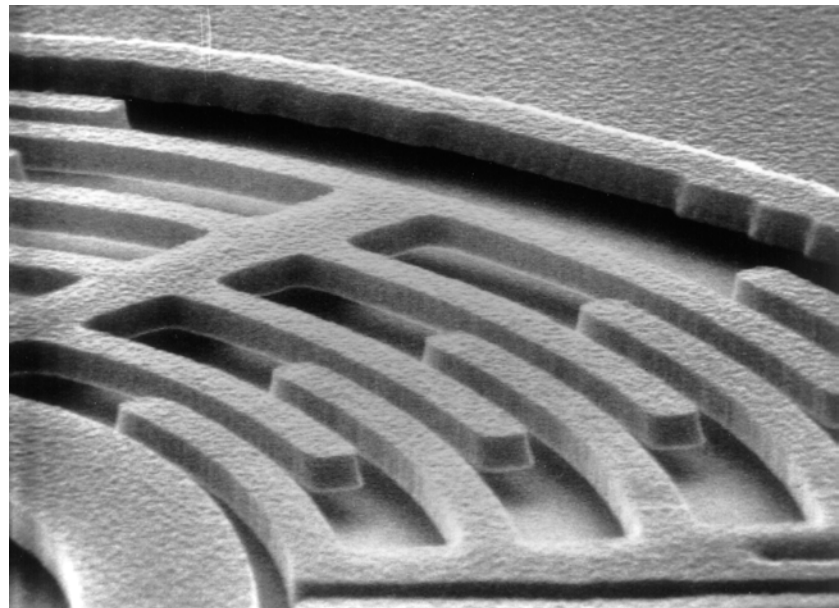


Figure 3.9 SEM of the concentric comb structure.

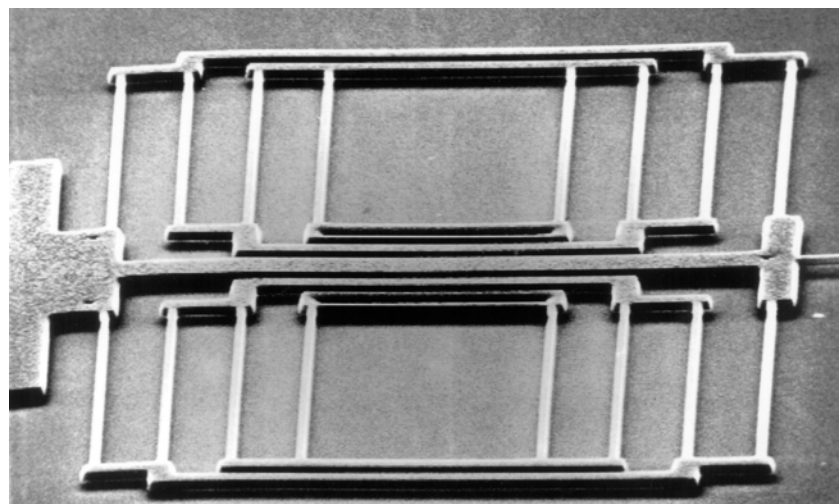


Figure 3.10 SEM of a structure supported by a pair of double-folded beams.

3.2 FABRICATION CHARACTERISTICS AND PERFORMANCE

Having described the fabrication sequence, we now identify and discuss several important processing issues that affect the yield and performance of the finished structures.

3.2.1 Thin-Film Stress Consideration and Control Method

Residual stress in LPCVD polysilicon thin films has been a major design limitation for micromechanical devices, which has motivated many research efforts for its characterization and control [55-61]. In particular, the presence of strain gradients through the thickness of the structural film results in suspended microstructures deflecting towards or away from the substrate. Constrained structures, such as clamped-clamped beams, buckle under compressive stress in the film [55].

The microstructures studied here can stick to the substrate after the final drying process [62]. The yield of free-standing structures is zero on wafers for which the one-hour stress anneal at 1050 °C is omitted (Fig. 3.11). When the stress anneal is included in the process, 70% of the structures are free-standing. Most of the 30% which are initially attached to the substrate are without standoff bumps, and can be easily freed with a probe tip; the high flexibility of the structures allows manipulation without breakage. No amount of probing, however, can free any of the unannealed structures.

A series of clamped-clamped diagnostic microbridges (Fig. 3.12) is included in the design to estimate the average residual strain in the structural polysilicon film from the minimum buckling length [56]. The moment of the residual strain is quantitatively

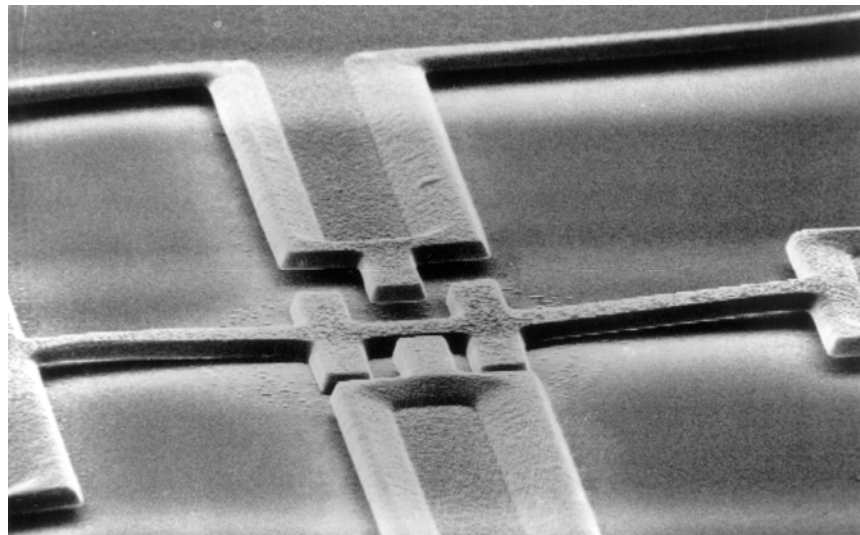


Figure 3.11 SEM of a constrained structure fabricated without stress anneal.



Figure 3.12 SEM of a set of clamped-clamped diagnostic bridges, each beam is 10 μm wide and 2 μm thick, with the length varying from 100 μm to 300 μm .

studied by a series of clamped-free cantilever beams. Since the microbridges have “step-up” anchors, it is expected that end effects will have to be modeled carefully to obtain an accurate value of the residual strain [57]. Moreover, the sticking of the diagnostic microbridges and cantilevers to the substrate during drying is also a source of error in calculating the strain and its moment [63].

For the unannealed samples, the cantilevers longer than 150 μm have a tendency to deflect and attach to the substrate, while the minimum buckling length for microbridges is about 120 μm (Fig. 3.13). Using Euler's simple criterion for buckling a clamped-clamped beam [56], the strain is estimated to be 10^{-3} . Annealed samples have apparently undeflected cantilevers under optical and SEM observation and have a buckling length of about 220 μm (Fig. 3.14), indicating a residual strain of about 3×10^{-4} . These estimated values are typical of residual strain for phosphorus-doped polysilicon [56].

However, annealing temperatures higher than 1100°C may adversely affect the adhesion of PSG to stoichiometric-nitride passivation layer; and PSG on top of silicon-rich nitride blisters at temperature higher than 1000°C. Figure 3.15 shows a wafer with PSG on silicon-rich nitride damaged as a result of annealing at 1050°C for one hour. Furthermore, if CMOS devices are present, the temperature ceiling is further reduced to less than 900°C [64], where stress annealing is ineffective. Other processing approaches such as rapid-thermal annealing (RTA) [65] or the use of as-deposited low-stress polysilicon film [61] are possible alternatives.

Although stoichiometric nitride is preferred if high annealing temperature cannot

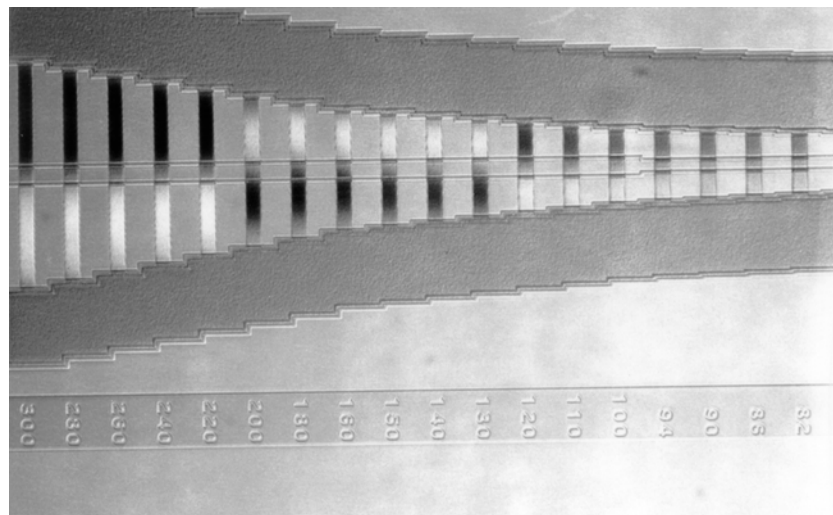


Figure 3.13 Optical micrograph of a set of diagnostic microbridges from an unannealed wafer. Nomaski illumination reveals that bridges 120 μm and longer are buckled.

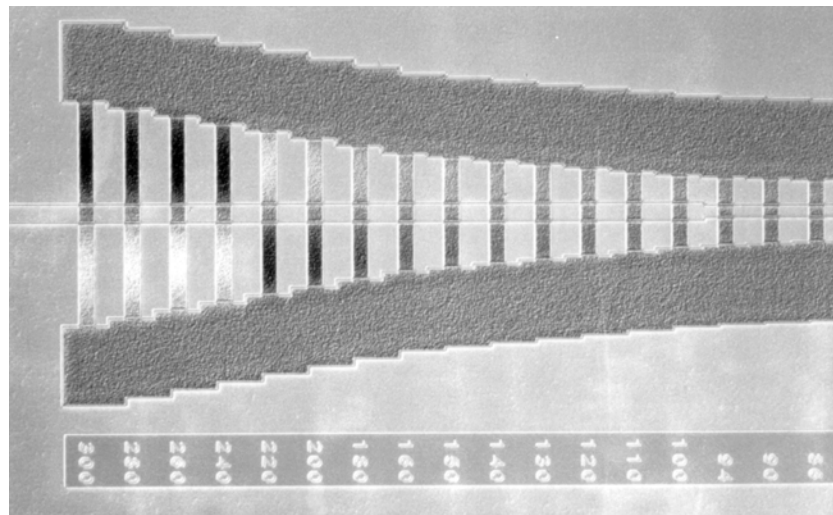


Figure 3.14 Optical micrograph of a set of microbridges from an annealed wafer. Nomaski illumination shows a buckling length of 220 μm .

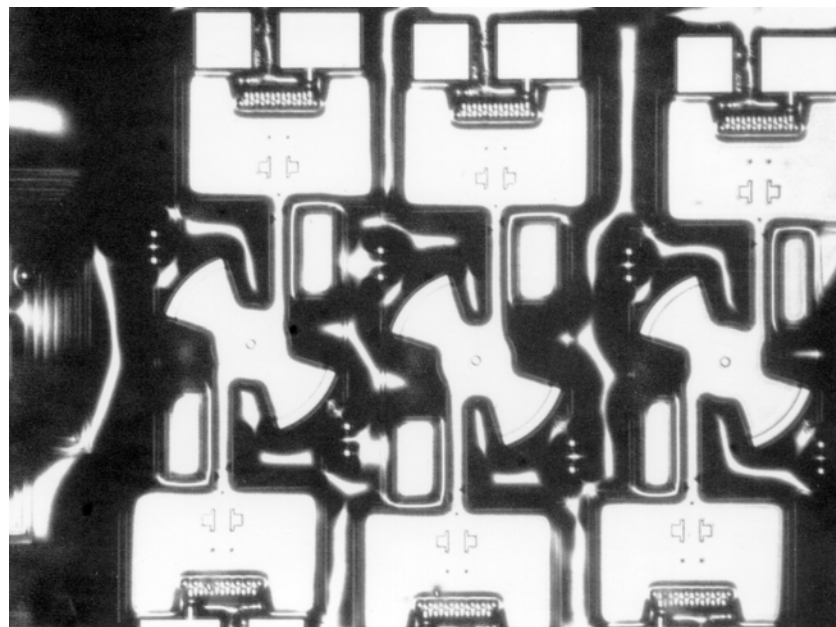


Figure 3.15 Optical micrograph of a wafer with PSG blistering on top of silicon-rich nitride as a result of one-hour annealing at 1050 °C.

be avoided, the highly tensile built-in stress within the film limits the thickness to less than 2000 Å. Silicon-rich nitride layer is attractive as an alternative passivation layer especially when extended etching in an HF bath is required in subsequent processing. Because of its relatively low built-in stress, silicon-rich nitride film can be as thick as 1.5 μm without cracking or peeling. The etch rates of $20 \text{ \AA} \cdot \text{min}^{-1}$ for stoichiometric nitride and $15 \text{ \AA} \cdot \text{min}^{-1}$ for silicon-rich nitride in 5:1 buffered-HF bath can be used as a guideline in selecting either types of nitride. The recipes for depositing stoichiometric and silicon-rich nitride are detailed in Appendix A.

3.2.2 Thin-Film Etching and Vertical Sidewalls

Besides the ability to deposit films with thicknesses on the order of 2 μm with controlled built-in stress, another factor that is critical to the success of fabricating surface-micromechanical devices is the use of reactive-ion etching to etch near-vertical sidewalls for microstructures. For example, the drive efficiency of the electrostatic comb will be degraded if the sidewalls of the comb fingers that form the capacitor are not parallel (Fig. 3.16).

As a prerequisite, parallel-electrode plasma etchers with adjustable plate gap are used instead of barrel etchers for faster and more vertical etching. Two etchers by *LAM Research* are used for etching oxide and polysilicon films separately to avoid cross-contamination from etch products, while the less critical nitride etch is done in a *Technics Inc.* etcher. The nitride etch uses SF_6 , and is more isotropic than the oxide or polysilicon

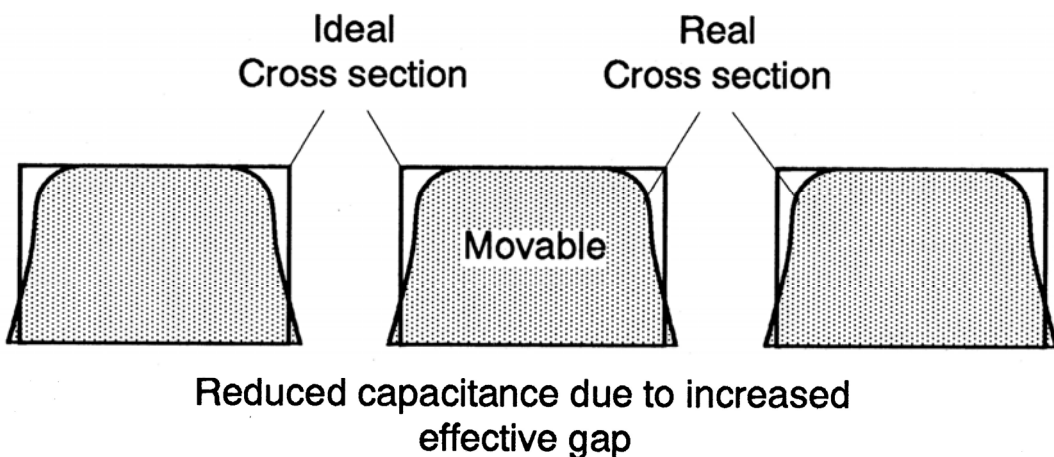


Figure 3.16 Cross section of the comb fingers as a result of nonideal plasma etching, reducing the drive efficiency.

etches.

For critically long etch steps such as those needed to open anchor windows for the microstructures through the 2 μm -thick sacrificial-PSG layer and for patterning the structural-polysilicon films, double photoresist layers (2 μm thick), hardened by baking at 120°C for at least 5 hours, are used as the etch mask. Also, we repeat several short etch steps between 30-second to 1-minute duration with at least one minute idle between etches to avoid excessive heat buildup [54]. If the reactive interface is allowed to heat up in a long etch step, the masking photoresist will erode prematurely and the etch rate becomes unpredictable. The radio-frequency (RF) power, the flow rates of different gases and the electrode gap are optimized to obtain the most vertical sidewalls with sufficient selectivities with respect to the photoresist and the underlying film. The optimized recipe is detailed in Appendix A. Other work done at Berkeley has used a thin-PSG layer as a mask for etching 2 μm -thick undoped polysilicon films with promising results [66–68].

When etched in a $\text{CHF}_3\text{-CF}_4$ plasma, the selectivity of PSG with respect to either silicon or silicon nitride is poor. Therefore, with a carefully characterized etch rate before each run, the etch is timed to leave about 3000 Å or more of PSG, which is subsequently removed by a highly selective timed etch in a 5:1 buffered-HF bath. Another complication is that small windows are etched slower than bigger ones in the reactive-ion etcher. A 5 μm \times 5 μm opening may be cleared at only half the rate of a completely exposed PSG film. Longer wet-etch time must be allowed to clear contact holes of all sizes. Therefore, a maximum of 1 μm undercut on anchor contacts may result, which must be compensated

for in the design rules. PSG layers that have not been densified at 950°C after deposition etch at a rapid and variable rate in buffered HF, which makes them unsuitable for this application.

Similarly, etching the passivation nitride layer (stoichiometric or silicon-rich) in an SF₆ plasma suffers from the problem of poor selectivity with respect to SiO₂ and silicon etches. As a matter of fact, bulk silicon is etched slightly faster than nitride in an SF₆ plasma. It is found that with SF₆ flowing at 13 sccm and He at 21 sccm with RF power set to 200 W, nitride is etched at about 1000 Å·min⁻¹, Si at 1200 Å·min⁻¹, and SiO₂ at 600 Å·min⁻¹. Fortunately, the stress-relief 5000 Å-thick thermal oxide layer between the nitride film and the substrate also serves as a buffer to prevent attack of the bulk silicon in case of nitride etch-through.

The selectivity problem of CHF₃-CF₄ etching makes it necessary to include a final wet-etch step when anchor windows are opened through the PSG layer, resulting in a tapered profile on the contact-hole sidewalls. Tapered windows necessitate relaxed design rules; however, they also relax the step-coverage required for subsequent deposition of the structural-polysilicon film. Microstructures have been successfully fabricated with anchors opened exclusively with buffered-HF etch (Fig. 3.17).

However, the drawback with a wet-etch-only approach is that all contact holes have rounded corners. Although the 2 μm undercut around the perimeters of the windows can be compensated by modifying the design rules, the minimum contact window area is larger. Furthermore, as with wet-etching techniques in general, adhesion of photoresist

to the PSG layer is critical. Care must be taken not to expose the wafer to acetone, as is usually done when photoresist layers are removed. Instead, ashing photoresist in an oxygen plasma is recommended if the wafer needs to be subsequently recoated with photoresist [69]. Hardening the photoresist at 120°C for at least 5 hours prior to wet etching also improves the adhesion, besides slowing the photoresist-erosion rate in plasma etchers.

The selectivity of polysilicon with respect to oxide etch in a CCl₄-O₂ plasma is very good, enabling automatic end-point detection and overetch to completely clear out narrow gaps between critical features. For a 2.7 μm-thick polysilicon layer, the smallest gap resolvable in the etcher is slightly less than 2 μm by allowing a 30% overetch.

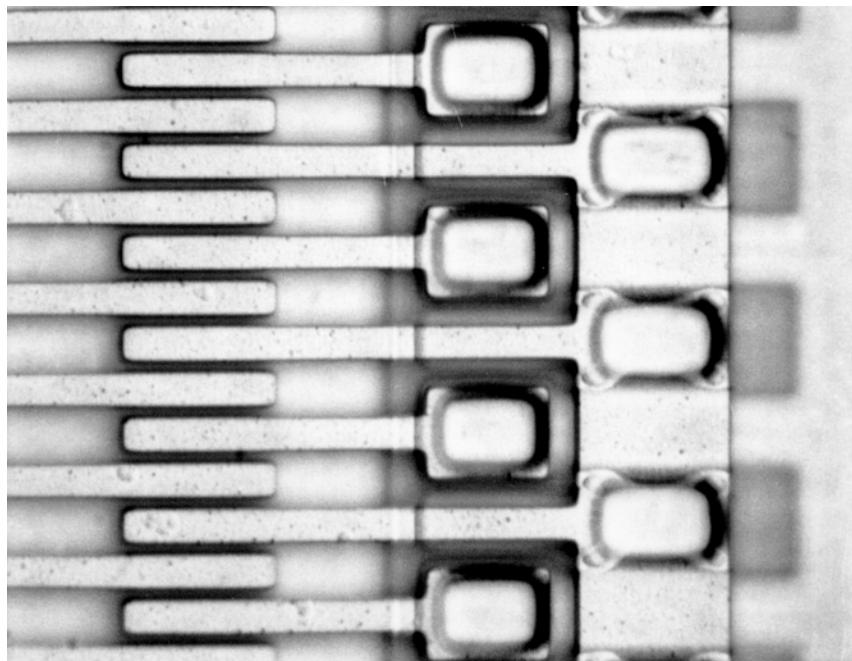


Figure 3.17 Optical micrograph of a structure with enlarged anchors as a result of wet etching.

Although increased overetch may clear out even smaller gaps, the resulting extended photoresist erosion may cause rounding of the top edges and loss in feature resolution.

3.2.3 Single-Mask Process

The power and flexibility of the lateral-drive approach can be further demonstrated with the single-mask process. Since all the critical features of the basic electrostatic-comb drive are fabricated out of the same structural polysilicon layer, it is possible to include only one photolithography step in the process to built a functioning comb structure, as illustrated in Fig. 3.18.

The fabrication steps are similar with the complete process flow described in section 3.1 with two exceptions. First, all lithography steps other than the one required to pattern the structural polysilicon layer are omitted. Second, the final sacrificial etch with buffered HF is carefully timed to free the moving parts of the structures but leave some PSG under the polysilicon layer as pedestal anchors. The layouts of the structures are redesigned to include large pad areas where PSG pedestals are needed, and etch holes are distributed over the moving parts to ensure their quick release. Figure 3.19 is a sample layout of a single-mask resonator.

Besides simplicity in processing, quick turn-around and high yield, single-mask resonators offer additional advantages. With the absence of anchor windows, extended PSG etching in plasma and step-coverage problems are eliminated. The sacrificial PSG layers can then be made as thick as the deposition step allows, increasing the distance

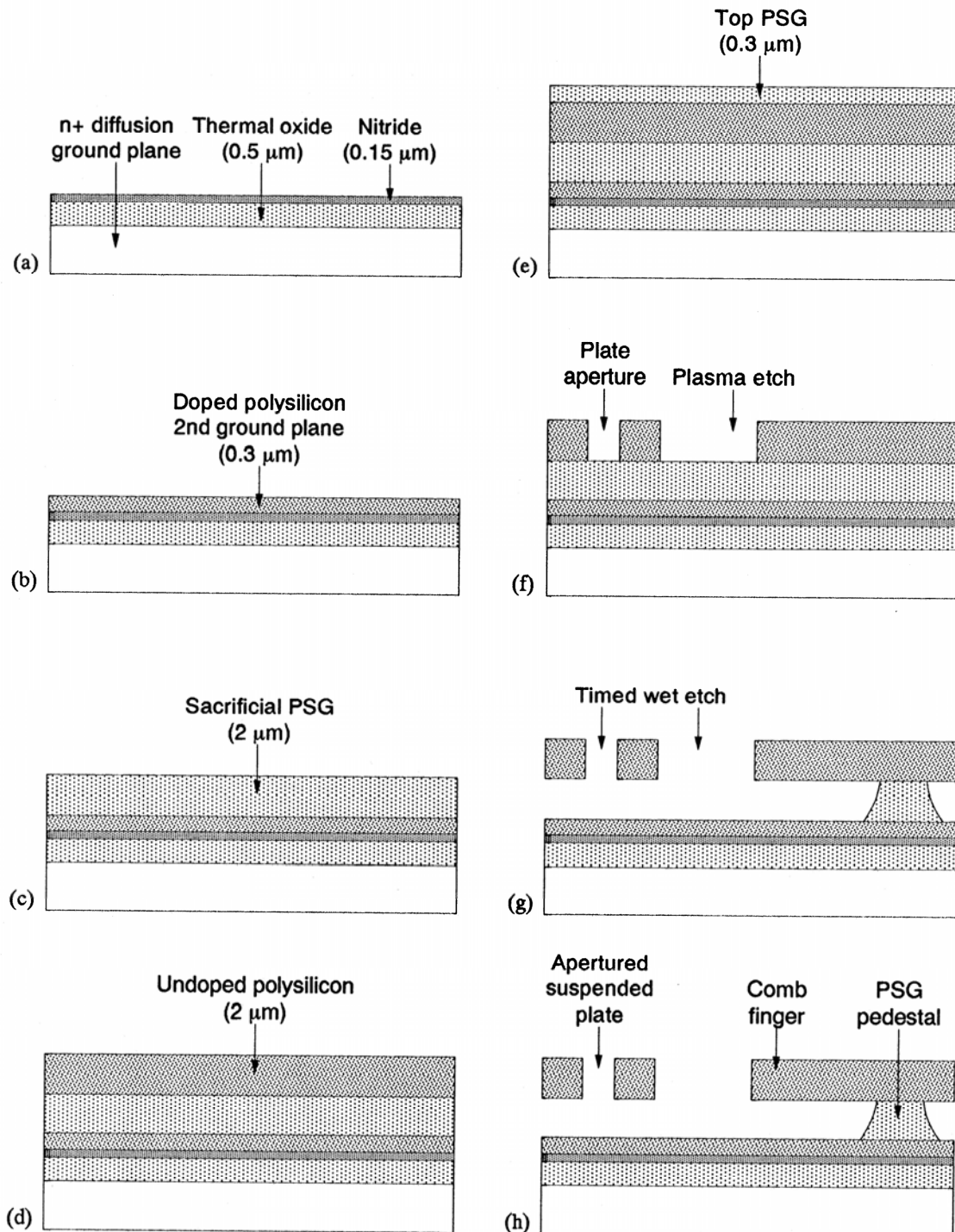


Figure 3.18 Single-mask processing steps.

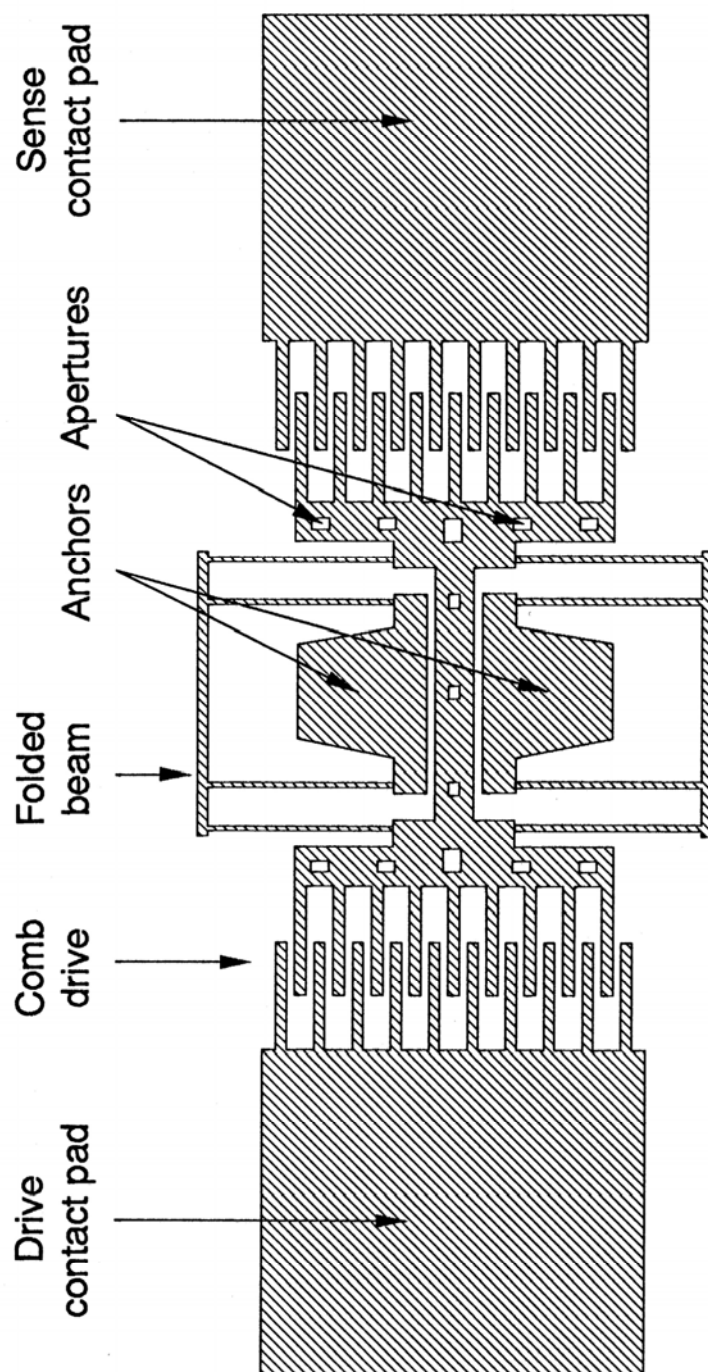


Figure 3.19 Layout of a single-mask resonator.

between the resonator and the substrate ground plane. Damping due to air drag (Couette flow) underneath the resonant plate is minimized (see sections. 2.3.1.3 and 2.3.2.3), and the induced levitation force on the structure from the image charges on the ground plane becomes less significant (see section 2.2.1).

The drawbacks, however, are that the big pads required to form the PSG pedestals preclude a compact resonator design, and crossovers for electrical isolation to form the differentially-balanced, alternating-comb drives (see section 2.2.5) are no longer available. Nevertheless, for certain applications such as diagnostic test structures for material properties, the fabrication simplicity may far outweigh these shortcomings.

Besides polysilicon as structural material and PSG as sacrificial layer, other alternatives exist that involve different technologies. These possibilities are explored in the final chapter.

3.3 SUMMARY

In this chapter, we have described the polysilicon surface-micromachining techniques for fabricating the laterally-driven microstructures. The five-mask process involves standard equipments available in a conventional IC-fabrication laboratory. The performance of the finished structures is critically dependent on the mechanical characteristics of the deposited polysilicon layer, especially the built-in stress within the film. The effects of stress annealing at high temperature and the final sacrificial etch affect the choice of the passivation nitride layer. Different combinations of plasma- and wet-etching techniques are optimized to obtain the most vertical sidewalls. Finally, we have described the single-mask process that offers the advantages of simplicity and functionality to demonstrate the power and flexibility of the lateral-drive approach.

Chapter 4

TESTING TECHNIQUES AND RESULTS

This chapter presents a collection of the test results from three different process runs. The first run includes both linear and torsional resonator prototypes with different characteristics to verify the basic principles of the lateral-drive approach and to demonstrate fabrication feasibility [38]. The second test chip is used to further characterize the electromechanical behaviors of the comb-drive structures [39]. The final test run is dedicated to study the vertical mode of motions and to compare the effectiveness of various control methods [40]. The experimental results from these three runs are organized to parallel Chapter 2, in which we have developed the first-order theory for both the lateral and vertical modes of operations of the electrostatic-comb drive.

The testing techniques involved in these experiments are first described. We then discuss the experimental results of the lateral motions of the linear and torsional resonators, followed by an analysis of the data collected on the vertical behavior of the microstructures. We are mainly interested in the resonant frequencies and quality factors of different resonator prototypes, from which we deduce the Young's modulus of the polysilicon film used and verify the first-order theory developed in Chapter 2.

4.1 TESTING TECHNIQUES

Since the vibration amplitudes of the resonators are sufficiently large (as much as 10 to 20 μm laterally), direct observations under a microscope as well as inside a scanning-electron microscope (SEM) can be used to collect reasonably accurate data. Electrical testing techniques that circumvent direct-signal feedthrough are developed to objectively verify the observed results.

4.1.1 Direct Observations

An optically-based, wafer-level test setup includes a probe station with a set of zoom objectives capable of 1000 \times maximum magnification, four probe-tip manipulators, and a video camera. The optical-light source assembly can be optionally modified and replaced with a stroboscopic light, the frequency of which can be triggered externally. Signals are fed to the wafer under test through a series resistor ($\geq 1 \text{ M}\Omega$) to provide short-circuit protection. The electronic equipment used is conventional, including dc voltage sources with a maximum output of 50 V, function generators capable of 1 MHz sinewave output at 10 V zero-to-peak amplitude, digital multimeters, and oscilloscopes.

Both sinusoidal and dc bias voltages are applied to the structures via probes contacting the numbered polysilicon pads, as illustrated in Figs. 4.1 and 4.2. For the linear structures, the sinusoidal drive voltage is applied to one set of fixed electrode fingers via *pad 1*, while a dc bias is supplied to *pad 2* (connected to the dormant sense fingers) and *pad 3* (connected to the first-level polysilicon ground plane and to the

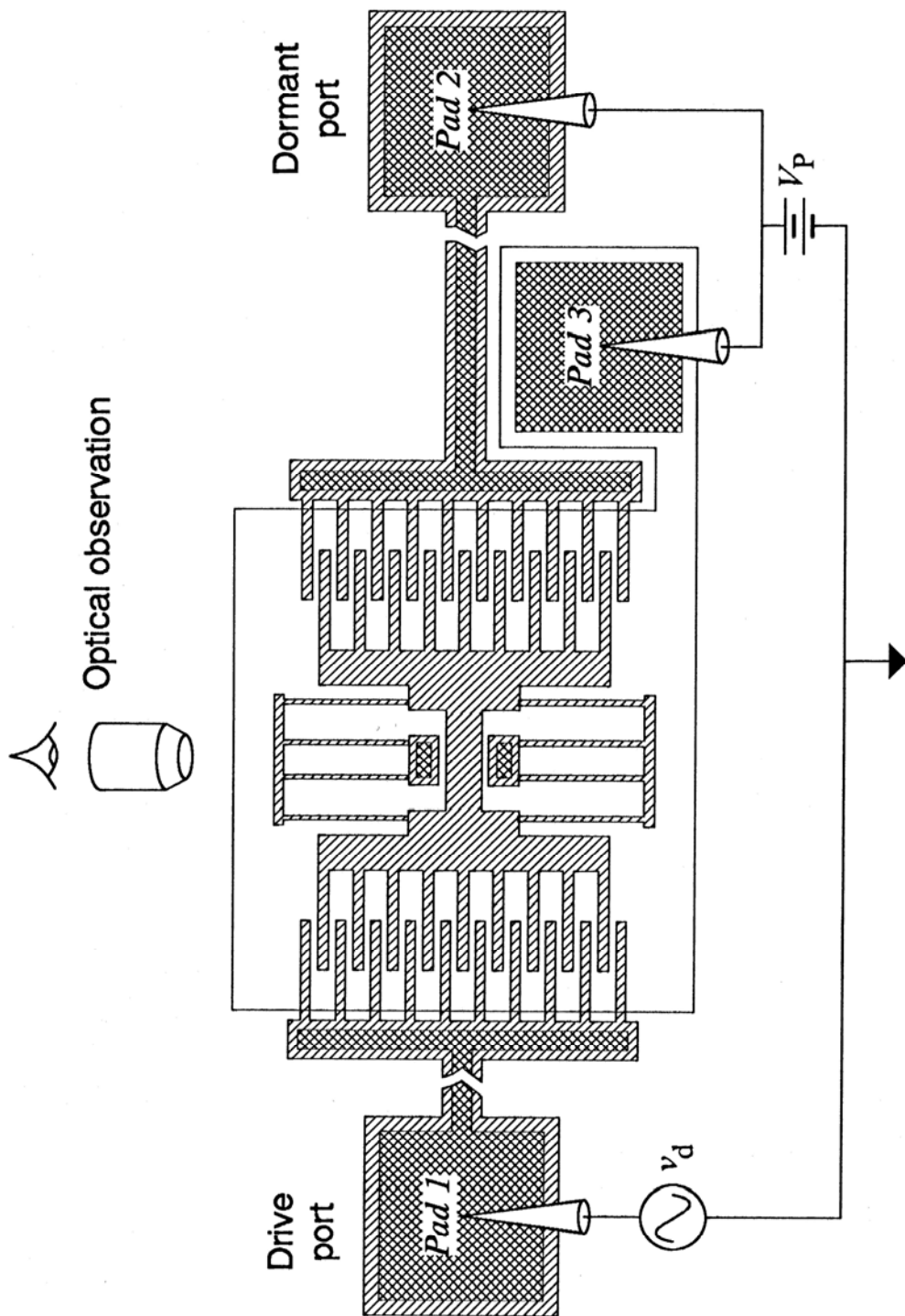


Figure 4.1 Test setup for a linear resonator.

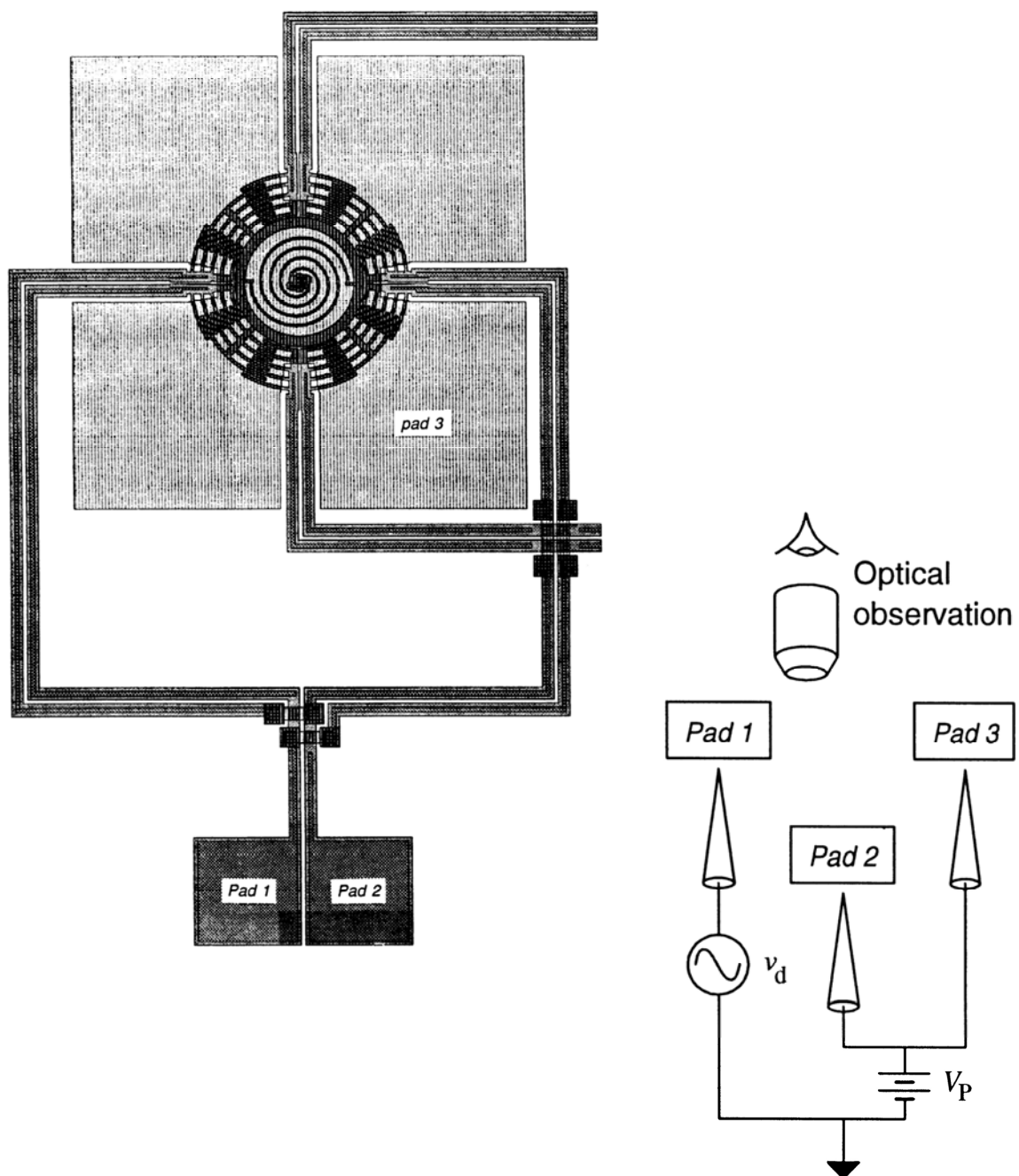


Figure 4.2 Test setup for a torsional resonator.

suspended structure through the folded-beams). The diffused ground plane is electrically tied to the first polysilicon layer through a contact window (not shown in the drawing). For the torsional structure in Fig. 4.2, the sinusoidal voltage is applied to the drive fingers via *pad 1*, and the dormant sense fingers, ground plane and resonant structure are biased via *pad 2* and *pad 3*.

In order to provide large-amplitude lateral motion in air for visual observation, dc biases of up to 40 V and drive-voltage amplitudes (zero-to-peak) of up to 10 V are used. Resonant frequencies are determined by tuning the frequency of the function generator until the blur envelope of the vibrating structure observed through the eyepieces or on the video monitor reaches a maximum. Some of the structures are designed with a vernier scale, which makes the amplitude estimation more accurate. The –3 dB bandwidth of the vibration is then estimated by tuning the driving frequency away from resonance, until the blur decreases to roughly 70% of the maximum. The quality factor Q is then deduced from the –3 dB bandwidth using the following formula:

$$Q = \frac{f_r}{f_2 - f_1} \quad (4.1)$$

where f_r is the resonant frequency and $(f_2 - f_1)$ is the –3 dB bandwidth. The results from Eq. (4.1) are combined with the recorded dc bias and drive voltage level to evaluate $\partial C/\partial x$ using Eqs. (2.11) and (2.16).

The experiment is repeated with the microscope light assembly replaced with a strobe light, which is triggered at a frequency 100 times less than that of the ac drive.

Besides providing a more stable image, the mode shape of the resonating structure can also be observed.

Finally, for testing under vacuum inside an SEM, the wafer is diced and bonded in a standard dual-in-line package (DIP), which is then mounted at a tilt angle inside the SEM chamber (Fig. 4.3). The SEM acceleration voltage is limited to about 1.6 kV to minimize charging from the scanning electron beams. Electrical signals are supplied to the chip with connectors through the chamber. The *HP 4192A LF Impedance Analyzer* is used as a signal generator for vacuum testing because of its capability to resolve

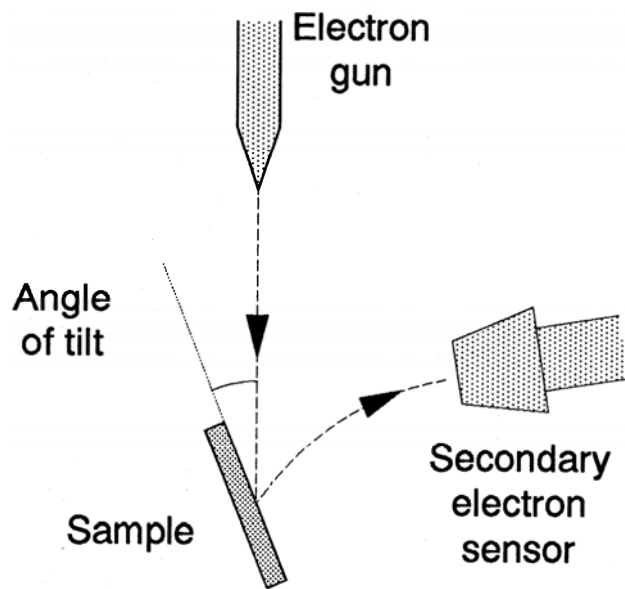


Figure 4.3 Test setup using an SEM.

frequencies at 10^{-3} Hz step and to generate signals at voltage amplitude down to 5 mV level with 1 mV steps.

Although cumbersome and time-consuming to set up, testing inside an SEM provides many advantages. First, in the absence of air damping, the measured resonant frequencies are very accurate because of the extremely narrow bandwidth. The dc bias and drive voltages required to sustain the high- Q resonance can also be lowered to 5 V and 50 mV amplitude respectively, and thus possible nonlinear effects due to large drive voltages are minimized. Furthermore, vertical motions are very difficult to observe using the optical techniques because the mechanical vibrations are in the line of vision. Also, since visual observation of resonance relies on maximizing the vibration amplitude, the low Q due to heavy squeeze-film damping in air hampers accurate measurements of the vertical resonant frequencies. Testing the sample mounted at a tilt angle inside the SEM avoids these problems associated with vertical-mode testing.

Testing by direct observation requires careful judgement on the part of the operator in deciding the size of the blur envelope of a vibrating structure, therefore, in order to minimize relative errors between data points, testing must be done in a consistent manner by the same operator without interruption during data collection.

4.1.2 Electrical Testing

To objectively verify the results obtained by observation, electrical testing techniques are developed. Both the linear resonator (Fig. 4.1) and the torsional structure (Fig. 4.2) are

originally designed to allow for electrical detection of the structural vibration. In the two-port arrangement, an *HP 4195 Spectrum Analyzer* would be connected to *pad 2* of either structures through a transimpedance amplifier to sense the current induced in the sense electrode by motion of the structure.

However, the weak motional current is difficult to detect without an on-chip buffer circuit [65]. Furthermore, the direct signal feedthrough from the drive port to the sense electrode through the large probe-to-probe parasitic capacitance is at least 10 times stronger than the desired motional signal.

To circumvent this problem, a modulation technique is used [70], in which a high-frequency ac signal is superimposed on top of the dc bias applied to the structure through the ground plane, as shown in Fig. 4.4. This signal serves as a carrier which is modulated by the time-varying sense capacitance. As a result, electrical feedthrough from fixed parasitic capacitors and the sense current due to the vibrating structure are separated in the frequency domain.

An alternative approach without the use of a carrier signal is to connect the structure to electrical ground and apply a pure ac signal to the drive port to create a frequency-doubling effect (Fig. 4.5). The frequency of the drive signal must now be at half of the resonant frequency of the structure in order to excite oscillation. With a drive

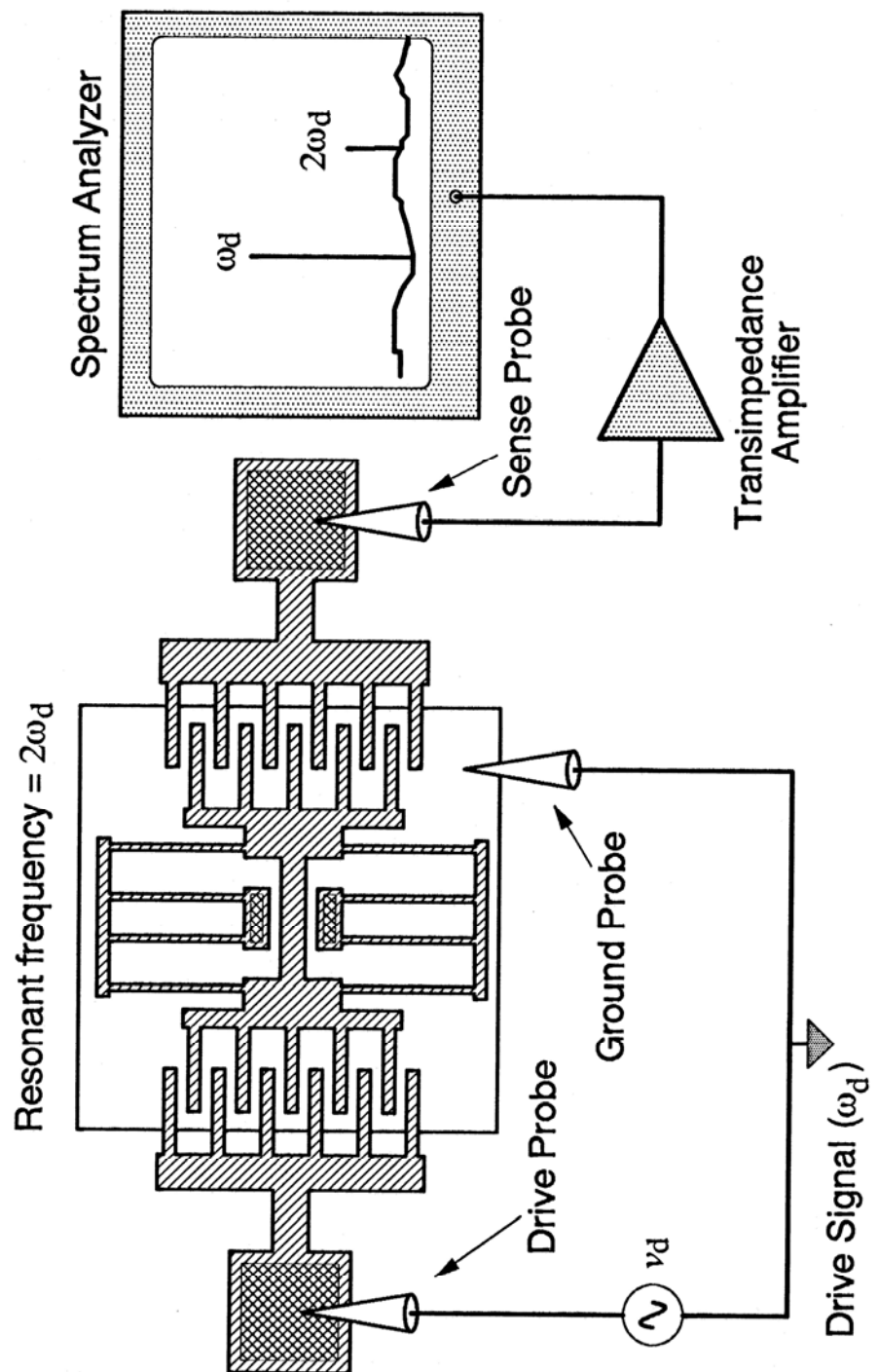


Figure 4.4 Electrical test setup with modulation technique.

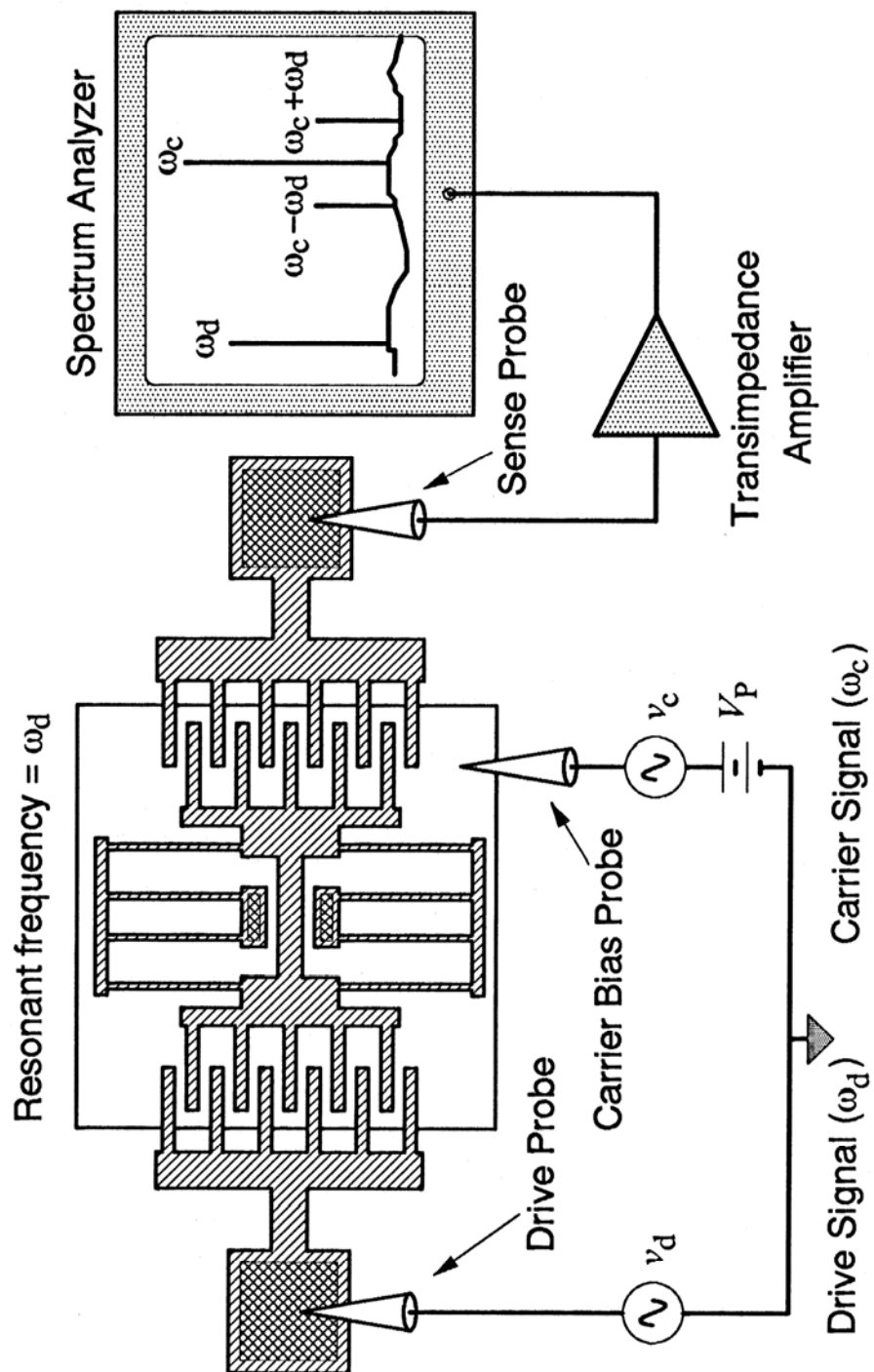


Figure 4.5 Electrical test setup using frequency-doubling effect.

voltage $v_D = v_d \sin(\omega t)$, the induced force on the comb finger is given by

$$\begin{aligned} F &= \frac{1}{2} \frac{\partial C}{\partial x} [v_d \sin(\omega t)]^2 \\ &= \frac{1}{4} \frac{\partial C}{\partial x} v_d^2 [1 - \cos(2\omega t)] \end{aligned} \quad (4.2)$$

Therefore, the separation of the motional current from the signal feedthrough is accomplished.

In this chapter, all the electrical measurements reported are done with the modulation technique because a stronger induced electrostatic force can be obtained by using a higher dc bias at the drive port (see section 2.1.3 of Chapter 2).

Since some of the earliest prototype structures do not have a standoff bump, they may be temporarily stuck to the substrate (see section 3.1 of Chapter 3). Therefore, in order to decide whether a structure is freed, as a standard practice, a dc voltage of 50 V is applied to the comb structure before each testing. If the structure does not deflect statically, it can be easily freed with a gentle probing.

We begin the analysis of the test results with a discussion on the microstructural parameters, which affect the performance of the finished structures. The measurement results are then organized and presented as two subtopics: lateral-mode and vertical-mode measurements.

4.2 MICROSTRUCTURAL PARAMETERS

There are two very important structural parameters that affect the performance of the fabricated microstructures: the deposited film thickness and the plasma-etching results. Although they do not affect the yield of the working structures, these two parameters play an important role in the uniformity and performance of the finished products.

4.2.1 Thickness of Deposited Polysilicon Film

Due to the characteristics of the LPCVD furnace, there is a rather large wafer-to-wafer variation of deposited film thickness, especially the structural polysilicon film. The thickness profile from a batch of wafers processed from the second run is obtained using an *Alpha-Step* surface profiler, and is listed in Table 4.I, with their relative position inside the furnace tube illustrated in Fig. 4.6.

Table 4.I Polysilicon film thickness profile

Position	1	2	3	4	5	6	7	8	9
Thickness [μm]	2.21	2.11	2.04	2.00	2.07	1.96	1.89	1.84	1.80

Table 4.I shows that films that are deposited on wafers closest to the gas sources tend to be thicker, with a maximum thickness variation of $\pm 10\%$ from average. Although the lateral resonant frequencies are not dependent on the thickness of the structures, $\partial C/\partial x$, and thus the lateral drive capacity, as well as the vertical mode of motions, are strong functions of the structural-film thickness.

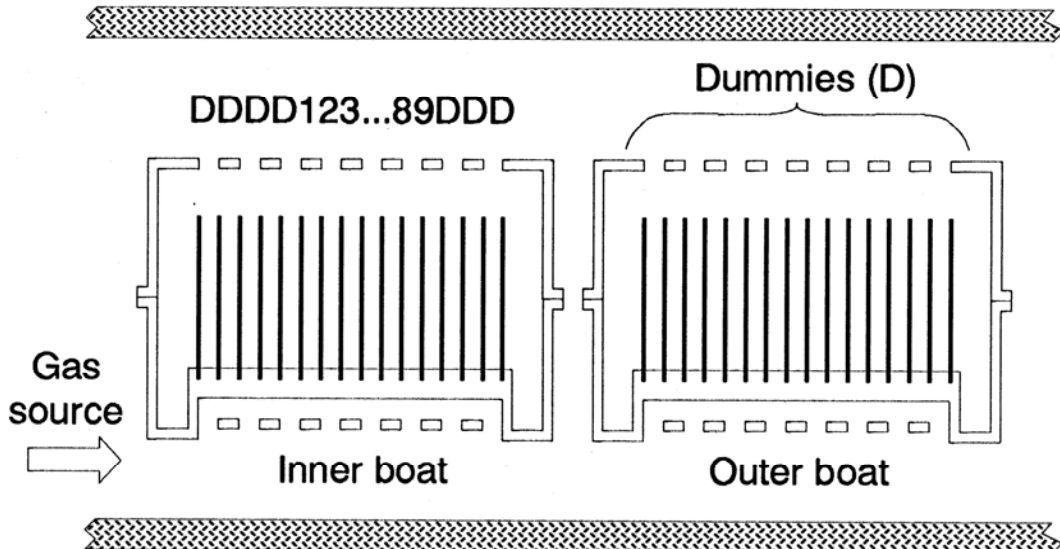


Figure 4.6 Position of the wafers inside the LPCVD polysilicon tube.

In order to improve the consistency of wafer-to-wafer film thickness, deposition can be done in two equal-length steps, with the wafer positions reversed between the two depositions. Table 4.II lists the results of an experimental run using the two-step-deposition approach, which show very satisfactory results.

Table 4.II Polysilicon film thickness profile from a two-step deposition experimental run

Position	1	2	3	4	5	6	7	8	9
Thickness [μm]	2.71	2.70	2.70	2.68	2.70	2.66	2.68	2.70	2.70

Another alternative is to modify the furnace tube such that reactive gases are distributed with an injector throughout the length of the furnace.

4.2.2 Plasma-Etching Results

The sidewall profiles of the structural-polysilicon film after reactive-ion etched in $\text{CCl}_4\text{-O}_2$ plasma depend on, among others factors, the erosion rate of the photoresist mask and the vertical kinetic energy of the reactive ions [71]. If the photoresist mask is being continuously eroded away during etching, the sidewall will be angled even when etching is anisotropic. To slow down mask erosion during etch, selectivity of etching polysilicon with respect to the photoresist must be increased. This is usually accomplished by hardening the photoresist mask or by etching at a low ion energy level. However, low-energy etching results in less anisotropy, which leads to excessive undercutting of the polysilicon material. Therefore, the reactive energy must be characterized carefully.

Figure 4.7 is an SEM of a microstructure etched with excessive energy, causing the top edges to be rounded. Figure 4.8 is an SEM of another structure showing excessive undercutting, a result of low-energy etch. An optimally etched structure is shown in Fig. 4.9, which has slightly sloped but straight sidewalls. The optimized recipe is detailed in Appendix A.

Etch uniformity across a wafer is mostly a function of the reactor geometry and therefore hard to control. The center of a wafer is usually etched faster because it is in the center of the plasma discharge and is nearest to the gas sources. Etch nonuniformity

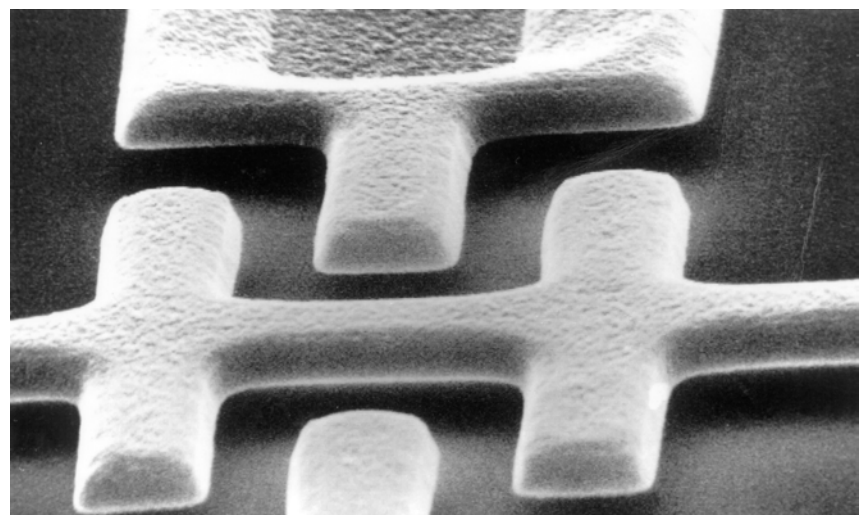


Figure 4.7 SEM of a microstructure etched with excessive energy.

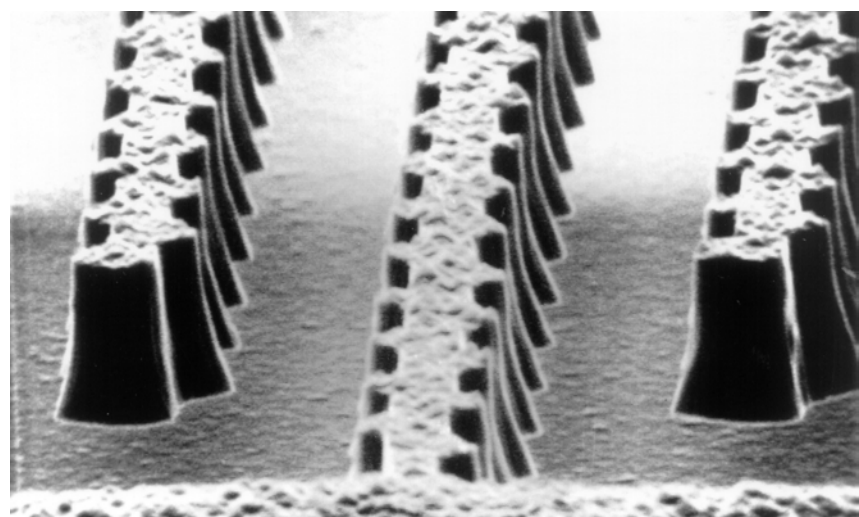


Figure 4.8 SEM of a microstructure etched with insufficient energy.

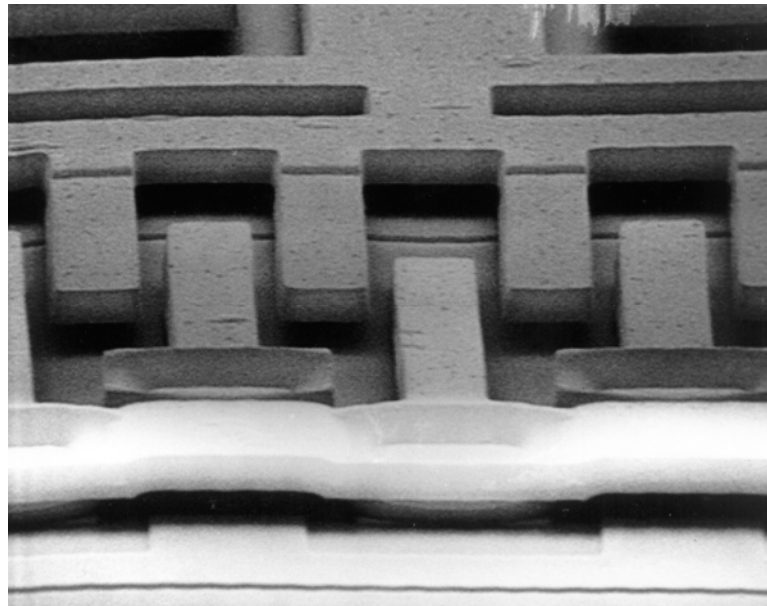


Figure 4.9 SEM of a microstructure etched with optimum energy.

is evidenced by the fact that the resonant frequencies of the same prototype resonators at the center of the wafer are lower than those near the edge. This is due to narrowed supporting beams as a result of excessive undercutting near the center of the wafer. The difference can be as much as 20% in the worst case. By decreasing the etch power and increasing the amount of overetch, uniformity could be slightly improved, at the expense of losing anisotropicity. The use of non-erodible mask may also improve the uniformity.

4.3 LATERAL-MODE MEASUREMENTS

Two series of lateral-resonator prototypes with different electrostatic comb designs (type A and type B) are used to verify the stress-relieving property of the folded-beam support and to evaluate the Young's modulus of the polysilicon film used. The features of these two types are tabulated in Table 4.III. Each series consists of resonant structures with beam length from 80 to 200 μm . The different comb-structure dimensions are illustrated in Fig. 4.10.

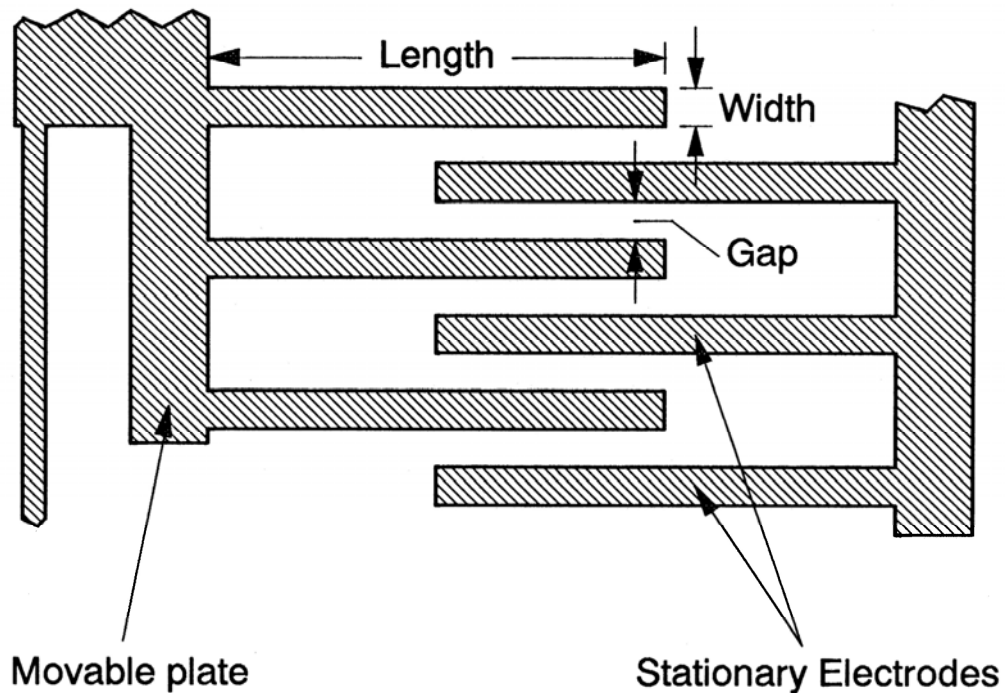


Figure 4.10 Comb-structure dimensions.

Table 4.III Comb drive features of types A and B,
with comb width = 4 μm , length = 40 μm , overlap = 20 μm

Type	Number of fingers	Finger gap [μm]	Plate mass, M_p [$\times 10^{-12} \text{ kg}$]	Truss mass, M_t [$\times 10^{-12} \text{ kg}$]
A	9	3	35.88	4.23
B	11	2	39.93	4.23

The spring constant, k_x , of each structure is calculated with Eqs. (2.45) and (2.49), with the given beam length and the following beam cross-section dimensions obtained with the *Vickers* line-width measurement system on the tested die:

top width, $a = 1.95 \mu\text{m}$ and bottom width, $b = 2.05 \mu\text{m}$.

The polysilicon film thickness is measured with the *Alpha-Step* surface profiler, and is found to be 2.05 μm . The resonant frequencies can then be calculated from Eq. (2.71) (see section 2.3.1.3 of Chapter 2), using a value of $2.3 \times 10^3 \text{ kg}\cdot\text{m}^{-3}$ for ρ , the density of polysilicon.

In addition, two torsional structures, one supported with two, two-turn Archimedean spirals and the other with four serpentine springs which are included in the same (first) process run. These are tested to verify the differential-drive technique as well as the rotational stability of the angular vibrations.

The spring constant for the spiral is calculated from Eq. (2.75), while that for the serpent is obtained with finite-element simulations. Eqs. (2.76) and (2.77) are then used to evaluate the torsional resonant frequencies (section 2.3.2.3 of Chapter 2).

Finally, the performance of the electrostatic-comb drive as a function of its geometry is evaluated with a third series of lateral resonators (type C) with the length of the folded-beam supports fixed at 200 μm . This set of prototypes was fabricated from the second process run with a polysilicon film measured to be 2.1 μm thick, with the following beam cross-section dimensions:

$$a = 2.0 \mu\text{m} \text{ and } b = 2.15 \mu\text{m}$$

Table 4.IV lists the different designed dimensions of type C resonators.

Table 4.IV Type C comb dimensions

Type	Number of fingers	Finger length [μm]	Finger width [μm]	Comb gap [μm]
C1	12	20	2	2
C2	12	30	2	2
C3	12	40	2	2
C4	12	50	2	2
C5	12	40	3	2
C6	12	40	4	2
C7	12	40	5	2
C8	12	40	2	3
C9	12	40	2	4
C10	12	40	2	5

4.3.1 Resonant Frequencies and Young's Modulus

The measured resonant frequencies for types A and B linear resonators are listed in Table 4.V and those for the torsional structures are listed in Table 4.VI. The predicted resonant frequencies in Tables 4.V and 4.VI are found from Eqs. (2.71) and (2.76) of Chapter 2 with the Young's modulus E adjusted to give the best fit to the experimental data. From this first process run, E is found to be 140 GPa.

Table 4.V Predicted and measured resonant frequencies of prototypes A and B

Beam Length [μm]	Type A		Type B	
	Predicted [kHz]	Measured [kHz]	Predicted [kHz]	Measured [kHz]
80	75.5	75.0 ± 0.05	71.8	72.3 ± 0.05
100	53.7	54.3 ± 0.05	51.1	50.8 ± 0.05
120	40.6	41.1 ± 0.1	38.7	39.4 ± 0.1
140	32.0	32.0 ± 0.2	30.5	30.0 ± 0.2
160	26.0	25.9 ± 0.2	24.8	25.0 ± 0.2
180	21.7	21.5 ± 0.3	20.7	20.3 ± 0.3
200	18.4	18.2 ± 0.3	17.6	17.5 ± 0.3

Table 4.VI Predicted and measured resonant frequencies of the torsional structures

Supporting Beam Type	Predicted [kHz]	Measured [kHz]
Spiral	10.5	9.7 ± 0.3
Serpent	60.7	59.4 ± 0.2

In order to verify the visual-observation results, three different test approaches are used to obtain the resonant frequencies for the C-series prototypes: visual testing with continuous-optical illumination, observation with strobe light, and electrical testing with modulation technique. The results are listed in Table 4.VII., which shows that the results obtained from the three testing methods independently agree with the calculated results.

Table 4.VII Predicted and measured resonant frequencies
of the C-series prototypes

Type	Calculated	Measured		
		Optical ± 0.05	Strobe ± 0.05	Electrical ± 0.05
C1	23.4	22.9	23.1	22.8
C2	22.6	22.3	22.4	22.9
C3	21.9	22.1	22.0	22.0
C4	21.3	21.5	21.6	21.6
C5	20.4	20.9	20.5	20.3
C6	19.1	19.2	19.3	19.3
C7	18.1	18.8	18.4	18.0
C8	21.3	21.1	21.2	21.4
C9	20.8	20.5	20.7	21.0
C10	20.2	20.0	19.9	19.8

The best-fit value for Young's modulus is $E = 140$ GPa for both linear and torsional resonators from the first process run, while measurements of the C-series prototypes from the second and third runs indicate a slightly higher value of 150 GPa. The difference may be attributable to variations in processing conditions of the fabrication equipments over time, especially the LPCVD furnace tube used to deposit the structural-polysilicon layer. Nevertheless, both of these values are typical of the doped polysilicon films processed at Berkeley [6, 8].

From Tables 4.V and 4.VI, the calculated and measured resonant frequencies are in close agreement for all the lateral structures. It should be noted that residual strain in the released structures is neglected in the calculation. The excellent fit with the measured frequencies over a range of truss dimensions and for the spiral and serpentine springs suggests that the residual strain is effectively relieved in these structures. Otherwise, it would be expected that a shift in frequency from the simple unstrained theory would be observed, with a greater shift for the shorter beams [34]. Furthermore, there may be a slight shift in resonant frequencies associated with large-amplitude oscillations [33], although such a shift is not observed with the visual technique employed in the present experiment.

4.3.2 Lateral-Mode Quality Factors

Initial visual measurements of the quality factor Q are plotted in Fig. 4.11 for prototypes A and B, together with the curves calculated from Eq. (2.74) in section 2.3.1.4. The visual measurement of Q is especially difficult for structures with small vibration

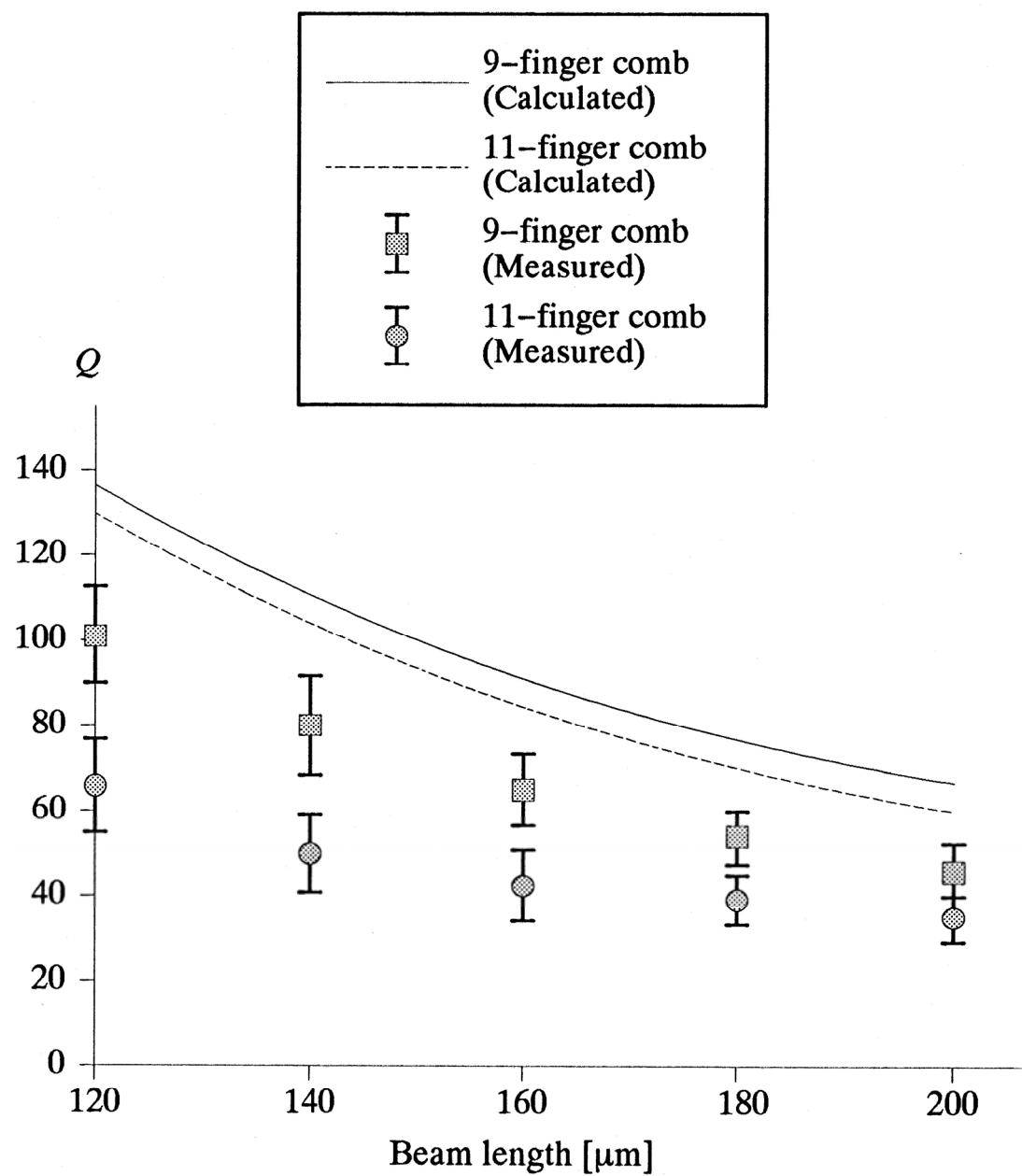


Figure 4.11 Measured and calculated Q vs. beam length.

amplitudes, which is reflected in the larger error bars for these points. The calculated quality factors are consistently higher than the measured values, indicating that the assumption of including only Couette flow underneath the plate in evaluating Q is an oversimplification for these structures. However, the calculated values of Q are within a factor of two of the actual measurements and may be useful for design purposes. The highest measured Q is about 130 for a structure with 80 μm -long folded-beam suspension.

In order to study the contribution of the comb-finger damping to the quality factor, the C-series prototypes are tested for Q with all three testing methods. The gap between comb fingers is found to be the most important design parameter for the quality factor. Figure 4.12 is a plot of the optical and electrical measurements of the quality factor Q for the set of test structures with different finger gaps (prototypes C3, C8–C10). An important observation from Fig. 4.12 is that Q is low for structures with either small finger gaps or widely separated fingers. Tightly spaced fingers lead to higher air-drag damping, while widely spaced ones must be attached to a wider structure for support, and hence also resulting in more air damping.

In order to evaluate the quality factor of the resonator in vacuum, one of the type A linear resonators with 140 μm -long folded-beam support is packaged and tested inside an SEM at a pressure of 10^{-7} torr. Figure 4.13 is an SEM of the vibrating structure driven by a 100 mV-amplitude ac voltage on top of a 5 V dc bias. The vibration amplitude is estimated to be 10 μm peak-to-peak. In the SEM, this structure resonates at $f_r = 31,636.91 \pm 0.02$ Hz. The quality factor is evaluated with both time- and

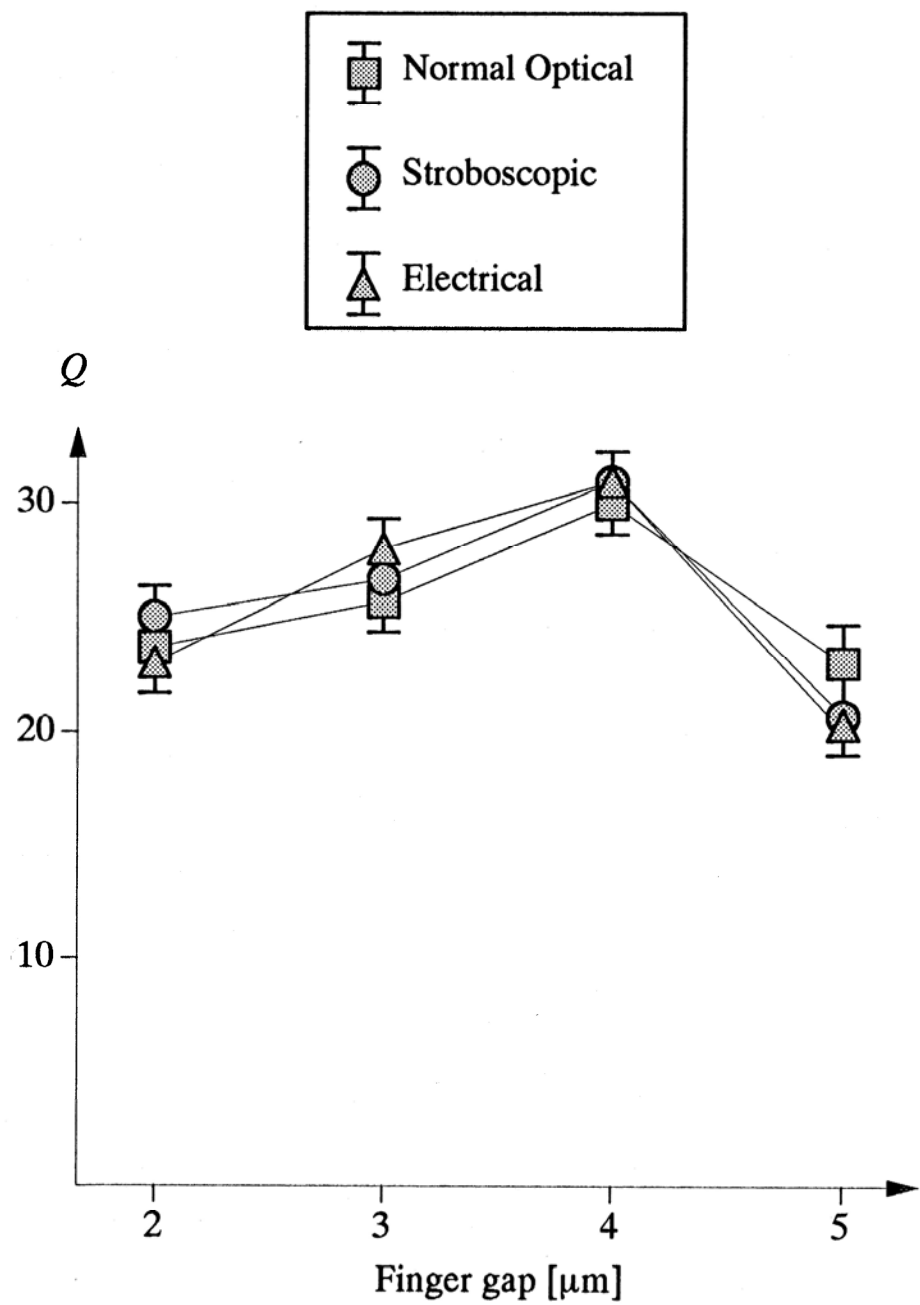


Figure 4.12 Q vs. finger gap.

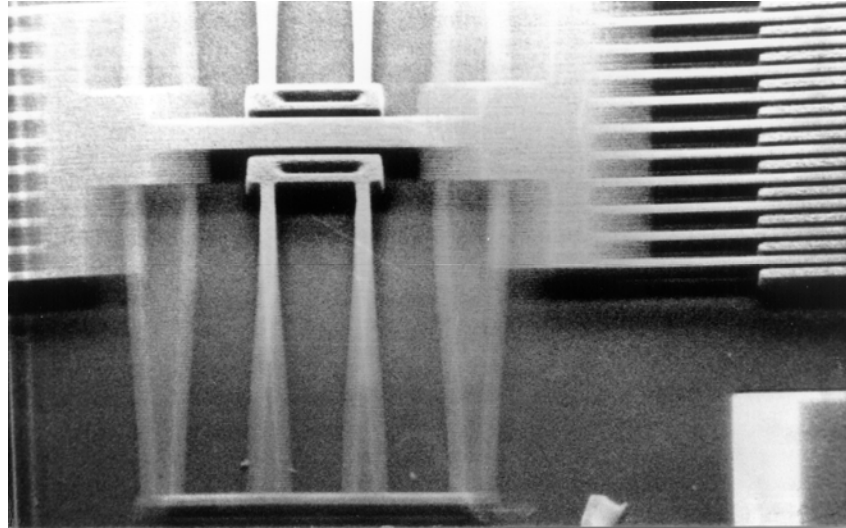


Figure 4.13 SEM of a vibrating structure under high vacuum (10^{-7} torr).

frequency-domain methods:

$$Q \approx 1.43Tf_r \quad \text{and} \quad Q = \frac{f_r}{f_2 - f_1} \quad (4.3)$$

where T is the time for the oscillation amplitude to drop from 90% to 10% of its full amplitude after stopping the drive, and $(f_2 - f_1)$ is the -3 dB bandwidth (Fig. 4.14). The values of Q are $49,000 \pm 2,000$ and $50,000 \pm 5,000$ from the time- and frequency-domain methods, respectively.

The vibration of the structure is lateral to the substrate, without any indication of

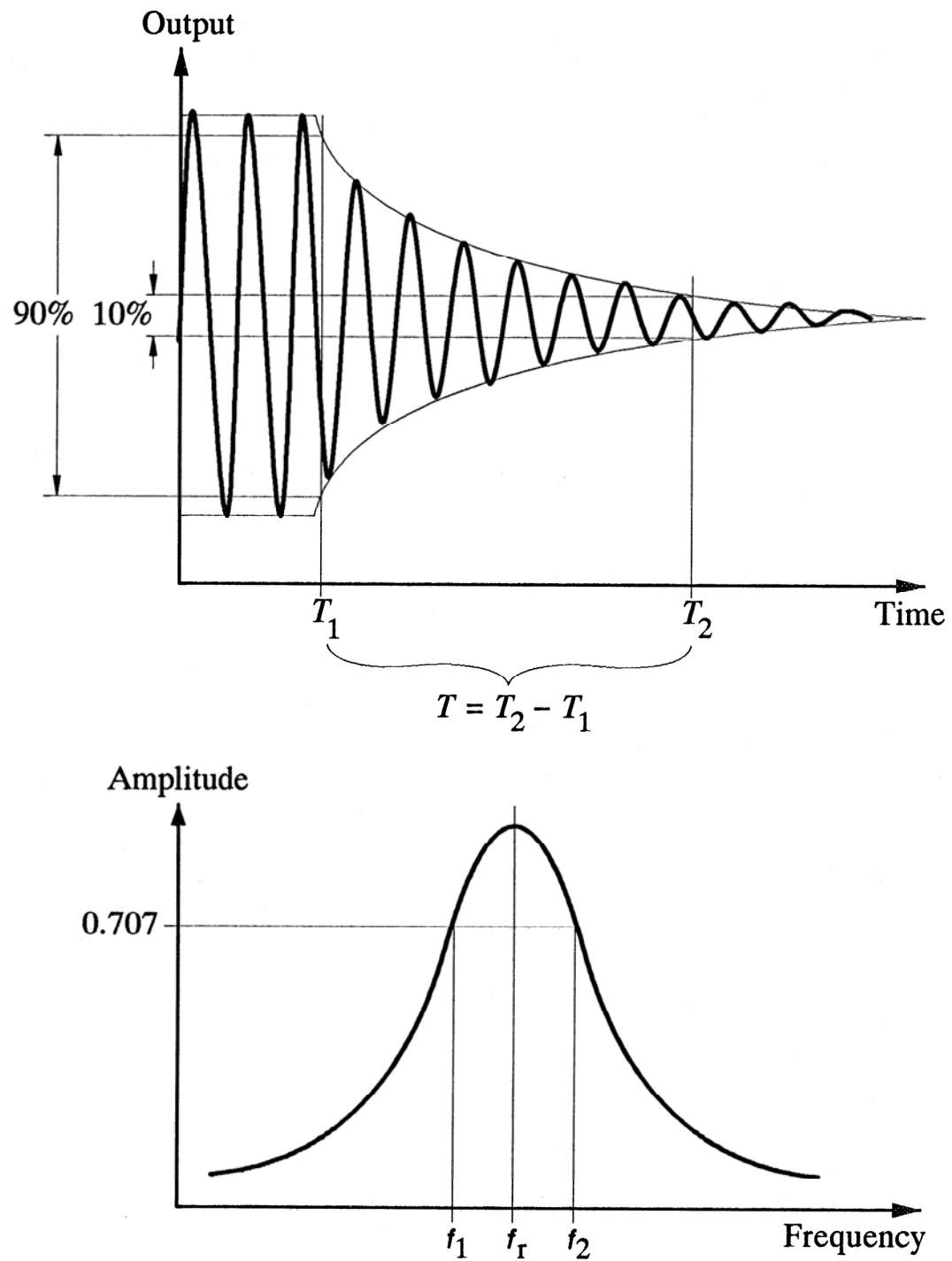


Figure 4.14 Time- and frequency-domain methods for Q evaluation.

torsional or vertical motion. It is important to note that the mechanical resonant frequency of the vertical mode is very close to that of the designed lateral mode due to the almost square cross section of the suspensions. A purely lateral vibration is excited as a result of the shift in the vertical resonant frequency due to the unbalanced comb drive (see section 2.2 of Chapter 2).

4.3.3 Capacitance Gradient, $\partial C/\partial x$

With the value of Q measured and the spring constant k_x established, we need only to measure the electromechanical transfer function at resonance to evaluate $\partial C/\partial x$ with Eq. (2.11) of Chapter 2. Alternatively, we can measure the static displacement of the structure under a dc bias, and use the solution of Eq. (2.5) to calculate $\partial C/\partial x$, without having to know Q *a priori*.

Figure 4.15 is a comparison of the experimental results for prototypes A and B with the calculated values from Eq. (2.11), for which $\partial C/\partial x$ for the two types of comb drives is a fitting parameter. The type A drive is found to have $\partial C/\partial x = 58 \text{ aF}\cdot\mu\text{m}^{-1}$ and type B has $\partial C/\partial x = 150 \text{ aF}\cdot\mu\text{m}^{-1}$.

The C-series prototypes are used to study the effects of different comb designs on $\partial C/\partial x$. It is found that the comb gap has the most effect on the values of $\partial C/\partial x$. Figure 4.16 is a plot of $\partial C/\partial x$ as a function of the finger gap, which shows the expected sharp increase with reduced gaps. Both Figs. 4.12 and 4.16 indicate that the three different measurement techniques are in good agreement within experimental errors. These two

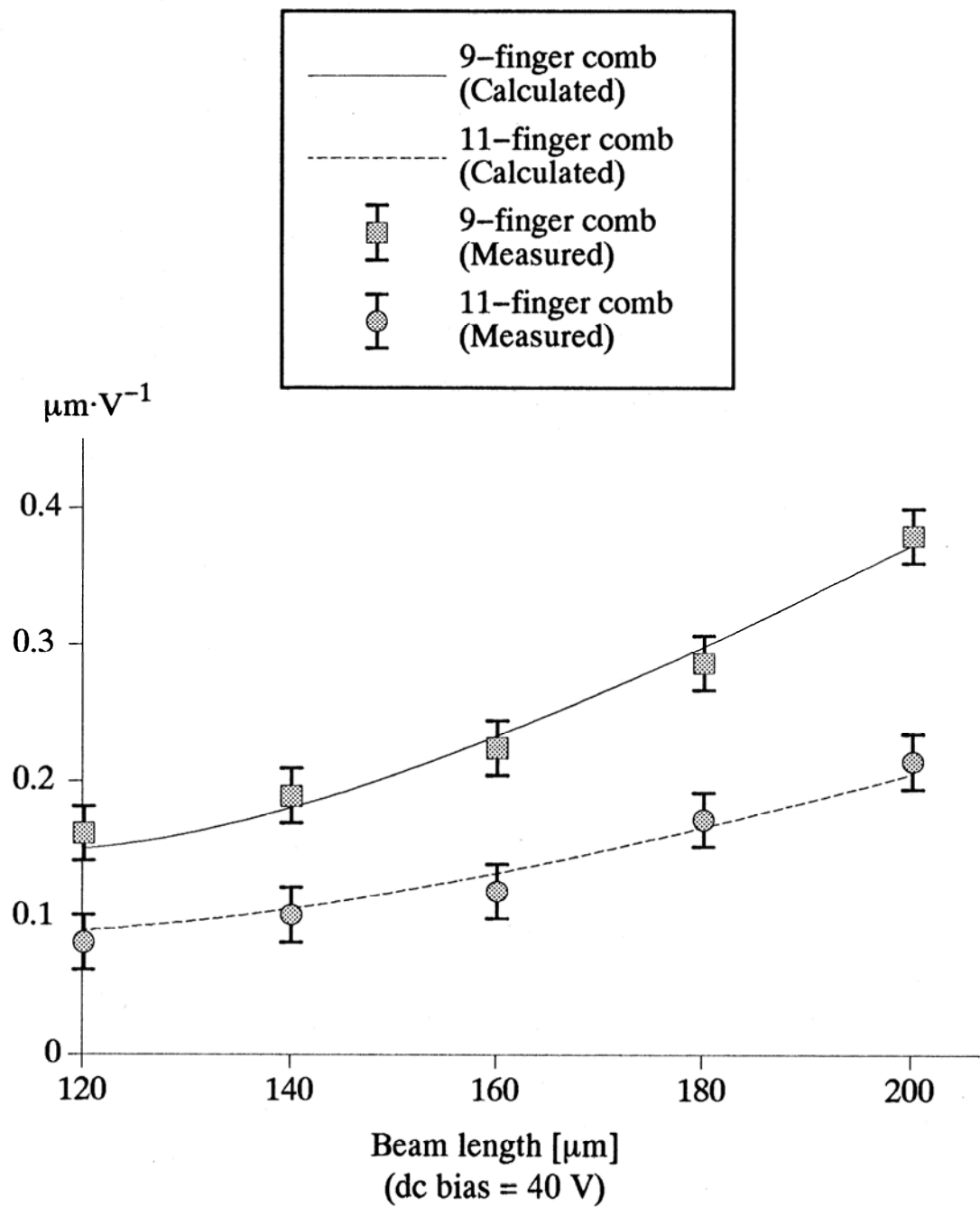


Figure 4.15 Measured and calculated values of the transfer functions.

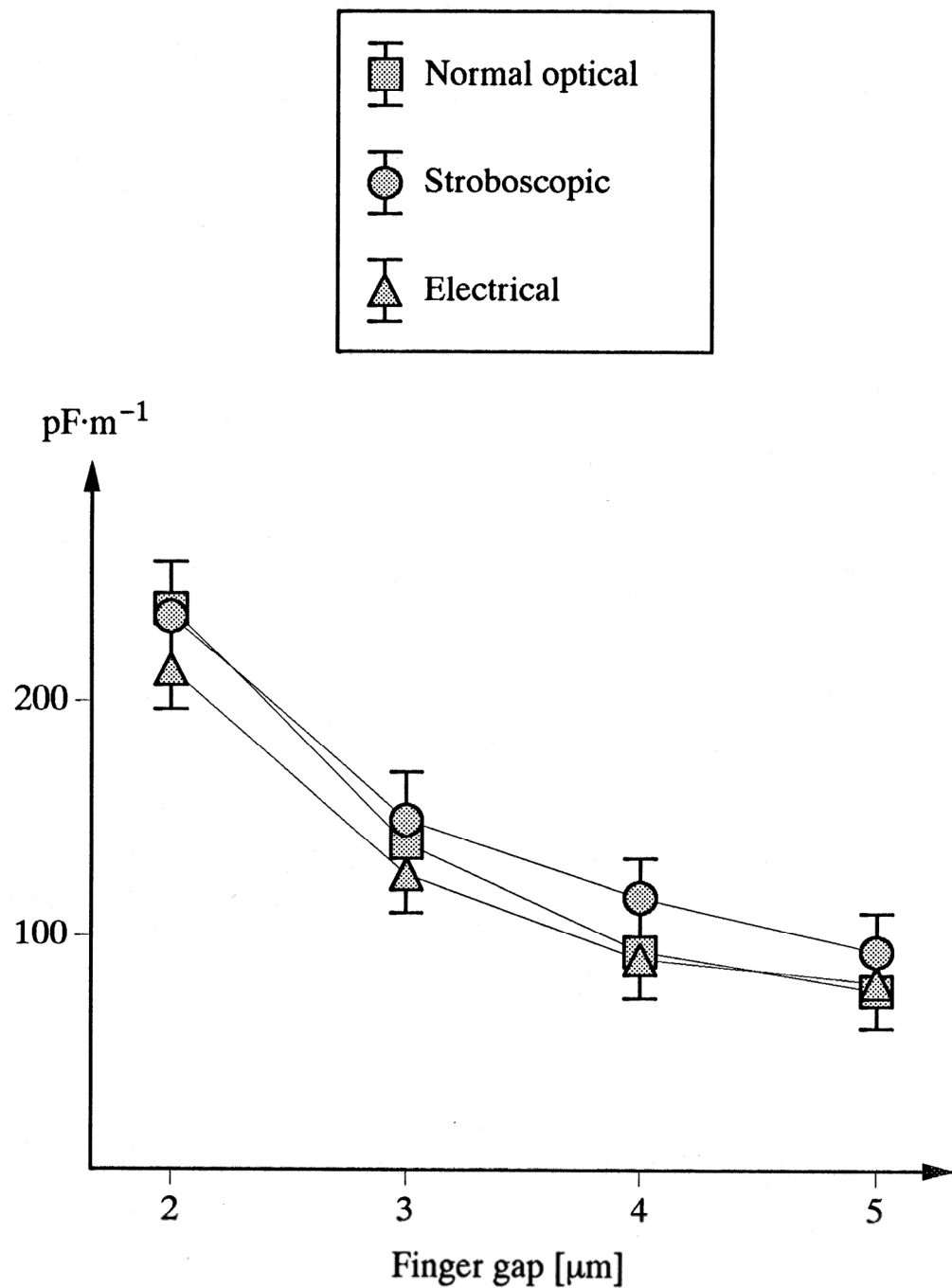


Figure 4.16 $\partial C / \partial x$ vs. finger gap.

plots also provide the empirical basis for designing electrostatic-comb drive.

4.4 VERTICAL-MODE MEASUREMENTS

Prototypes from the third process run (V-series) are used to study vertical-mode excitation. They are designed with 400 μm -long folded-beam supports to provide compliance in both the out-of-plane (z) and the lateral (x) directions. The polysilicon-film thickness of the device under test is measured to be 1.94 μm with *Alpha-Step*. The cross-sectional dimensions are $a = 2.2 \mu\text{m}$ and $b = 2.8 \mu\text{m}$ from *Vickers* linewidth measurements. These dimensions are somewhat wider than the designed 2 μm due to a combination of slight underexposure and underdevelopment on the photoresist. Note also that the sidewalls from this process run are more angled than that from the first and second run, due to the change of the photolithography system. The new photoresist (*Olin-Hunt 6512*, I-line resolution) that is used in this run erodes slightly faster than the original *KTI 820* G-line resist under the same etching conditions and parameters in CCl_4 - O_2 plasma.

The comb drives of all V-series prototypes have lateral vernier scales to measure lateral deflections. The structures are first resonated laterally to evaluate the Young's Modulus from the measured resonant frequencies, using Eqs. (2.45), (2.49) and (2.71) from sections 2.3.1.1 and 2.3.1.3 of Chapter 2. The same value for the Young's modulus is then used for the vertical-motion calculations based on the fact that polysilicon is materially isotropic.

The value for the Young's modulus is found to be 150 GPa, similar to the value found from the second process run but slightly higher than the 140 GPa value from the

first run. The lateral spring constant is then calculated to be

$$k_x = \frac{h}{2L^3} (a+b)(a^2 + b^2) E = 140 \text{ nN}\cdot\mu\text{m}^{-1} \quad (4.4)$$

Similarly, the vertical spring constant is evaluated as

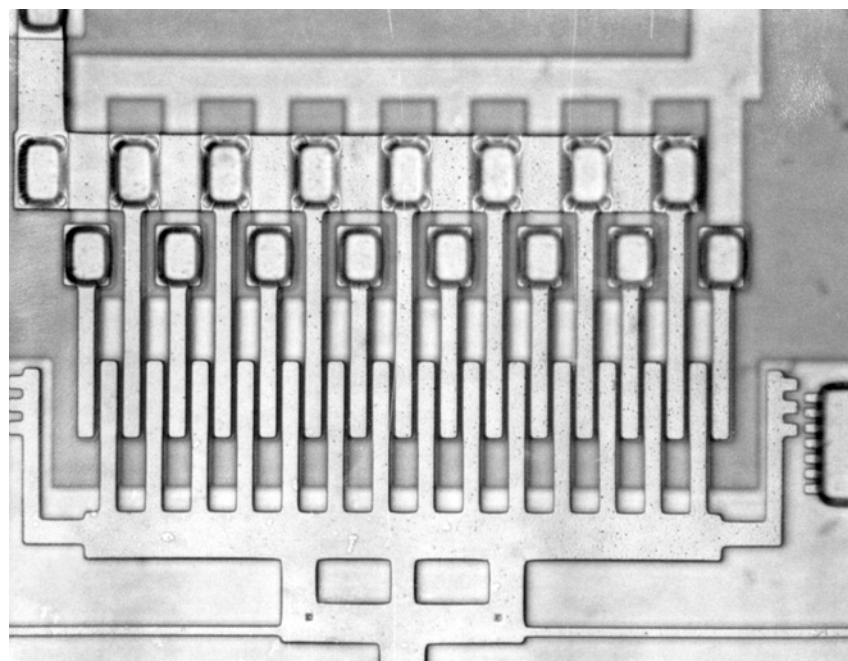
$$k_z = \frac{2h^3(a^2 + 4ab + b^2)}{3L^3(a+b)} E = 86 \text{ nN}\cdot\mu\text{m}^{-1} \quad (4.5)$$

Vertical motions are tested entirely in a low-voltage (1.6 kV) SEM to minimize charging effects due to the scanning-electron beams. All structures are wired together to make possible the measurement of a number of structures in a single SEM session. The angle of tilt of the sample inside the SEM chamber and the magnification are fixed for comparison between different structures. Vertical displacements are evaluated by accurately measuring the SEM images with a set of standard linewidths.

The comb dimensions for all the V-series prototypes are nominally 40 μm long, 4 μm wide, with a gap of 2 μm . However, underetch is evidenced by the cross-sectional dimension of the supporting beam, and thus 0.1 μm and 0.3 μm are added to all top and bottom perimeters, respectively. The structures are offset from the substrate by 2.0 μm . The different interdigititation designs in the V series are listed in Table 4.VIII. Figures 4.17–4.19 are the optical micrographs of some of the comb designs.

Table 4.VIII Different comb designs for levitation control

Type	Ground plane design	Drive finger alternation method
V1	striped conductor	every drive finger
V2	conventional blanket	every drive finger
V3	conventional blanket	every other drive finger
V4	conventional blanket	every third drive finger
V5	conventional blanket	every fourth drive finger
V6	conventional blanket	every sixth drive finger

**Figure 4.17** Optical micrograph of prototype V1 with 15 drive fingers.

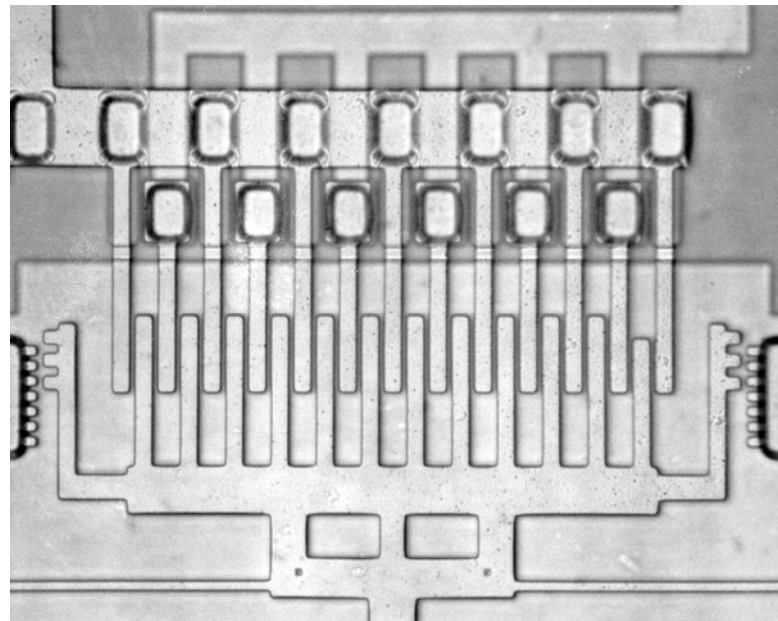


Figure 4.18 Optical micrograph of prototype V2 with 13 drive fingers.

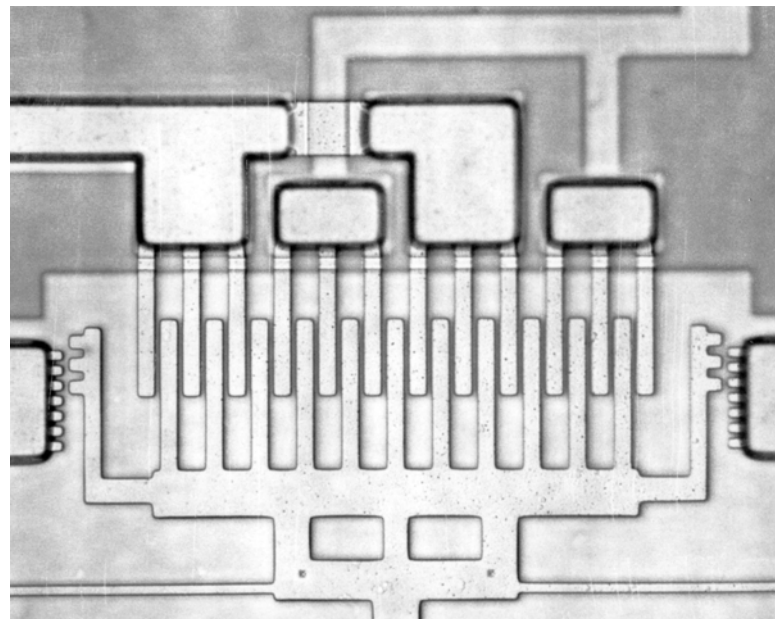


Figure 4.19 Optical micrograph of prototype V4 with 12 drive fingers.

The following presents the comparison of the effectiveness of different designs after an evaluation of the levitation phenomenon.

4.4.1 DC Levitation Results

Levitation is first measured by applying a voltage of 0 to 25 V to all drive fingers on one of the V1 prototypes with 18 movable comb fingers and 19 fixed drive fingers, the result of which is plotted in Fig. 4.20. Figure 4.21 is an SEM of a V2 prototype levitated under a 10 V dc bias. The vertical displacement increases with applied voltage and reaches an equilibrium near 20 V where the attractive forces between the displaced interdigitated fingers offset the repulsive electrostatic forces between the ground plane and movable fingers (see section 2.2 of Chapter 2). The initial negative deflection for a grounded comb, shown in Fig. 4.20, cannot be attributed to gravity. Charging effects in the exposed underlying dielectric films between the interdigitated striped ground plane are a likely source of this offset displacement. To account for the initial negative deflection, we hypothesize a fixed-charge force, F_c , which attracts the structure to the substrate:

$$F_c = \frac{\beta}{(z+d)^2} \quad (4.6)$$

where d is the nominal offset of the structure from the substrate and β is the constant of proportionality. Figure 4.22 illustrates the addition of F_c to the system. The term F_c is now added to Eq. (2.23) of section 2.2.3 of Chapter 2 as

$$F_{\text{net}} = F_z - F_k - F_c = 0 \quad (4.7)$$

Equations (2.21) and (2.24) of section 2.2.3 are combined with Eq. (4.6) to substitute the

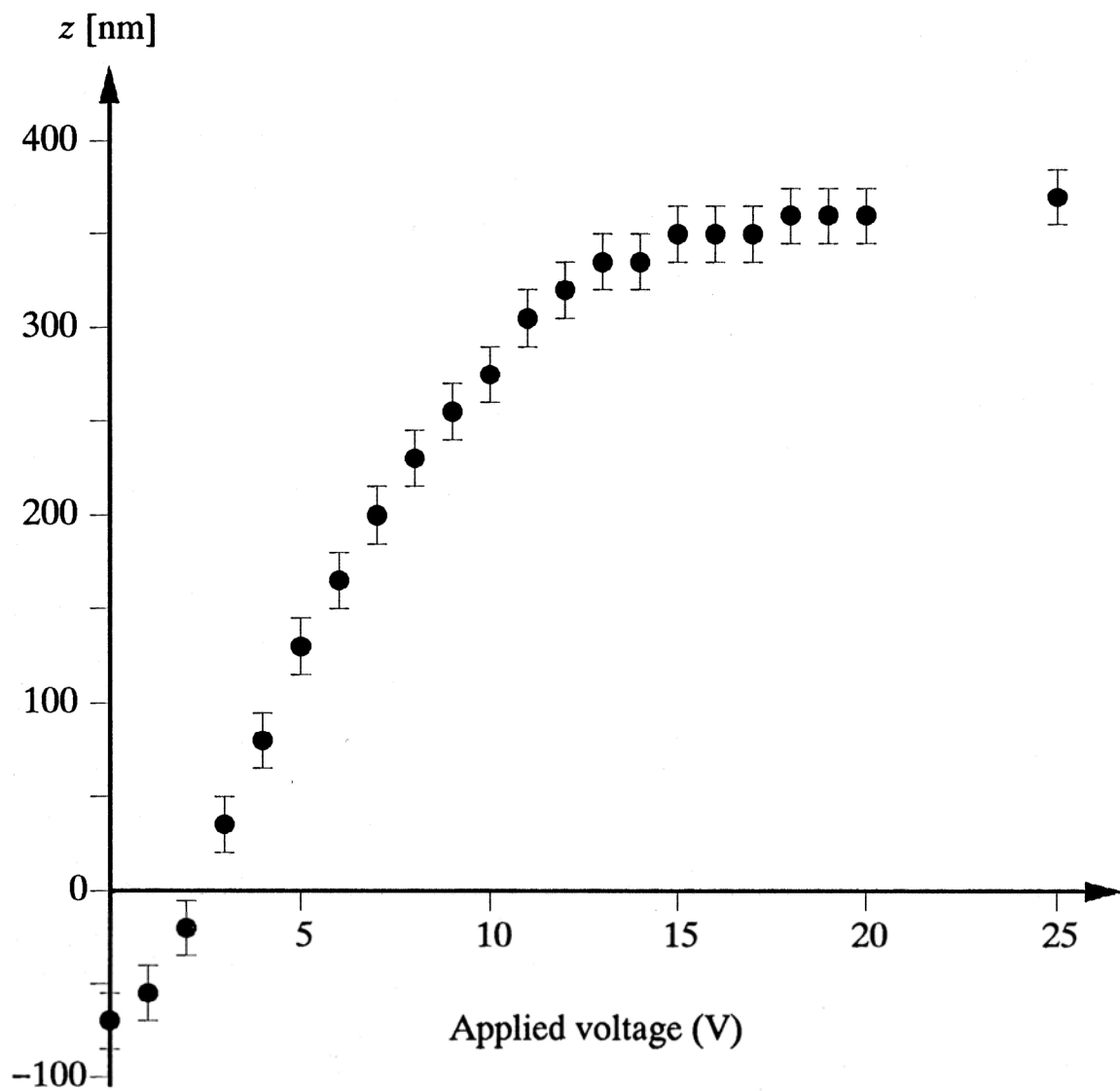


Figure 4.20 Levitation as a result of a common voltage applied to all electrodes.

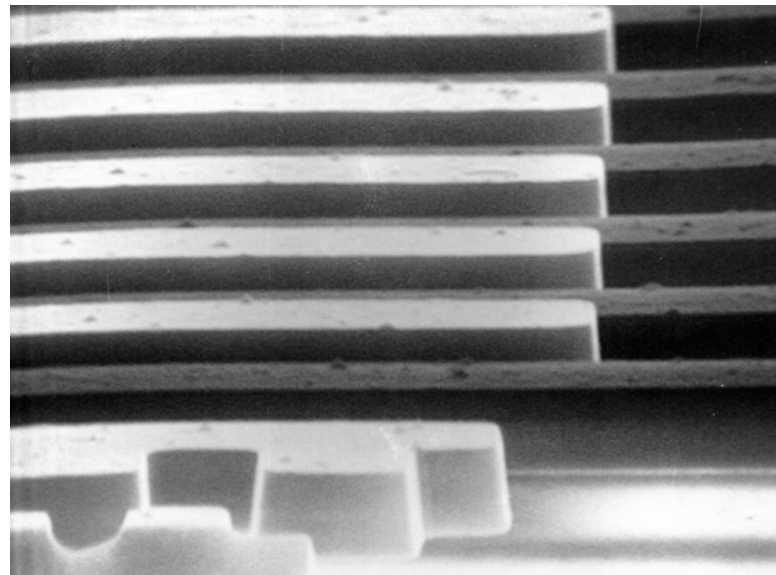


Figure 4.21 SEM of a V2 prototype comb levitated under 10 V dc bias. Note that the drive fingers, because of the positive bias, appear darkened in the SEM.

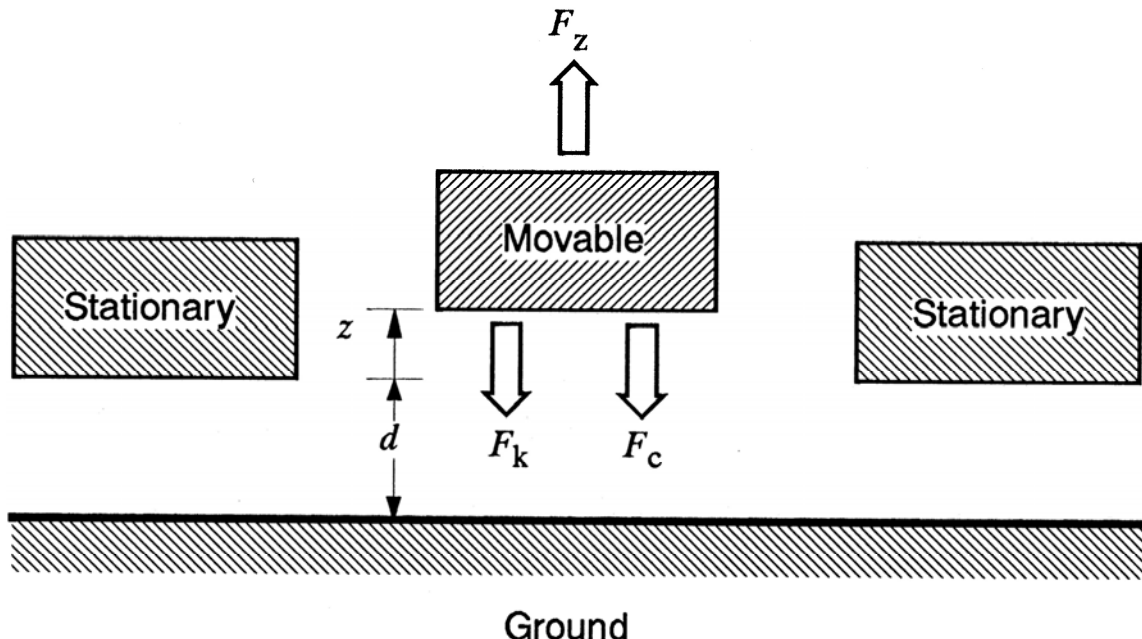


Figure 4.22 The three forces acting on the movable comb finger.

terms in Eq. (4.7), yielding an implicit function as follows

$$V_P = \left(\frac{k_z z + \beta / (z + d)^2}{\gamma_z (z_0 - z) / z_0} \right)^{\frac{1}{2}} \quad (4.8)$$

Figure 4.23 is the result of fitting the curve to the data in Fig. 4.20 by adjusting z_0 , γ_z and β . The best-fitted values are $z_0 = 400$ nm, $\gamma_z = 47$ pN·V⁻² per drive finger, and $\beta = 23.6$ nN·μm². The equilibrium levitation (z_0) of 0.4 μm is much less than the observed 2 μm levitation in some structures with soft spring supports and a blanket ground plane.

The effectiveness of levitation control by alternating the potentials on every drive finger of prototype V1 is evaluated next. Figure 4.24 is a plot of the measured vertical displacement resulting from holding one set of an alternating drive fingers at +15 V and varying the other set of electrodes from -15 V to +15 V. This structure is the same as that tested in Fig. 4.20. As expected, negative voltages in the range of -10 V to -15 V suppress the lifting behavior. As the disparity between the magnitudes of the voltages increases, more lifting occurs, with the limiting case of +15 V applied to all drive fingers yielding the same vertical displacement as found in Fig. 4.20. Figure 4.25 is the SEM of prototype V1 under a ±10 V balanced biasing on the alternating drive fingers, indicating almost no levitation. Note that the voltage-contrast effect inside the SEM causes the drive fingers at a higher potential to appear darkened.

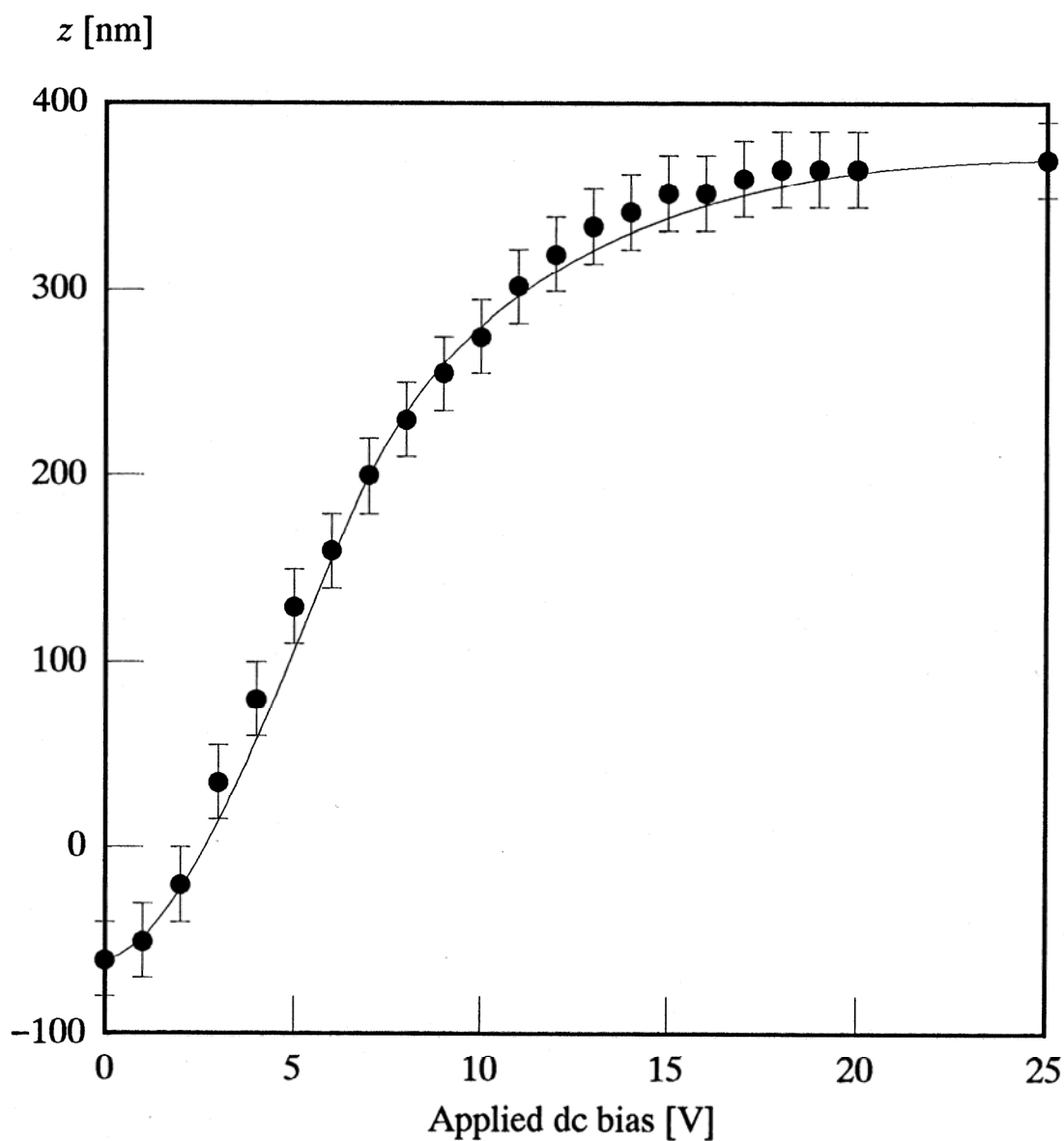


Figure 4.23 Measured and calculated levitation for prototype V1.

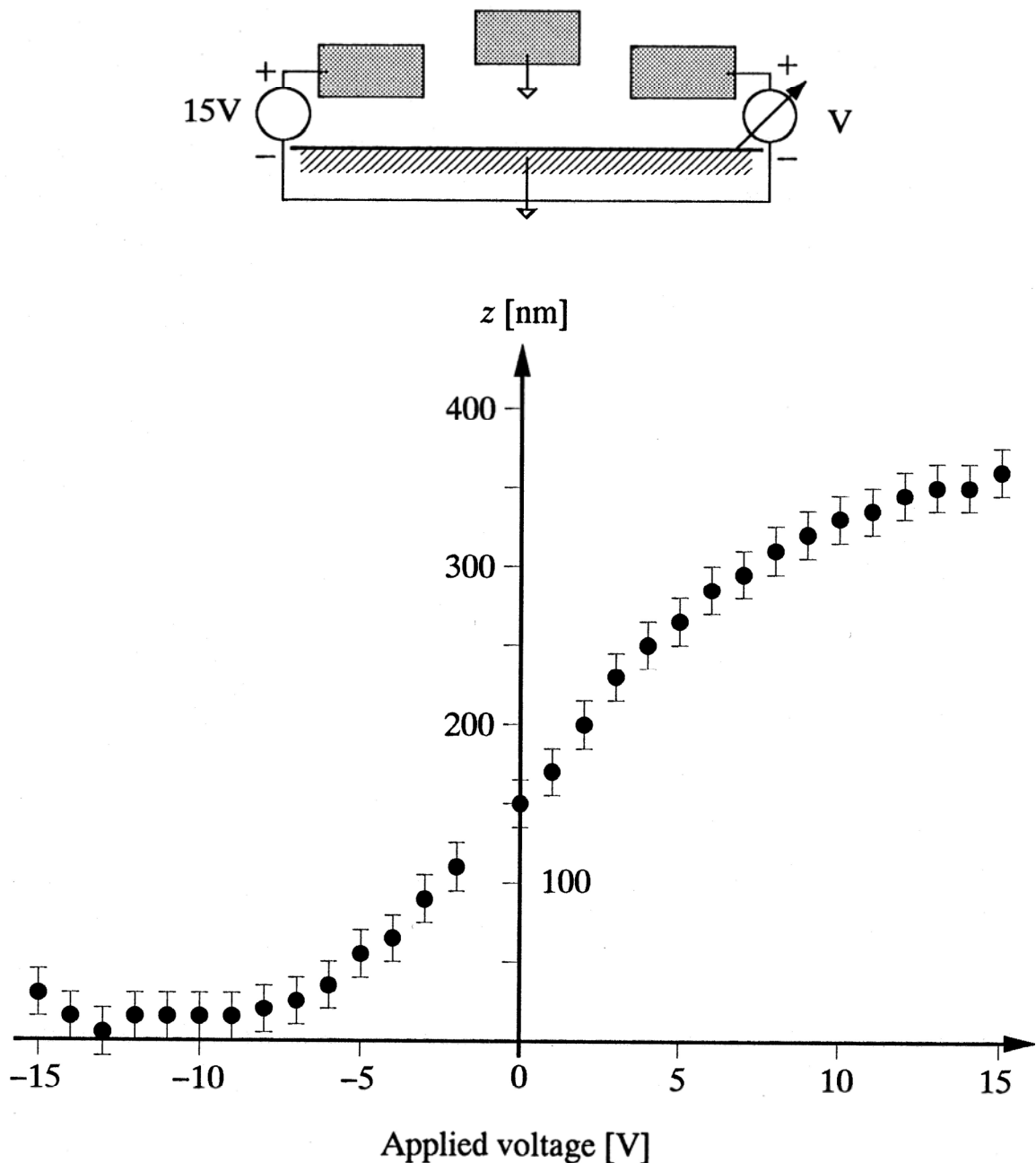


Figure 4.24 Vertical displacement of prototype V1 for varying voltage on one electrode from -15 V to +15 V, while holding the other electrode fixed at +15 V.

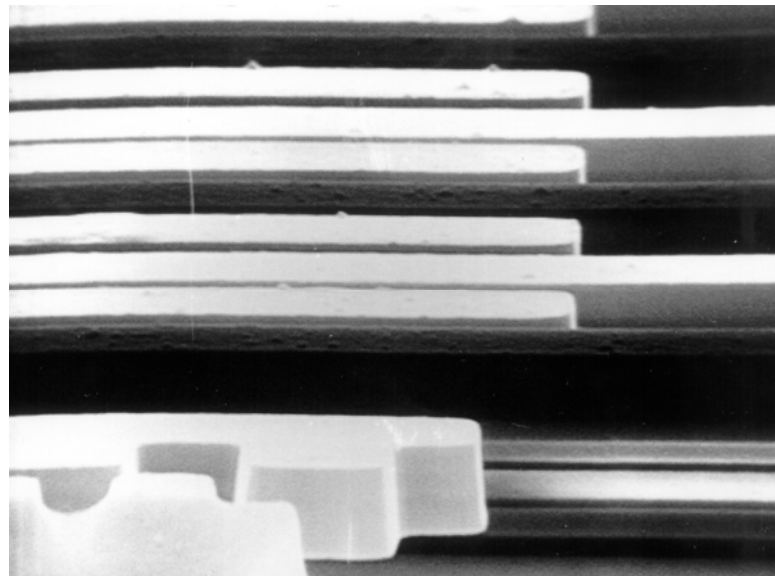


Figure 4.25 SEM of prototype V1 under ± 10 V balanced biasing on the alternating drive fingers, indicating almost no levitation. Fingers at higher potentials appear darkened due to voltage-contrast effect in SEM.

4.4.2 Vertical and Lateral Drive Capacities

It is found that, besides suppressing the vertical levitation, the balanced-biasing approach on the alternating drive fingers induces a weaker lateral force on the structure than the unbalanced comb. The balanced comb is advantageous only if the tradeoff between levitation suppression and loss of lateral drive is favorable. In order to quantify the comparison of the lateral and vertical force reductions, we define the lateral drive capacity, γ_x , of an electrostatic-comb drive as the lateral force induced per square of the

applied voltage:

$$\gamma_x = \frac{F_x}{V_p^2} \quad [\text{pN}\cdot\text{V}^{-2}] \quad (4.9)$$

The value of γ_x is normalized to each drive finger, and is found to be $16 \pm 1 \text{ pN}\cdot\text{V}^{-2}$ per drive finger for all the unbalanced comb designs. Both γ_z and γ_x for the V-series prototypes are tabulated in Table 4.IX. The reductions in γ are defined as the ratios of the drive capacities of the unbalanced comb to those of the balanced one.

Table 4.IX Normalized γ_z and γ_x per drive finger for V-series prototypes

Type	γ_z at $z = 0$ $\pm 1 \text{ pN}\cdot\text{V}^{-2}$	γ_x $\pm 1 \text{ pN}\cdot\text{V}^{-2}$	γ_z reduction	γ_x reduction
Unbalanced	47	16	-	-
V1	3	10	16:1	1.6:1
V2	26	8	1.8:1	2:1
V3	30	11	1.6:1	1.5:1
V4	35	12	1.3:1	1.3:1
V5	36	14	1.3:1	1.1:1
V6	38	14	1.2:1	1.1:1

Although none of the comb designs completely eliminates the levitation as predicted by idealized theory, which assumes evenly spaced comb fingers with vertical sidewalls, the V1 prototype stands out as the best approach, with a 16:1 reduction on the vertical drive capacity while suffering only a 1.6:1 reduction in induced lateral force. All of the other interdigitation methods are ineffective.

4.4.3 Vertical Resonant Frequencies

The vertical resonant frequencies for prototype V1 are found by stepping the output frequency of an *HP 4192A LF Impedance Analyzer* at 0.1 Hz steps at different dc biases from 5.0 V to 15.0 V, and fixing the ac drive amplitude at 50 mV. Figure 4.26 is the SEM of prototype V1 driven into vertical resonance. The vibration amplitude is estimated to be 2 μm peak-to-peak. The results are plotted in Fig. 4.27, with the theoretical curve fitted to the data with z_0 and γ_z adjusted to 400 nm and 47 $\text{pN}\cdot\text{V}^{-2}$, respectively.

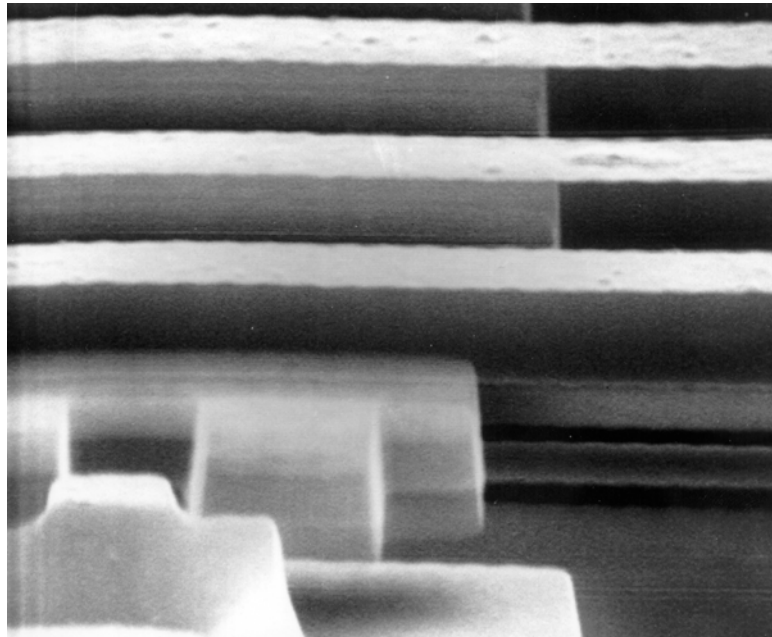


Figure 4.26 SEM of prototype V1 driven into vertical resonance under a 50 mV ac drive on top of a 5 V dc bias.

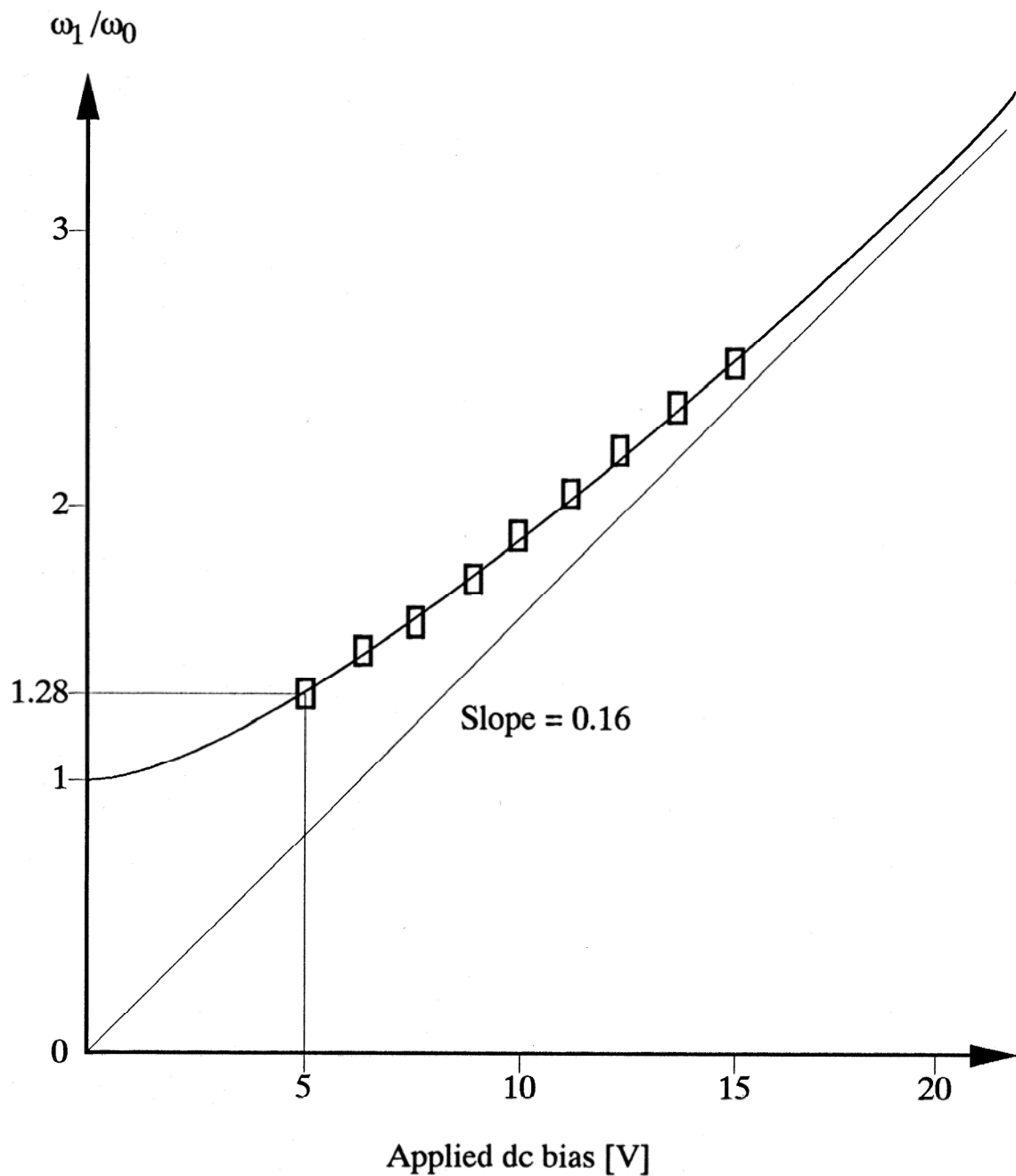


Figure 4.27 Measured and fitted vertical resonant frequencies of prototype V1 as a function of dc bias.

The -3 dB bandwidth appears to be about 20 Hz for all the vertical resonant frequencies, which would put the value for Q at between 250 and 500, depending on the resonant frequencies. However, the Q is evaluated to be close to 50,000 using the time-domain method (see section 4.2.2), which is the same as the lateral Q . The apparently excessive -3 dB bandwidth may be due to the highly nonlinear function of vertical resonant frequency on the drive voltage. Since the vertical position is also a function of the applied voltage, the large vibration amplitude of 2 μm peak-to-peak indicates that the vertical resonance is in the nonlinear region even at an ac drive level of 50 mV. Nevertheless, the excellent fit of the first order theory with the experimental results verifies the usefulness of the frequency-shifting phenomenon as a way to control vertical resonant frequency.

4.5 SUMMARY

In this chapter we have presented the measurement techniques and have analyzed the static and dynamic characteristics of both the lateral and vertical modes of operations. The large-amplitude resonance, which is characteristic of the electrostatic comb drive with the folded-beam suspension, enables straightforward measurements of the motions by direct observations with either optical microscope or SEM. The modulation-based testing technique provides an electrical verification of the observed measurements. Although the nonuniform thickness and built-in stress of the deposited polysilicon film and the less-than-ideal plasma etching step affect the characteristics of the finished structures slightly, the basic functional advantages of the comb-drive structure such as large vibration amplitude, linearity, and the ability to control vertical motions are realized. The robustness of the laterally-driven microstructures is further demonstrated by the excellent fit of the first-order theories with the measurement results for both lateral and vertical modes of operation.

Chapter 5

ACTUATOR APPLICATION EXAMPLE

In the previous chapters, we have established the first-order theory, described the processing techniques and compared the experimental and theoretical results of the lateral and vertical modes of motion of the electrostatic-comb structures. This chapter describes the design and theory of a two-dimensional manipulator as an example of applying the comb drive as an actuating element. The manipulator can be used potentially to improve the performance of a resonant micromotor. The structure can be analyzed with an approach similar to that developed in Chapter 2 and fabricated with the same surface-micromachining technique described in Chapter 3.

5.1 TWO-DIMENSIONAL MANIPULATOR

In robotics system applications, complicated multidimensional motions are usually achieved by mechanically coupling an array of one-dimensional actuators capable of performing periodic rotary or linear motions. Stepper motors and electromagnetic resonators are common examples of one-dimensional periodic actuators.

One of the simplest forms of actuator coupling based on the electrostatic-comb drive is illustrated in Fig. 5.1, which shows the basic design of an orthogonally coupled

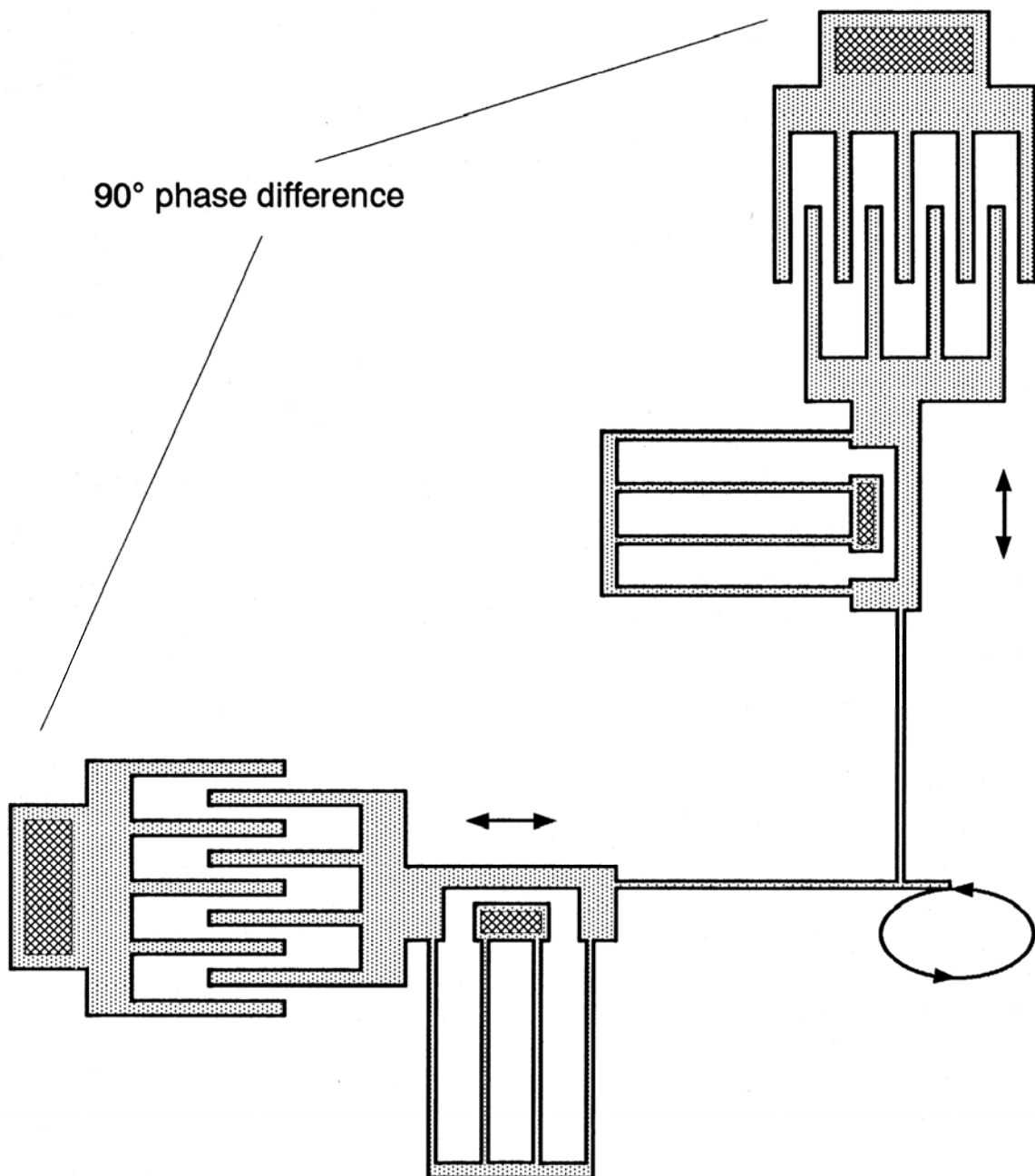


Figure 5.1 Basic design of an orthogonally coupled comb-drive pair to form a two-dimensional manipulator.

comb-drive pair to form a two-dimensional manipulator. The combs are resonated by sinewave signals at 90° -phase difference to achieve circular or elliptical motions on the pawl tip. If the lateral-drive capacities of the combs are sufficiently high to statically deflect the suspensions, then any arbitrary motions can be obtained by independently driving the combs at off-resonant, low-frequency modes.

5.2 RESONANT MICROMOTOR APPLICATION

The two-dimensional manipulator can be far more versatile than a single comb-drive resonator in many applications. An example is the resonant-structure micromotor concept briefly described in Section 2.2 of Chapter 2. The original suggested micromotor is based on a tuning-fork actuating element, where the vibration energy is used to turn a gear wheel with a ratchet-and-pawl mechanism (Fig. 5.2) [30]. This concept can be implemented using a comb drive as the actuator as illustrated in Fig. 5.3.

A critical design issue is the interaction between the pawl tip and the gear tooth, where tooth interference and friction must be considered carefully [72]. Figure 5.4 is the close-up view of the pawl tip and the gear wheel in resting position. When the vibration of the pawl builds up to a sufficient amplitude to push forward the gear wheel, the subsequent tooth will move into a position where the pawl motion is interfered, as illustrated in Fig. 5.5. The frictional force between the pawl and the tooth, if sufficiently large, may drag the wheel in the backward direction when the pawl retracts. One or more passive ratchets are usually placed along the perimeter of the wheel to prevent backward motion. However, excessive friction between the gear teeth and the pawls and ratchets may prove fatal to the micromotor.

In order to reduce friction and to eliminate the need for passive ratchets, it is desirable to engage the gear wheel with elliptical pawl tip motions (Fig. 5.6). To further reduce the stress on the hub, two pawls can be used on the opposite sides of the wheel to eliminate translational force at the center of the wheel.

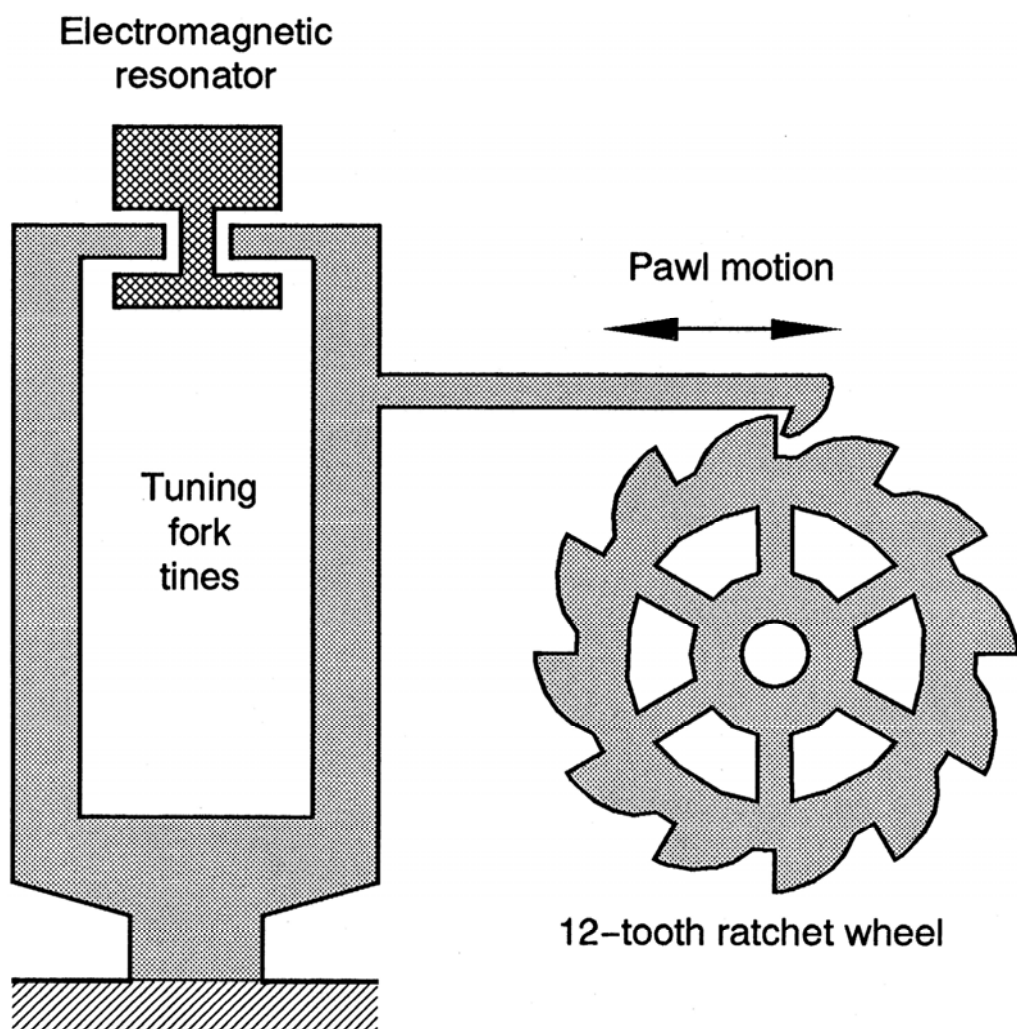


Figure 5.2 Resonant-structure micromotor concept [30].

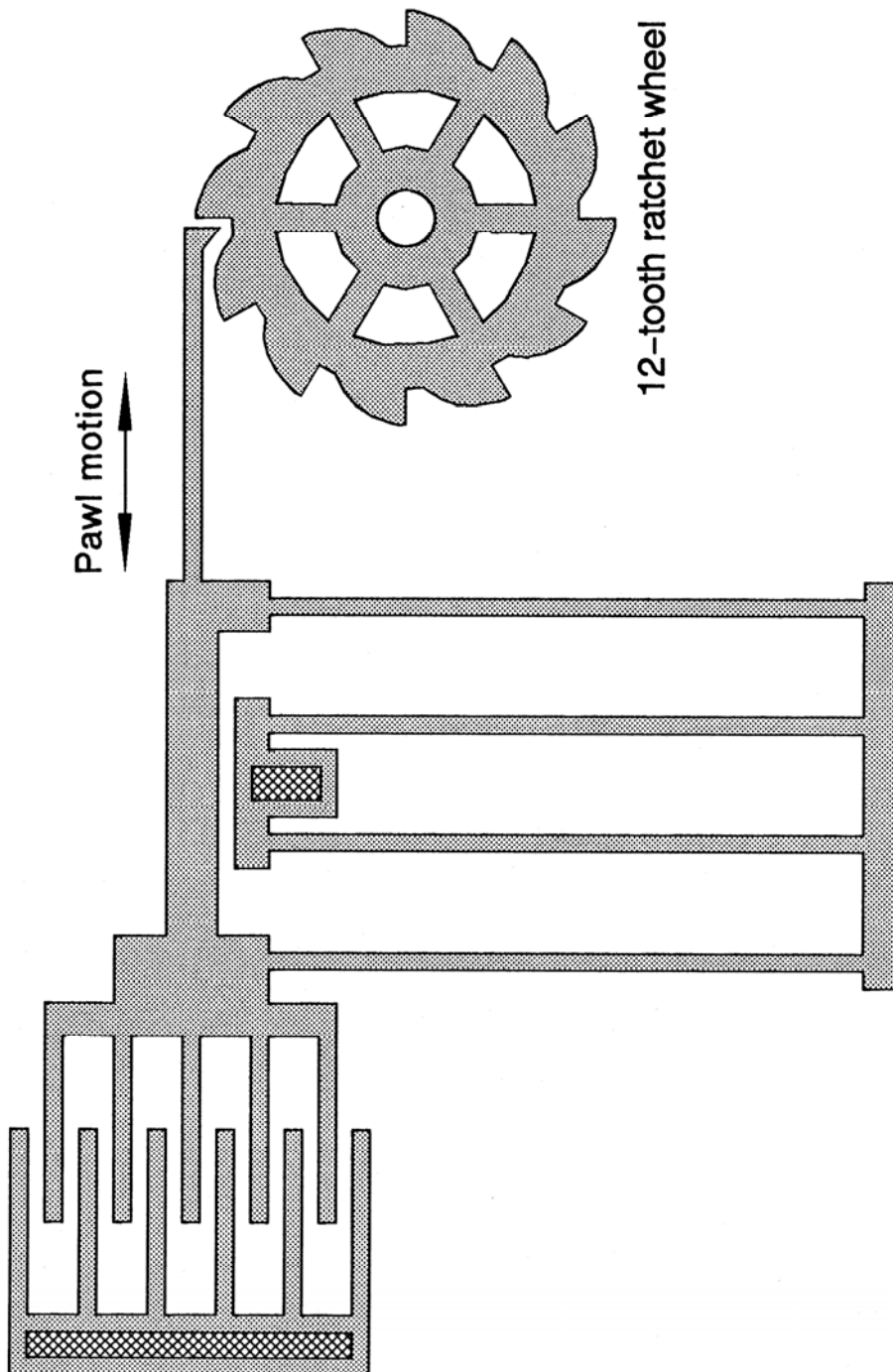


Figure 5.3 Resonant micromotor implemented with the comb drive as the actuating element.

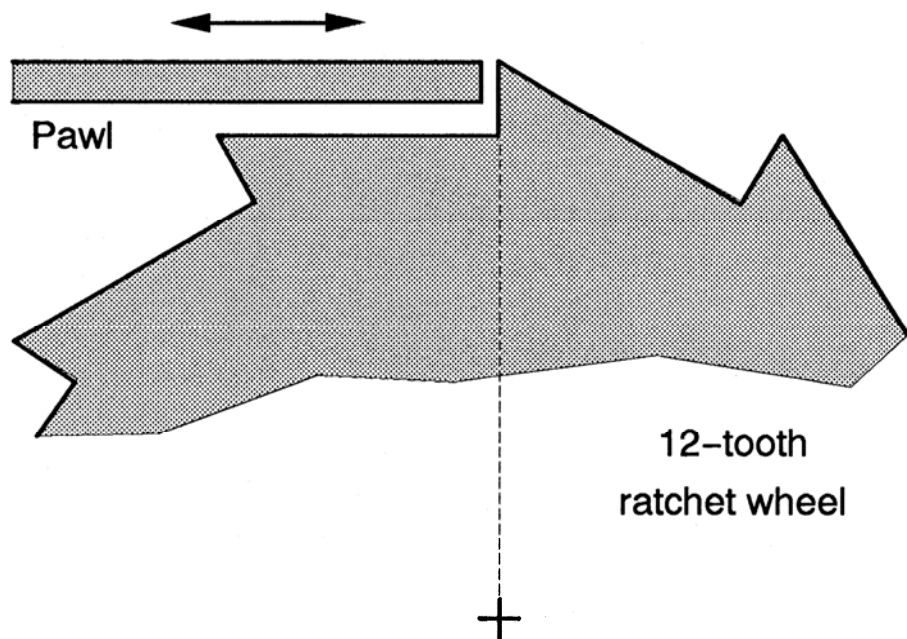


Figure 5.4 Pawl and gear wheel in resting position.

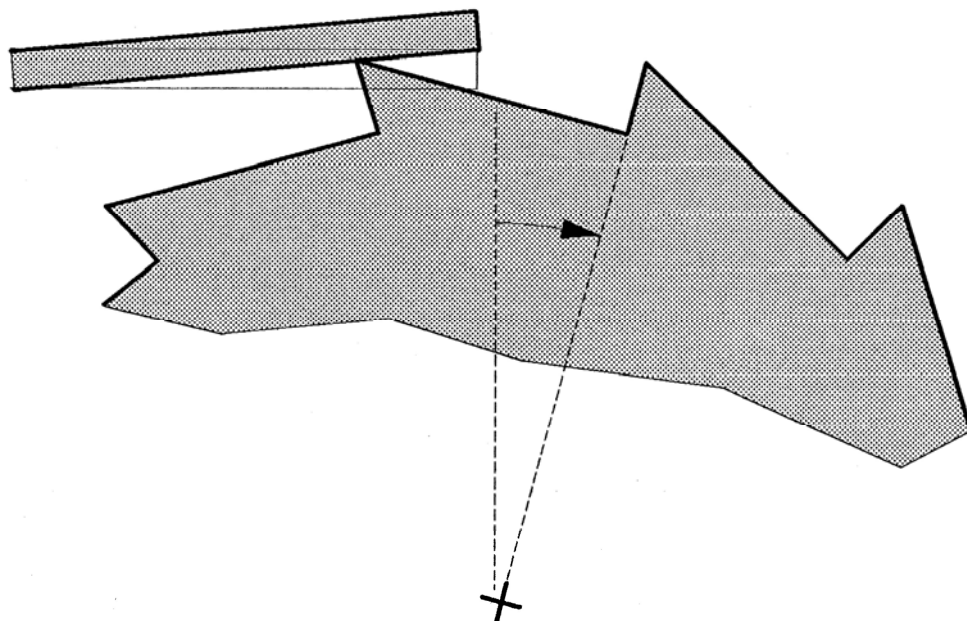


Figure 5.5 Pawl and gear wheel interference.

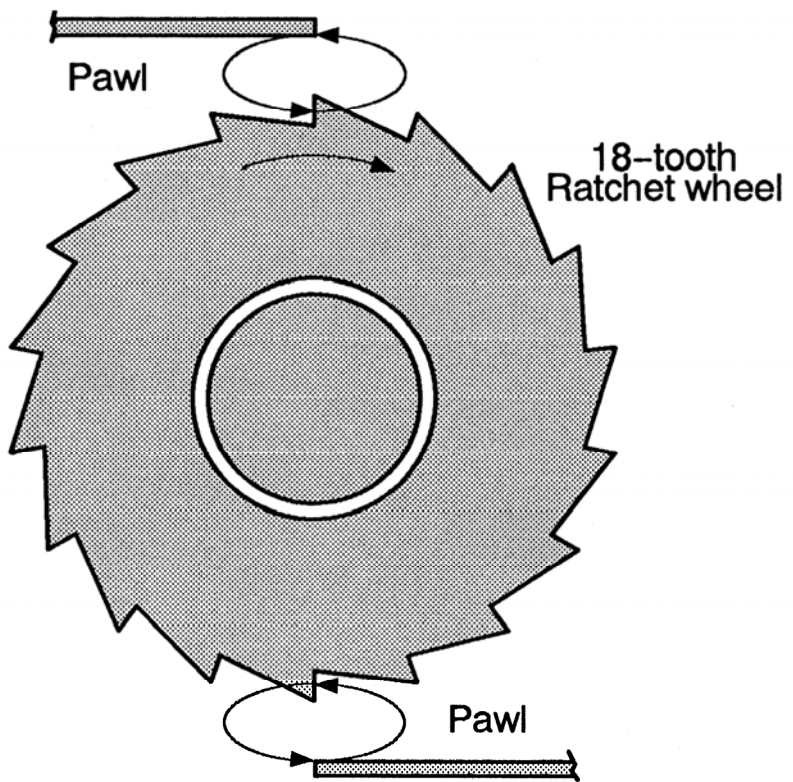


Figure 5.6 Improved pawl-ratchet engagement with elliptical pawl motions.

5.3 STABILITY AND DESIGN CONSIDERATIONS

Operation of the two-dimensional manipulator requires that the coupled pawls are compliant in sideways motion to avoid inducing excessive sideways force on the comb drive. The simulation results of the spring constants of serpentine-spring supports described in Section 2.3.2.2 of Chapter 2 can be used as a design guideline for the coupled pawls. Figure 5.7 is the redesigned gear wheel with a pair of orthogonally coupled serpentine springs as flexible pawls. Note that square teeth are used instead of saw teeth such that the gear wheel can be turned in either directions. In this case, push-

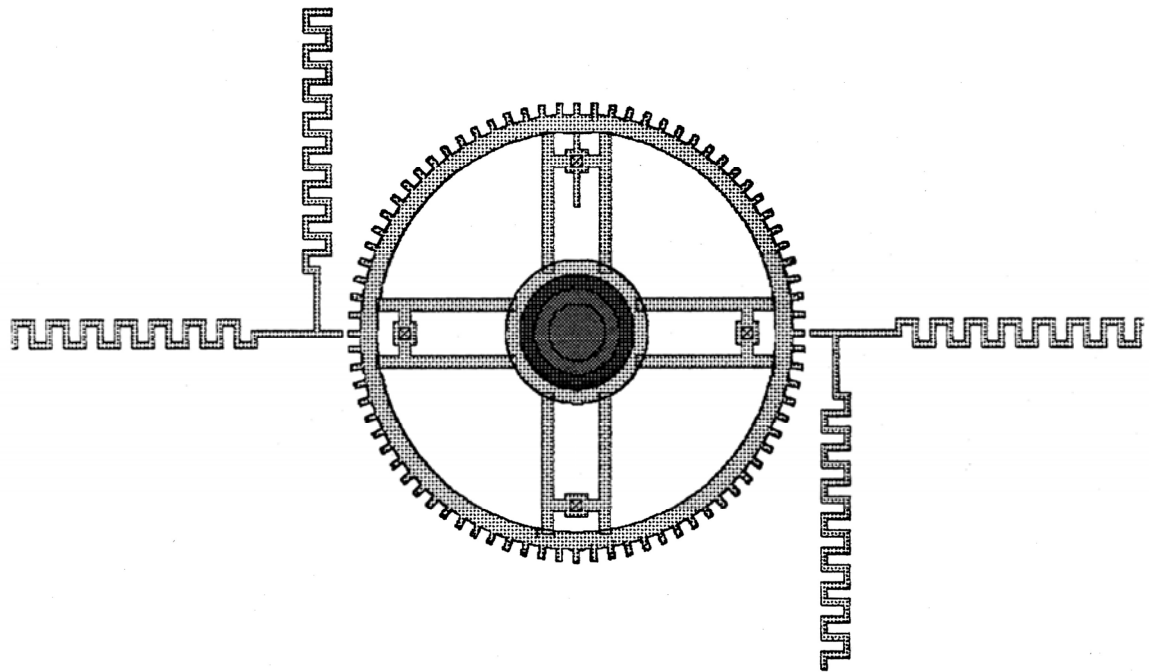


Figure 5.7 Modified resonant micromotor with differential elliptical drives.

pull drives are needed for the pawls.

In order to provide push-pull capability and increased lateral drive capacity for off-resonant operation, the comb-drive structure is modified as shown in Fig. 5.8. Alternating drive fingers are employed in the design to minimize the effect of levitation. A single-folded supporting beam is used instead of the more compact double-folded one to obtain better lateral stiffness.

As an example, Fig. 5.9 is the simulated mode shape of an orthogonally coupled pawl when a force is induced on the x -axis actuator. The dimensions of each of the serpentine spring in this example are (see Section 2.3.2.2 of Chapter 2)

$$N_m = 8, W_m = 8 \mu\text{m}, \text{ and beam cross section} = 2 \mu\text{m} \times 2 \mu\text{m}.$$

The spring constant for this coupled pawl in the x direction, k_x , is simulated to be 619 $\text{nN}\cdot\mu\text{m}^{-1}$, which is more than two-and-a-half times higher than the 233 $\text{nN}\cdot\mu\text{m}^{-1}$ value for simple bending of a single serpentine pawl with the same dimensions (see Section 2.3.2.2 of Chapter 2). The value for k_y , the coupled spring constant in the y direction, is equal to k_x since the two serpentine supports are identically dimensioned. It is desirable for k_x to be as small as possible such that the lateral load on the y -axis actuator is minimized. Similarly, a small k_y minimizes the lateral load on the x -axis actuator. The resonant frequency for the whole manipulator is calculated from the system spring constant, which is the sum of the spring constant of the folded-beam support and that of the orthogonally coupled pawl.

For the particular design illustrated in Fig. 5.8, the orthogonally coupled serpentine

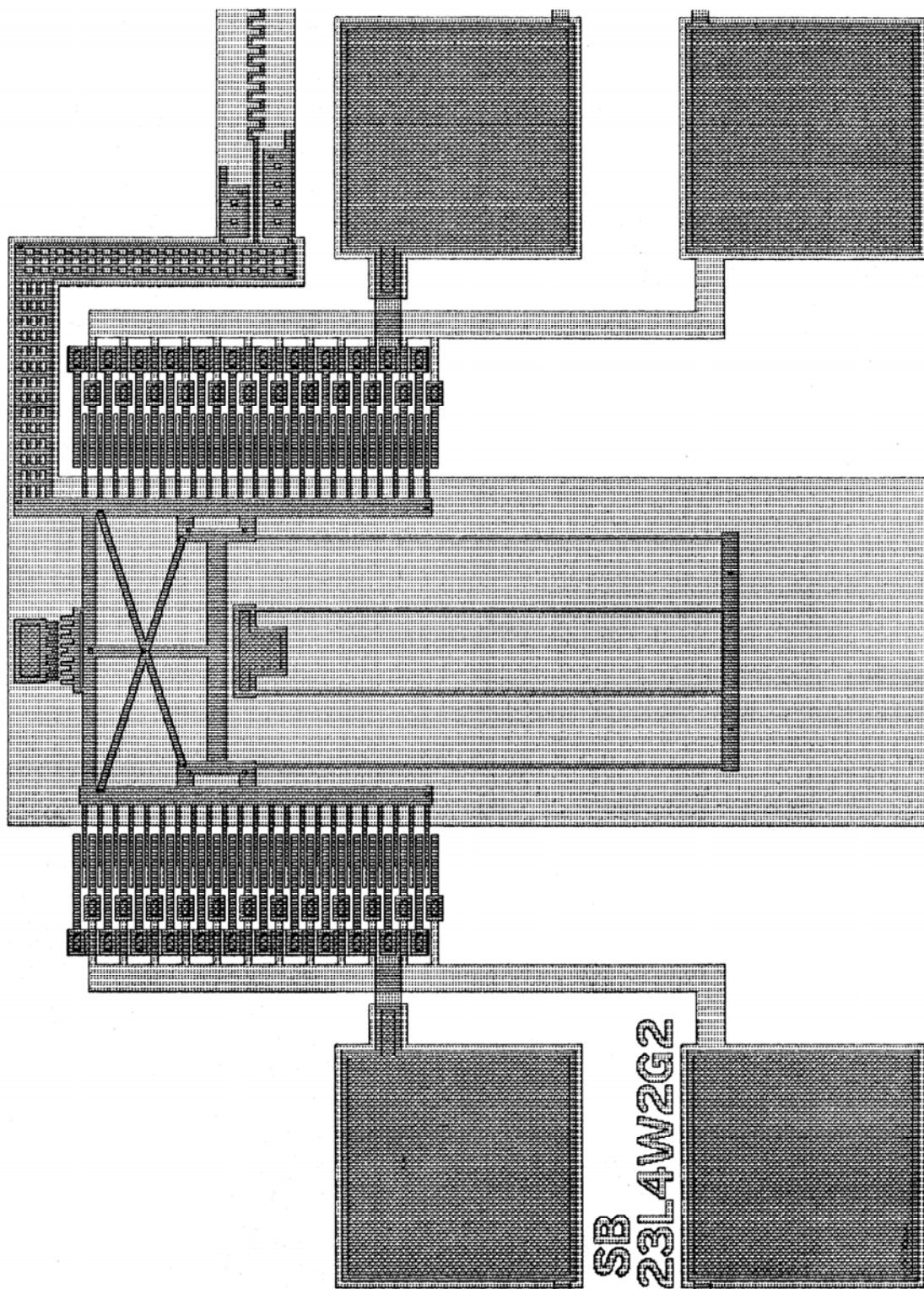


Figure 5.8 Push-pull comb-drive actuator.

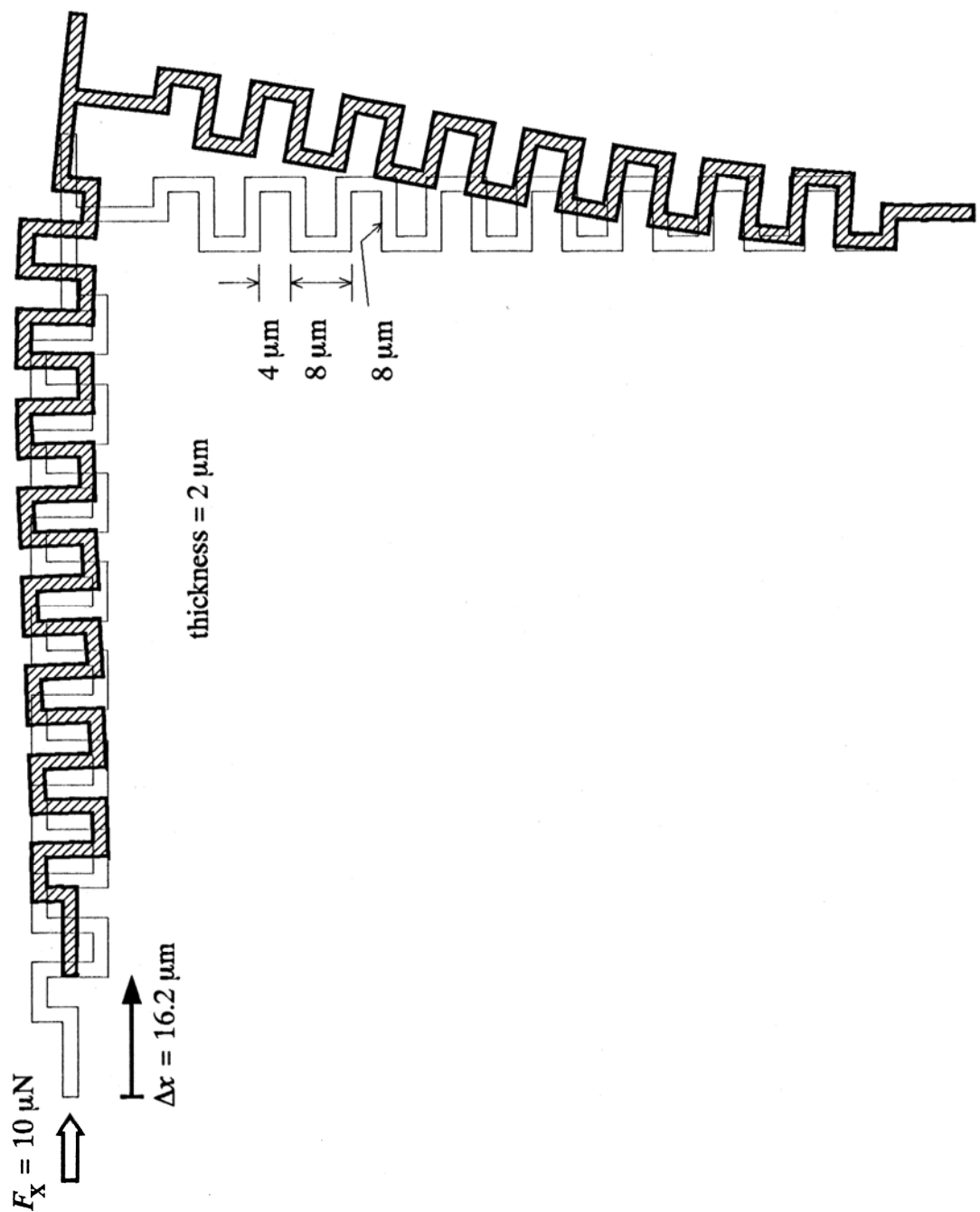


Figure 5.9 Model shape of an orthogonally coupled serpentine spring pair under a force F_x .

pawl is designed with the following dimensions:

$$N_m = 33, W_m = 8 \mu\text{m}, \text{ and beam cross section} = 2 \mu\text{m} \times 2 \mu\text{m}.$$

The simulated spring constant of this design is

$$k_x|_{\text{pawl}} = 8.8 \text{ nN}\cdot\mu\text{m}^{-1} \quad (5.1)$$

The spring constant of the 300 μm -long, one-sided, single-folded spring support is calculated with Eq. (2.45) (see Section 2.3.1.1 of Chapter 2). Since we now have a one-sided support, the spring constant is

$$k_x|_{\text{beam}} = \frac{24EI_z}{2L^3} = \frac{Ehw^3}{L^3} = 89 \text{ nN}\cdot\mu\text{m}^{-1} \quad (5.2)$$

which is more than ten times the value of $k_x|_{\text{pawl}}$. Given the even higher ratio of $k_y|_{\text{beam}}$ to $k_x|_{\text{beam}}$, the sideways bending of the pawl will have negligible effect on the normal operation of the associated comb drive. The resonant frequency is then calculated with Eq. (2.71) of Section 2.3.1.3 of Chapter 2, and is found to be 3.82 kHz.

The lateral drive capacity (γ_x) for the push-pull actuator in Fig. 5.8 is evaluated to be $0.74 \text{ nN}\cdot\text{V}^{-2}$ based on the experimental results described in Chapter 4. Thus, a $\pm 30 \text{ V}$ differential bias applied to the two sides of the push-pull comb drive will induce a static deflection of

$$\Delta x = \frac{F_x}{k_x|_{\text{beam}} + k_x|_{\text{pawl}}} = \frac{2 \times (30 \text{ V})^2 \times 0.74 \text{ nN}\cdot\text{V}^{-2}}{(89 + 8.8) \text{ nN}\cdot\mu\text{m}^{-1}} = 13.6 \mu\text{m}$$

which is more than sufficient to statically manipulate the gear wheel.

In order to shed light on the forces between the pawls and the gear teeth, a

microdynamometer is designed with similar dimensions as the resonant micromotor, except that the gear wheel is supported by a pair of Archimedean spirals with two needles added to the perimeter of the wheel to indicate the amount of deflection (Fig. 5.10).

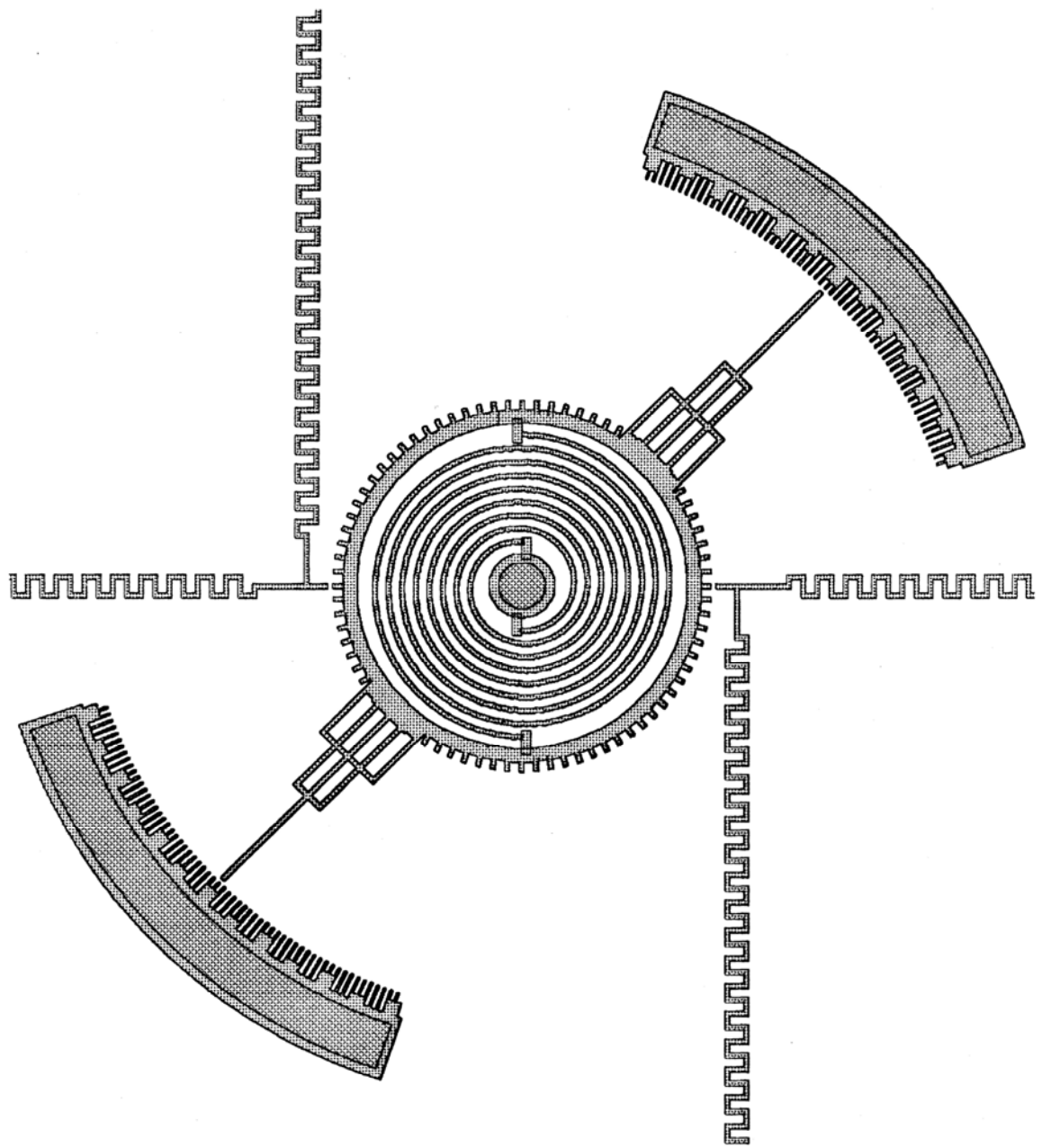


Figure 5.10 Microdynamometer with Archimedean spiral supports.

5.4 SUMMARY

We have discussed the theory of the two-dimensional manipulator as an extension of the electrostatic-comb drive to demonstrate possible applications in resonant micromotor and microdynamometer. The major potential advantage of the proposed manipulator is its increased versatility without adding processing steps. Initial calculations indicated that it is feasible to statically move the manipulator pawl tip in any arbitrary large-amplitude planar motions parallel to the substrate. However, the theory is yet to be verified.

Chapter 6

CONCLUSIONS

We conclude the thesis with this final chapter by evaluating the surface-micromachined electrostatic-comb drive in light of the research goal, which is to establish a foundation for electrostatically exciting and sensing suspended micromachined transducer elements. The merits and weaknesses of the lateral-drive approach are evaluated, based on the potential applications of resonant sensors and actuators for micromechanical systems, and we point to the direction for future research.

6.1 EVALUATION OF THIN-FILM ELECTROSTATIC-COMB DRIVE

Since tribology at the micron-sized domain is not well understood, the general development of microactuators is concentrated either in basic research on friction and other related micromechanical properties, or in frictionless or minimal-friction devices. The key to the development of a frictionless microstructure is the availability of robust flexure suspensions that can sustain repetitive cycles of motion in a predetermined manner. Also, an efficient and compatible periodic energy source is needed for excitation. We have taken the full advantage of the well-established planar-IC technology to develop and demonstrate suspended planar micromechanical devices capable of large-amplitude motions that are driven and sensed electrostatically.

LPCVD polycrystalline silicon is chosen as the material for the spring suspensions and other associated mechanical parts simply because of its mature micromachining technology. Plasma-etched microstructures are superior in their fracture toughness because of its ability to disperse stress concentrations due to the absence of sharply angled corners.

Arbitrary shapes can be easily patterned in one masking step with the lateral-drive approach. At the minimum, one masking step is sufficient to fabricate functioning electrostatic-comb drives. The linearity and efficiency of the electrostatic-comb drive have been shown to be advantageous for microactuator applications. Since the levitation phenomenon has been sufficiently analyzed and a control method has been experimentally verified, it can be used as a functioning feature of the electrostatic-comb drive. Finally, a two-dimensional manipulator design is theoretically feasible as an example of building geometrically sophisticated planar structures without adding processing steps.

However, the limited thickness of all thin-film processed microstructures, including the electrostatic-comb drive, may inherently restrict its usefulness in certain applications. The following section discusses this issue from the perspective of geometrical scaling.

6.2 SCALING CONSIDERATION AND ALTERNATIVE PROCESS

As discussed in Section 2.1.2 of Chapter 2, since $\partial C/\partial x \approx 2\alpha\epsilon hg^{-\beta}$ per drive finger, it is desirable to decrease the finger gap g and increase the thickness h to enhance the drive efficiency. Also, increased film thickness is advantageous for improving mechanical stability of the finished structures. However, for a 2 μm -thick polysilicon film, conventional photolithography and plasma-etching techniques would place a lower limit on resolving g to probably no less than 1 μm . Also, a near-vertical sidewall would be more difficult to obtain at decreased gap clearances. To increase h , a thick polysilicon film can be deposited at the expense of long deposition time and accelerated need for furnace tube maintenance. However, thicker films are progressively more difficult to pattern because of the obscured alignment mark, except in the case of the single-mask process. The use of non-erodible mask would become necessary for the extended plasma-etch step for thick films. To form the non-erodible mask, a two-step approach is usually adopted where an intermediate layer of photoresist is first patterned to define the mask which is then used to pattern the underlying polysilicon film after the photoresist layer is optionally removed. This two-step approach may degrade the feature resolution, and thus increasing the minimum resolvable g . Therefore, the processing steps described in Chapter 3, if not extensively modified, are best suited for film thickness of 4 μm or less, with a gap clearance of at least 1 μm .

Extending beyond conventional IC technology, recent research has provided alternatives to create microstructures with high aspect ratios [73–75]. Using deep-etch,

high-energy X-ray lithography with a synchrotron and specialized developer, polymeric photoresist as thick as 300 μm has been patterned to form the mold for depositing metals onto the exposed areas of the underlying conductive substrate by electroforming [73]. Minimum separation between structures as small as 3 μm was achieved, with excellent vertical sidewalls [73]. The use of deep UV source for lithography has also been reported to obtain structures as thick as 8 μm without the need for synchrotron [74]. If a suitable sacrificial material is used with these processes, the single-mask electrostatic-comb drive, which does not require mask alignment through the thick photoresist, can be realized with excellent drive efficiency and mechanical stability.

Another processing approach was also recently introduced which uses a combination of deep-boron diffusion as a wet-etch stop and a long plasma etch with thick CVD oxide as a mask to create thick microstructures from the bulk substrate silicon material [75]. The etched microstructures are electrostatically bonded onto a glass substrate with patterned metal interconnects, followed by a final wet etch to remove the sacrificial silicon. This process promises structure thickness as high as 20 μm and a gap separation as small as 1 μm , providing pedestal supports without step-coverage problems.

Although on-chip integration with signal-processing circuits is extremely difficult with these processes, the greatly enhanced drive efficiency will provide sufficiently strong signals and sensitivity that closed-loop operation may be possible even with an adjacent hybrid-packaged IC chip.

6.3 FUTURE RESEARCH

An immediate research topic is to demonstrate the feasibility of the two-dimensional manipulator described in Chapter 5 as an actuator for the resonant micromotor and the microdynamometer. Since these designs require long structural beams and a third polysilicon layer to form the center hub for the motor, additional process development may be necessary to address the need to further reduce the built-in differential stress, step-coverage problem and extended final sacrificial etch. If the use of silicon-rich nitride as passivation layer becomes necessary for the extended wet etch, rapid-thermal annealing (RTA) may be explored as an alternative for the polysilicon stress anneal to avoid nitride layer blistering [35].

The present process compatibility with IC technology can be exploited to develop on-chip circuit integration to achieve closed-loop operation [64]. There is a need to demonstrate the feasibility of RTA to stress anneal the polysilicon film without permanently damaging the CMOS circuits and the tungsten metalization [64].

Finally, extending beyond the use of polysilicon to build microstructures and PSG as sacrificial material, alternative materials based on different technologies may be advantageous for the comb-drive design, as discussed in the previous section. The same approach may be explored to build the single-mask electrostatic-comb drive for improved drive efficiency and reduced built-in stress.

REFERENCES

- [1] K. E. Petersen, "Silicon as a mechanical material," *Proceedings of the IEEE*, vol. 70, pp. 420–457, May 1982.
- [2] R. S. Muller, "From IC's to microstructures: materials and technologies," *Proceedings, IEEE Micro Robots and Teleoperators Workshop*, Hyannis, Mass., November 9–11, 1987.
- [3] M. Mehregany, K. J. Gabriel, and W. S. N. Trimmer, "Integrated fabrication of polysilicon mechanisms," *IEEE Trans. Electron Devices*, vol. ED-35, pp. 719–723, 1988.
- [4] T. A. Lober and R. T. Howe, "Surface-micromachining processes for electrostatic microactuator fabrication," *Technical Digest, IEEE Solid-State Sensor and Actuator Workshop*, Hilton Head Island, SC., June 6–9, 1988, pp. 59–62.
- [5] K. Hjort, J.-A. Schweitz, and B. Hök, "Bulk and surface micromachining of GaAs structures," *Technical Digest, IEEE Micro Electro Mechanical Systems Workshop*, Napa Valley, CA., February 11–14, 1990, pp. 73–76.
- [6] Y.-C. Tai, "IC-processed polysilicon micromechanics: technology, material, and devices," Ph.D. Thesis, Dept. of Electrical Engineering and Computer Sciences, University of California at Berkeley, Berkeley, CA., Sept. 1989.
- [7] M. Mehregany, "Microfabricated silicon electric mechanisms," Ph.D. Thesis, Dept. of Electrical Engineering and Computer Science, Massachusetts Institute of Technology, May 1990.
- [8] L.-S. Fan, "Integrated micromachinery: moving structures on silicon chips," Ph.D. Thesis, Dept. of Electrical Engineering and Computer Sciences, University of California at Berkeley, Berkeley, CA., Dec. 1989.
- [9] W. S. N. Trimmer, K. J. Gabriel and R. Mahadevan, "Silicon electrostatic motors," *Technical Digest, 4th International Conference on Solid-State Sensors and Actuators*, Tokyo, Japan, June 2–5, 1987, pp. 857–860.

- [10] M. Esashi, S. Shoji, and A. Nakano, "Normally close microvalve and micropump fabricated on a silicon wafer," *Technical Digest*, IEEE Micro Electro Mechanical Systems Workshop, Salt Lake City, Utah, February 20–22, 1989, pp. 29–34.
- [11] H. Jerman, "Electrically-activated micromachined diaphragm valves," *Technical Digest*, IEEE Solid-State Sensor and Actuator Workshop, Hilton Head Island, SC., June 4–7, 1990, pp. 65–69.
- [12] F. Pourahmadi, L. Cristel, K. Petersen, J. Mallon, and J. Bryzek, "Variable-flow micro-valve structure fabricated with silicon fusion bonding," *Technical Digest*, IEEE Solid-State Sensor and Actuator Workshop, Hilton Head Island, SC., June 4–7, 1990, pp. 78–81.
- [13] F. C. M. van de Pol, H. T. G. van Lintel, M. Elwenspoek, and J. H. J. Fluitman, "A thermopneumatic micropump based on micro-engineering techniques," *Proceedings vol. 2, 5th International Conference on Solid-State Sensors and Actuators*, Montreux, Switzerland, June 25–30, 1989, pp. 198–202.
- [14] M. A. Huff, M. S. Mettner, T. A. Lober, and M. A. Schmidt, "A pressure-balanced electrostatically-actuated microvalve," *Technical Digest*, IEEE Solid-State Sensor and Actuator Workshop, Hilton Head Island, SC., June 4–7, 1990, pp. 123–127.
- [15] M. J. Zdeblick, "A planar process for an electric-to-fluidic valve," Ph.D. Thesis, Dept. of Electrical Engineering, Stanford University, June 1988.
- [16] R. T. Howe, "Resonant microsensors," *Technical Digest*, 4th International Conference on Solid-State Sensors and Actuators, Tokyo, Japan, June 2–5, 1987, pp. 843–848.
- [17] M. A. Schmidt and R. T. Howe, "Resonant structures for integrated sensors," *Technical Digest*, IEEE Solid-State Sensor and Actuator Workshop, Hilton Head Island, SC., June 2–5, 1986, pp. 94–97.
- [18] R. M. Langdon, "Resonator sensors—a review," *J. Phys. E: Sci. Inst.*, vol. 18, pp. 103–115, 1985.
- [19] E. P. EerNisse and J. M. Paros, "Practical considerations for miniature quartz resonator force transducers." *Proceedings, 37th Annual Symposium on Frequency Control*, pp. 255–260, 1983.

- [20] W. C. Albert, "Vibrating quartz crystal beam accelerometer," *Proceedings, 28th ISA International Instrumentation Symposium*, pp. 33–44, 1982.
- [21] E. Karrer and R. Ward, "A low-range quartz resonator pressure transducer," *ISA Trans.*, vol. 16, pp. 90–98, 1977.
- [22] J. Hlavay and G. G. Guilbault, "Application of the piezoelectric crystal detector in analytical chemistry," *Analytical Chemistry*, vol. 49, pp. 1890–1898, 1977.
- [23] H. Wohltjen, "Mechanism of operation and design considerations for surface acoustic wave device vapour sensors," *Sensors and Actuators*, vol. 5, pp. 307–325, 1984.
- [24] S. J. Martin, K. S. Schweizer, A. J. Ricco, and T. E. Zipperian, "Gas sensing with surface acoustic wave devices," *Technical Digest, 3rd International Conference on Solid-State Sensors and Actuators*, Philadelphia, Penn., June 11–14, 1985, pp. 71–73.
- [25] J. G. Smits, H. A. C. Tilmans, and T. S. J. Lammerink, "Pressure dependence of resonant diaphragm pressure sensors," *Technical Digest, 3rd International Conference on Solid-State Sensors and Actuators*, Philadelphia, Penn., June 11–14, 1985, pp. 93–96.
- [26] J. C. Greenwood, "Etched silicon vibrating sensor," *J. Phys. E: Sci. Inst.*, vol. 17, pp. 650–652, 1984.
- [27] K. Ikeda, H. Kuwayama, T. Kobayashi, T. Watanabe, T. Nishikawa, and T. Yoshida, "Silicon pressure sensor with resonant strain gauges built into diaphragm," *Technical Digest, 7th Sensor Symposium*, Tokyo, Japan, May 30–31, 1988, pp. 55–58.
- [28] D. C. Satchell and J. C. Greenwood, "Silicon microengineering for accelerometers," *Proc. Inst. of Mech. Eng.*, vol. 1987–2, Mechanical Technology of Inertial Devices, Newcastle, England, April 7–9, 1987, pp. 191–193.
- [29] R. T. Howe and R. S. Muller, "Resonant-microbridge vapor sensor," *IEEE Trans. Electron Devices*, vol. ED-33, pp. 499–506, 1986.

- [30] A. P. Pisano, "Resonant-structure micromotors," *Technical Digest, IEEE Micro Electro Mechanical Systems Workshop*, Salt Lake City, Utah, February 20–22, 1989, pp. 44–48.
- [31] W. Benecke, A. Heuberger, W. Reithmüller, U. Schnakenberg, H. Wölfelschneider, R. Kist, G. Knoll, S. Ramakrishnan, and H. Höfflin, "Optically excited mechanical vibrations in micromachined silicon cantilever structures," *Technical Digest, 4th International Conference on Solid-State Sensors and Actuators*, Tokyo, Japan, June 2–5, 1987, pp. 838–842.
- [32] H. C. Nathanson, W. E. Newell, R. A. Wickstrom, and J. R. Davis, Jr., "The resonant gate transistor," *IEEE Trans. Electron Devices*, vol. ED-14, pp. 117–133, 1967.
- [33] K. E. Petersen and C. R. Guarnieri, "Young's modulus measurements of thin films using micromechanics," *J. Appl. Phys.*, vol. 50, pp. 6761–6766, 1979.
- [34] D. W. DeRoo, "Determination of Young's modulus of polysilicon using resonant micromechanical beams," M.S. Report, Dept. of Electrical and Computer Engineering, University of Wisconsin-Madison, Jan. 1988.
- [35] M. W. Putty, "Polysilicon resonant microstructures," M.S. Report, Dept. of Electrical Engineering and Computer Science, The University of Michigan, Ann Arbor, Mich., Sept. 1988.
- [36] M. A. Schmidt, "Microsensors for the measurement of shear forces in turbulent boundary layers," Ph.D. Thesis, Massachusetts Institute of Technology, Cambridge, Mass., May 1988.
- [37] M. A. Schmidt, R. T. Howe, S. D. Senturia, and J. H. Haritonidis, "Design and calibration of a microfabricated floating-element shear-stress sensor," *IEEE Trans. Electron Devices*, vol. ED-35, pp. 750–757, 1988.
- [38] W. C. Tang, T.-C. H. Nguyen, and R. T. Howe, "Laterally driven polysilicon resonant microstructures," *Sensor and Actuators*, vol. 20, pp. 25–32, 1989.
- [39] W. C. Tang, T.-C. H. Nguyen, M. W. Judy, and R. T. Howe, "Electrostatic-comb drive of lateral polysilicon resonators," *Proceedings vol. 2, 5th International Conference on Solid-State Sensors and Actuators*, Montreux, Switzerland, June 25–30, 1989, pp. 328–331.

- [40] W. C. Tang, M. G. Lim, and R. T. Howe, "Electrostatically balanced comb drive for controlled levitation," *Technical Digest*, IEEE Solid-State Sensor and Actuator Workshop, Hilton Head Island, SC., June 4–7, 1990, pp. 23–27.
- [41] *Maxwell Solver, Electrostatic Package* v. 4.20, Ansoft Corp., 4 Station Square, 660 Commerce Court Building, Pittsburgh, Pa. 15219.
- [42] S. S. Rao, *Mechanical Vibrations*, Reading: Addison-Wesley, 1986.
- [43] Y.-C. Tai, L. S. Fan, and R. S. Muller, "IC-processed micromotors: design, technology, and testing," *Technical Digest*, IEEE Micro Electro Mechanical Systems Workshop, Salt Lake City, Utah, February 20–22, 1989, pp. 1–6.
- [44] M. Mehregany, P. Nagarkar, S. D. Senturia, and J. H. Lang, "Operation of microfabricated harmonic and ordinary side-drive motors," *Technical Digest*, IEEE Micro Electro Mechanical Systems Workshop, Napa Valley, CA., February 12–14, 1990, pp. 1–8.
- [45] J. M. Gere and S. P. Timoshenko, *Mechanics of Materials*, 2nd ed. Belmont: Wadsworth, 1984.
- [46] A. P. Pisano, University of California at Berkeley, personal communication.
- [47] A. P. Pisano and Y.-H. Cho, "Mechanical design issues in laterally-driven microstructures," *Proceedings vol. 2, 5th International Conference on Solid-State Sensors and Actuators*, Montreux, Switzerland, June 25–30, 1989, pp. 1060–1064.
- [48] F. M. White, *Viscous Fluid Flow*, New York: McGraw-Hill, 1974.
- [49] C. J. Chen, L.-D. Chen, and F. M. Holly, Jr., eds., *Turbulence Measurements and Flow Modeling*, Washington: Harper & Row, 1987.
- [50] L. D. Clayton, S. R. Swanson, and E. P. Eernisse, "Modifications of the double-ended tuning fork geometry for reduced coupling to its surroundings: finite element analysis and experiments," *IEEE Trans. Ultrasonics, Ferroelectrics, and Frequency Control*, vol. UFFC-34, pp. 243–252, 1987.
- [51] A. M. Wahl, *Mechanical Springs*, 1st ed. Cleveland: Penton, 1945.
- [52] *SuperSAP*, Algor Interactive Systems, Inc., Essex House, Pittsburgh, Penn. 15206.

- [53] R. T. Howe, "Integrated silicon electromechanical vapor sensor," Ph.D. Thesis, Dept. of Electrical Engineering and Computer Sciences, University of California at Berkeley, Berkeley, CA., Dec. 1984.
- [54] L. A. Field, University of California at Berkeley, personal communication.
- [55] R. T. Howe and R. S. Muller, "Polycrystalline and amorphous silicon micro-mechanical beams: annealing and mechanical properties," *Sensors and Actuators*, vol. 4, pp. 447–454, 1983.
- [56] H. Guckel, T. Randazzo, and D. W. Burns, "A simple technique for the determination of mechanical strain in thin films with application to polysilicon," *J. Appl. Phys.*, vol. 57, no. 5, pp. 1671–1675, 1985.
- [57] T. A. Lober, J. Huang, M. A. Schmidt, and S. D. Senturia, "Characterization of the mechanisms producing bending moments in polysilicon micro-cantilever beams by interferometric deflection measurements," *Technical Digest, IEEE Solid-State Sensor and Actuator Workshop*, Hilton Head Island, SC., June 6–9, 1988, pp. 92–95.
- [58] H. Guckel, D. W. Burns, H. A. C. Tilmans, D. W. DeRoo, and C. R. Rutigliano, "Mechanical properties of fine grained polysilicon: the repeatability issue," *Technical Digest, IEEE Solid-State Sensor and Actuator Workshop*, Hilton Head Island, SC., June 6–9, 1988, pp. 96–99.
- [59] L. S. Fan, R. S. Muller, W. Yun, R. T. Howe, and J. Huang, "Spiral microstructures for the measurement of average strain Gradients in thin films," *Technical Digest, IEEE Micro Electro Mechanical Systems Workshop*, Napa Valley, CA., February 11–14, 1990, pp. 177–181.
- [60] H. Guckel, D. W. Burns, H. A. C. Tilmans, C. C. G. Visser, D. W. DeRoo, T. R. Christenson, P. J. Klomberg, J. J. Sniegowski, and D. H. Jones, "Processing conditions for polysilicon films with tensile strain for large aspect ratio micro-structures," *Technical Digest, IEEE Solid-State Sensor and Actuator Workshop*, Hilton Head Island, SC., June 6–9, 1988, pp. 51–54.
- [61] L. S. Fan and R. S. Muller, "As-deposited low-strain LPCVD polysilicon," *Technical Digest, IEEE Solid-State Sensor and Actuator Workshop*, Hilton Head Island, SC., June 6–9, 1988, pp. 55–58.

- [62] T. A. Lober and R. T. Howe, "Surface-micromachining processes for electrostatic microactuator fabrication," *Technical Digest, IEEE Solid-State Sensor and Actuator Workshop*, Hilton Head Island, SC., June 6–9, 1988, pp. 59–62.
- [63] D. W. Burns, "Micromechanics of integrated sensors and the planar processed pressure transducer," Ph.D. Thesis, Dept. of Electrical and Computer Engineering, University of Wisconsin-Madison, May 1988.
- [64] W. Yun, W. C. Tang, and R. T. Howe, "Fabrication technologies for integrated microdynamic systems," *Technical Digest, 3rd Toyota Conference*, Aichi-ken, Japan, October 22–25, 1989, pp. 17-1–17-15.
- [65] M. W. Putty, S. C. Chang, R. T. Howe, A. L. Robinson, and K. D. Wise, "Process integration for active polysilicon resonant microstructures," *Sensors and Actuators*, vol. 20, pp. 143–151, 1989.
- [66] J. Huang, University of California at Berkeley, unpublished data.
- [67] M. G. Lim, University of California at Berkeley, unpublished data.
- [68] M. W. Judy, University of California at Berkeley, unpublished data.
- [69] D. Hebert, University of California at Berkeley, personal communication.
- [70] J. J. Bernstein, Charles Stark Draper Laboratory, personal communication.
- [71] D. M. Manos and D. L. Flamm, ed., *Plasma etching, an introduction*, Boston: Academic Press, 1989.
- [72] A. P. Pisano, University of California at Berkeley, personal communication.
- [73] W. Ehrfeld, F. Götz, D. Münchmeyer, W. Schelb, and D. Schmidt, "LIGA process: sensor construction techniques via X-Ray lithography," *Technical Digest, IEEE Solid-State Sensor and Actuator Workshop*, Hilton Head Island, SC., June 6–9, 1988, pp. 1–4.
- [74] H. Guckel, T. R. Christenson, K. J. Skrobis, D. D. Denten, B. Choi, E. G. Lovell, J. W. Lee, S. S. Bajikar, and T. W. Chapman, "Deep X-ray and UV lithographies for micromechanics," *Technical Digest, IEEE Solid-State Sensor and Actuator Workshop*, Hilton Head Island, SC., June 4–7, 1990, pp. 118–122.

- [75] K. Suzuki and H. Tanigawa, "Alternative process for silicon linear micro-actuators," *Technical Digest, IEE of Japan 9th Sensor Symposium*, Tokyo, Japan, 1990, pp. 125–128.

Appendix A PROCESS FLOW

The following describes the standard processing steps used in all three experimental runs, except for slight variations in fabrication details.

A.1 Defused Ground Plane Definition

equipment: tylan8

recipe name: POCL3

recipe highlights:

1. Initial temperature = 750°C
2. Load wafers
3. Ramp temperature up to 1000°C in 20 min
4. Stabilize temperature for 10 min
5. Turn on POCl₃ for 2 hr
6. Shut off POCl₃
7. Ramp temperature down to 750°C in 20 min
8. End

A.2 Wet Oxidation

target: 5000 Å wet oxide (growth rate ≈ 4600 Å·hr⁻¹)

equipment: tylan1 or 2

recipe name: SWETOXB

recipe highlights:

1. Initial temperature = 750°C
2. Initial N₂ flow rate = 1000 sccm
3. Load wafers
4. Ramp temperature up to 1000°C in 15 min
5. Loop back for 2 min until temperature stabilizes
6. Change N₂ flow rate to 200 sccm
7. Preoxidation (dry) with O₂ flowing at 4000 sccm for 5 min
8. Turn off N₂
9. Wet oxidation with steam and O₂ at 200 sccm for 1 hr 5 min
10. Turn off steam

11. Purge with O₂ flowing at 4000 sccm for 5 min
12. Turn off O₂
13. Anneal with N₂ flowing at 4000 sccm for 20 min
14. Change N₂ flow rate to 1000 sccm
15. Ramp temperature down to 750°C in 20 min
16. End

A.3a Nitride Deposition (alternative 1)

target: 1700 Å stoichiometric nitride (deposition rate \approx 1700 Å·hr⁻¹)

equipment: tylan9

recipe name: SNITC

recipe highlights:

1. Initial temperature = 750°C
2. Initial N₂ flow rate = 1000 sccm
3. Load wafers
4. Change N₂ flow rate to 100 sccm
5. Short pump for 2 min
6. Ramp temperature up to 800°C in 12 min
7. Loop back for 2 min until temperature stabilizes
8. Turn off N₂
9. Hard pump for 2 min
10. Leak check for 2 min
11. Pre-deposition purge for 2 min with NH₃ = 75 sccm
12. Deposition with SiH₂Cl₂ = 25 sccm, NH₃ = 75 sccm, pressure = 160 mtorr, time = 1 hr
13. Post-deposition purge for 40 sec with SiH₂Cl₂ turned off
14. Turn off NH₃ and hard pump for 1 min
15. Flush with N₂ flowing at 100 sccm and hold for user acknowledgement

A.3b Nitride Deposition (alternative 2)

target: 5000 Å silicon-rich, low-stress nitride (deposition rate \approx 2200 Å·hr⁻¹)

equipment: tylan9

recipe name: SNITC.V

recipe highlights:

1. Initial temperature = 750°C
2. Initial N₂ flow rate = 1000 sccm

3. Load wafers
4. Change N₂ flow rate to 180 sccm
5. Short pump for 2 min
6. Ramp temperature up to 835°C in 12 min
7. Loop back for 2 min until temperature stabilizes
8. Turn off N₂
9. Hard pump for 2 min
10. Leak check for 30 sec
11. Turn on N₂, flow rate = 180 sccm
12. Short pump for 3 min
13. Turn off N₂
14. Second hard pump for 2 min
15. Second leak check for 2 min
16. Pre-deposition purge for 1 min 30 sec with NH₃ = 16 sccm
17. Set pressure control
18. Deposition with SiH₂Cl₂ = 64 sccm, NH₃ = 16 sccm, pressure = 300 mtorr, time = 2 hr 20 min
19. Post-deposition purge for 40 sec with SiH₂Cl₂ turned off and pressure control turned off
20. Turn off NH₃ and hard pump for 1 min
21. Flush with N₂ flowing at 180 sccm and hold for user acknowledgement

A.4 Diffusion Contact Definition

target: 2 μm-thick patterned negative photoresist

equipments: Eaton wafer track, GCA Wafer Stepper, MTI Omnichuck Developer, Technics-c plasma etcher

recipe highlights:

1. Dehydrate at 120°C for 1 hr
2. Expose to HMDS vapor for 1 min
3. Spin on KTI 820 negative G-line photoresist: thickness = 2 μm
4. Soft bake with Eaton hot chuck at 120°C for 1 min
5. Expose with GCA Wafer Stepper: exposure time = 1.5× dark field
6. Post-exposure bake at 120°C for 1 min with Eaton hot chuck.
7. Develop with 2:1 KTI 934 developer in Omnichuck: time = standard
8. Descum in Technics-c: O₂ = 50 sccm, power = 50 W, time = 1 min
9. Hard bake at 120°C for > 5 hr

A.5 Diffusion Contact Etch

target: etch through nitride and oxide (nitride plasma-etch rate $\approx 1200 \text{ \AA}\cdot\text{min}^{-1}$, oxide wet-etch rate $\approx 8000 \text{ \AA}\cdot\text{min}^{-1}$)

equipments: technics-c, wet sink

recipe highlights:

1. Timed plasma etch for nitride: $\text{SF}_6 = 13 \text{ sccm}$, $\text{He} = 21 \text{ sccm}$, power = 200 W, time $\approx 1 \text{ min } 30 \text{ sec}$
2. Timed wet etch for oxide: 10:1 diluted-HF bath, time $\approx 45 \text{ sec}$

A.6 Clean

target: prepare wafers for doped-polysilicon deposition

equipments: Technics-c, wet sinks

recipe highlights:

1. Photoresist ashing in Technics-c: $\text{O}_2 = 50 \text{ sccm}$, power = 400 W, time = 10 min
2. Cleaning: piranha clean in Sink8 for 20 min, rinse in DI water up to 10 $\text{M}\Omega\cdot\text{cm}$
3. Final cleaning: piranha clean in Sink6 for 20 min, rinse in DI water up to 14 $\text{M}\Omega\cdot\text{cm}$
4. Brief dip (5 sec) in 10:1 HF
5. Final rinse with DI water to 16 $\text{M}\Omega\cdot\text{cm}$
6. Spin dry at 2000 rpm for 2 min

A.7 First Polysilicon Deposition

target: 3000 \AA -thick doped polysilicon (deposition rate $\approx 2400 \text{ \AA}\cdot\text{hr}^{-1}$)

equipments: tylan11

recipe name: SDOPOLYG

recipe highlights:

1. Initial temperatures: load zone = 644°C , center = 650°C , source zone = 656°C
2. Initial N_2 flow rate = 1000 sccm
3. Load wafers
4. Change N_2 flow rate to 35 sccm
5. Short pump for 2 min
6. Wait for temperature to recover after loading

7. Loop back until temperature stabilizes
8. Turn off N₂
9. Hard pump for 2 min
10. Leak check for 1 min
11. Hard pump for 1 min
12. Turn on phosphine: PH₃ = 1.0 sccm, time = 1 min
13. Deposition: SiH₄ = 120 sccm, pressure = 310 mtorr, time = 1 hr 15 min
14. Pump: SiH₄ = PH₃ = 0, time = 1 min
15. Purge: N₂ = 50 sccm
16. Hold for user acknowledgement

A.8 First Poly Definition

target: 1 μm -thick patterned negative photoresist

equipments: Eaton wafer track, GCA Wafer Stepper, MTI Omnichuck Developer, Technics-c plasma etcher

recipe highlights:

1. Dehydrate at 120°C for 1 hr
2. Expose to HMDS vapor for 1 min
3. Spin on KTI 820 negative G-line photoresist: thickness = 1 μm
4. Soft bake with Eaton hot chuck at 120°C for 1 min
5. Expose with GCA Wafer Stepper: exposure time = standard bright field
6. Post-exposure bake at 120°C for 1 min with Eaton hot chuck.
7. Develop with 2:1 KTI 934 developer in Omnichuck: time = standard
8. Hard bake at 120°C for > 5 hr

A.9 First Poly Etch

target: pattern poly1 (etch rate \approx 3200 $\text{\AA}\cdot\text{min}^{-1}$)

equipments: lam1, wet sink

recipe highlights:

1. Brief dip in 5:1 buffered HF to remove oxide
2. Rinse to 10 M $\Omega\cdot\text{cm}$ in Sink8
3. Spin dry at 2000 rpm for 2 min
4. Lam1 etch with automatic 90% endpoint detection after 20 sec and 25% overetch: pressure = 280 mtorr, power = 300 W, gap = 1.5 cm, CCl₄ = 130 sccm, O₂ = 15 sccm, He = 130 sccm

A.10 Clean

target: prepare wafers for PSG deposition

equipments: Technics-c, wet sinks

recipe highlights:

1. Photoresist ashing in Technics-c: $O_2 = 50$ sccm, power = 400 W, time = 10 min
2. Cleaning: piranha clean in Sink8 for 20 min, rinse in DI water up to $10 M\Omega \cdot cm$
3. Final cleaning: piranha clean in Sink6 for 20 min, rinse in DI water up to $14 M\Omega \cdot cm$
4. Brief dip (5 sec) in 10:1 HF
5. Final rinse with DI water to $16 M\Omega \cdot cm$
6. Spin dry at 2000 rpm for 2 min

A.11 First PSG Deposition

target: 2 μm of PSG (deposition rate $\approx 8000 \text{ \AA} \cdot \text{hr}^{-1}$)

equipment: tylan12

recipe name: SDOLTOD

recipe highlights:

1. Initial temperature = $450^\circ C$
2. Initial N_2 flow rate = 1000 sccm
3. Load wafers
4. Change N_2 flow rate to 100 sccm
5. Pump for 2 min
6. Stabilize temperature for 15 min or loop back
7. Turn off N_2
8. Hard pump for 2 min
9. Leak check for 1 min
10. Hard pump for 1 min
11. gasflow stabilization: $SiH_4 = 60$ sccm, $PH_3 = 5$ sccm, $O_2 = 90$ sccm, pressure = 300 mtorr, time = 1 min
12. Deposition: time = 2 hr 30 min
13. Pump for 1 min, gases shut down
14. Purge for 1 min, $N_2 = 100$ sccm
15. Second pump for 1 min, with N_2 turned off
16. Second purge for 1 min, $N_2 = 100$ sccm

17. Hold for user acknowledgement

A.12 PSG Densification

target: densify PSG at 950°C for 1 hr

equipment: tylan7

recipe name: N2ANNEAL

recipe highlights:

1. Initial temperature = 750°C
2. Initial N₂ flow rate = 1000 sccm
3. Load wafers
4. Change N₂ flow rate to 2000 sccm
5. Ramp temperature up to 950°C in 15 min
6. Stabilize temperature for 5 min
7. Anneal: N₂ = 2000 sccm, time = 1 hr
8. Ramp temperature down to 750°C in 5 min
9. End

A.13 Dimple Definition

target: 1 μm-thick patterned negative photoresist

equipments: Eaton wafer track, GCA Wafer Stepper, MTI Omnichuck Developer, Technics-c plasma etcher

recipe highlights:

1. Dehydrate at 120°C for 1 hr
2. Expose to HMDS vapor for 1 min
3. Spin on KTI 820 negative G-line photoresist: thickness = 1 μm
4. Soft bake with Eaton hot chuck at 120°C for 1 min
5. Expose with GCA Wafer Stepper: exposure time = standard dark field
6. Post-exposure bake at 120°C for 1 min with Eaton hot chuck.
7. Develop with 2:1 KTI 934 developer in Omnichuck: time = standard
8. Descum in Technics-c: O₂ = 50 sccm, power = 50 W, time = 1 min
9. Hard bake at 120°C for 5 hr

A.14 Dimple Etch

target: pattern 1 μm-deep dimple (etch rate ≈ 4000 Å·min⁻¹)

equipments: lam2

recipe highlights:

1. Etch: pressure = 2.8 torr, power = 350 W, gap = 0.38 cm, CHF₃ = 30 sccm, CF₄ = 90 sccm, He = 120 sccm, time = 1 min
2. Idle: power = 0, gases continue, time = 1 min
3. Etch: pressure = 2.8 torr, power = 350 W, gap = 0.38 cm, CHF₃ = 30 sccm, CF₄ = 90 sccm, He = 120 sccm, time = 1 min
4. Idle: power = 0, gases continue, time = 1 min
5. Etch: pressure = 2.8 torr, power = 350 W, gap = 0.38 cm, CHF₃ = 30 sccm, CF₄ = 90 sccm, He = 120 sccm, time = 30 sec

A.15 Clean

target: prepare wafers for second photoresist coating

equipments: Technics-c, wet sinks

recipe highlights:

1. Photoresist ashing in Technics-c: O₂ = 50 sccm, power = 400 W, time = 10 min
2. Cleaning: piranha clean in Sink8 for 20 min, rinse in DI water up to 10 MΩ·cm
3. Spin dry at 2000 rpm for 2 min

A.16 Anchor Definition

target: 2 μm-thick patterned negative photoresist

equipments: Eaton wafer track, GCA Wafer Stepper, MTI Omnichuck Developer, Technics-c plasma etcher

recipe highlights:

1. Dehydrate at 120°C for 1 hr
2. Expose to HMDS vapor for 1 min
3. Spin on KTI 820 negative G-line photoresist: thickness = 2 μm
4. Soft bake with Eaton hot chuck at 120°C for 1 min
5. Expose with GCA Wafer Stepper: exposure time = 1.5× dark field
6. Post-exposure bake at 120°C for 1 min with Eaton hot chuck.
7. Develop with 2:1 KTI 934 developer in Omnichuck: time = standard
8. Descum in Technics-c: O₂ = 50 sccm, power = 50 W, time = 1 min
9. Hard bake at 120°C for > 5 hr

A.17 Anchor Etch

target: open anchors (etch rate $\approx 8000 \text{ \AA}\cdot\text{min}^{-1}$ both plasma and wet)

equipments: lam2, wet sink

recipe highlights:

1. Lam2 etch: pressure = 2.8 torr, power = 350 W, gap = 0.38 cm, CHF_3 = 30 sccm, CF_4 = 90 sccm, He = 120 sccm, time = 1 min
2. Idle: power = 0, gases continue, time = 1 min
3. Lam2 etch: pressure = 2.8 torr, power = 350 W, gap = 0.38 cm, CHF_3 = 30 sccm, CF_4 = 90 sccm, He = 120 sccm, time = 1 min
4. Wet wafer in DI for 30 sec
5. 5:1 buffered HF etch for 1 min
6. Rinse up to $10 \text{ M}\Omega\cdot\text{cm}$

A.18 Clean

target: prepare wafers for structural-polysilicon deposition

equipments: Technics-c, wet sinks

recipe highlights:

1. Photoresist ashing in Technics-c: O_2 = 50 sccm, power = 400 W, time = 10 min
2. Cleaning: piranha clean in Sink8 for 20 min, rinse in DI water up to $10 \text{ M}\Omega\cdot\text{cm}$
3. Final cleaning: piranha clean in Sink6 for 20 min, rinse in DI water up to $14 \text{ M}\Omega\cdot\text{cm}$
4. Brief dip (5 sec) in 10:1 HF
5. Final rinse with DI water to $16 \text{ M}\Omega\cdot\text{cm}$
6. Spin dry at 2000 rpm for 2 min

A.19 Second Polysilicon Deposition

target: $2 \mu\text{m}$ -thick undoped polysilicon (deposition rate $\approx 7000 \text{ \AA}\cdot\text{hr}^{-1}$)

equipment: tylan11

recipe name: SUNPOLYA

recipe highlights:

1. Initial temperatures: load zone = 605°C , center = 610°C , source zone = 615°C
2. Initial N_2 flow rate = 1000 sccm

3. Load wafers
4. Change N₂ flow rate to 100 sccm
5. Short pump for 2 min
6. Temperature recover and stabilization
7. Turn off N₂
8. Hard pump for 2 min
9. Leak check for 1 min
10. Turn on N₂, flow rate = 200 sccm
11. Pump down for 30 sec
12. Turn off N₂
13. Gasflow stabilization: SiH₄ = 120 sccm, time = 1 min
14. Deposition: time = 2 hr 50 min
15. Hard pump for 30 sec, gas off
16. Purge: N₂ = 100 sccm for 1 min
17. Hold for user acknowledgement

A.20 Second PSG Deposition

target: 3000 Å of top PSG (deposition rate \approx 8000 Å·hr⁻¹)

equipment: tylan12

recipe name: SDOLTOD

recipe highlights:

1. Initial temperature = 450°C
2. Initial N₂ flow rate = 1000 sccm
3. Load wafers
4. Change N₂ flow rate to 100 sccm
5. Pump for 2 min
6. Stabilize temperature for 15 min or loop back
7. Turn off N₂
8. Hard pump for 2 min
9. Leak check for 1 min
10. Hard pump for 1 min
11. gasflow stabilization: SiH₄ = 60 sccm, PH₃ = 5 sccm, O₂ = 90 sccm, pressure = 300 mtorr, time = 1 min
12. Deposition: time = 22 min
13. Pump for 1 min, gases shut down
14. Purge for 1 min, N₂ = 100 sccm

15. Second pump for 1 min, with N₂ turned off
16. Second purge for 1 min, N₂ = 100 sccm
17. Hold for user acknowledgement

A.21 Doping and Stress Anneal

target: dope and stress anneal 2nd poly at 1050°C for 1 hr

equipment: tylan7

recipe name: N2ANNEAL

recipe highlights:

1. Initial temperature = 750°C
2. Initial N₂ flow rate = 1000 sccm
3. Load wafers
4. Change N₂ flow rate to 2000 sccm
5. Ramp temperature up to 1050°C in 15 min
6. Stabilize temperature for 5 min
7. Anneal: N₂ = 2000 sccm, time = 1 hr
8. Ramp temperature down to 750°C in 5 min
9. End

A.22 Strip Top PSG

target: remove top PSG

equipment: wet sink

recipe highlights:

1. Wet wafer in DI water for 30 sec
2. Dip in 5:1 buffered HF until wafer dewet
3. rinse up to 10 MΩ·cm
4. Spin dry at 2000 rpm for 2 min

A.23 Second Poly Definition

target: 2 μm-thick patterned negative photoresist

equipments: Eaton wafer track, GCA Wafer Stepper, MTI Omnichuck Developer, Technics-c plasma etcher

recipe highlights:

1. Dehydrate at 120°C for 1 hr
2. Expose to HMDS vapor for 1 min
3. Spin on KTI 820 negative G-line photoresist: thickness = 2 μm

4. Soft bake with Eaton hot chuck at 120°C for 1 min
5. Expose with GCA Wafer Stepper: exposure time = 1.5× bright field
6. Post-exposure bake at 120°C for 1 min with Eaton hot chuck.
7. Develop with 2:1 KTI 934 developer in Omnichuck: time = standard
8. Hard bake at 120°C for > 5 hr

A.24 Second Poly Etch

target: pattern poly2 (etch rate $\approx 3200 \text{ \AA}\cdot\text{min}^{-1}$)

equipments: lam1, wet sink

recipe highlights:

1. Brief dip in 5:1 buffered HF to remove oxide
2. Rinse to 10 MΩ·cm in Sink8
3. Spin dry at 2000 rpm for 2 min
4. Lam1 etch: pressure = 280 mtorr, power = 300 W, gap = 1.5 cm, CCl₄ = 130 sccm, O₂ = 15 sccm, He = 130 sccm, time = 1 min
5. Idle: power = 0, gases flowing, time = 1 min
6. Repeat steps 4 and 5 six times
7. Overetch: 25% of total etch time

A.25 Clean and Sacrificial Etch

target: free structures

equipments: Technics-c, wet sinks

recipe highlights:

1. Photoresist ashing in Technics-c: O₂ = 50 sccm, power = 400 W, time = 10 min
2. Cleaning: piranha clean in Sink8 for 20 min, rinse in DI water up to 10 MΩ·cm
3. Final cleaning: piranha clean in Sink6 for 20 min, rinse in DI water up to 16 MΩ·cm
4. Sacrificial etch in 10:1 diluted HF: time = 2 hr
5. Final rinse with DI water to 16MΩ·cm
6. Dry under an IR lamp for 10 min

Appendix B C-PROGRAMMING SOURCE CODES

Appendix B is a collection of some selected C-programming source codes developed for laying out various novel planar structures suitable for KIC. The *GCA 3600 Pattern Generator* used at the Berkeley Microfabrication Laboratory is capable of exposing sequences of regular or rotated rectangles, which can be used to generate rounded or curved features in addition to the conventional Manhattan layout. The following C-source codes are designed to automate part of the layout process for complicated geometries.

B.1 Manhattan Archimedean Spiral

This program generates a KIC file of an Archimedean spiral with Manhattan boxes, the dimensions are specified by the user.

```
#include <stdio.h>
#include <math.h>

/* A program to generate spiral pattern in .kic format
 *
 * Input is the maximum radius, the number of turns
 * and the width of
 * the spiral.
 *
 * Output is a complete spiral.
 * Radius is R = (Ro - a * theta),
 * where theta is measured from positive x-axis.
 *
 * Written by William C. Tang, 6/30/88
 */
```

```
double thetal, theta2, alpha;
double rmax, rmin, turnnum, w;
double getxy();
int    j;
FILE *fptr;

main()
{
    double  r1;
    double  y0f, y1f;
    int     x0, y0, y1;
    int     xin;
    int     jj;
    int     tx = 0;
    int     ty = 0;
    int     xc, yc, dx, dy;
    int     xc0 = 0;
    int     yc0=0;
    int     dx0=0;
    int     dy0=0;
    char    a[10], inp[80];

    printf("\n\nA file \"spiral.k\""
           " will be created or overwritten.\n\n");
    printf("Enter maximum outer radius (um): ");
    gets(inp);
    rmax = atof(inp);

    printf("Enter minimum outer radius (um): ");
    gets(inp);
    rmin = atof(inp);

    printf("Enter number of turns (increments of 0.25): ");
    gets(inp);
    turnnum = atof(inp);

    printf("Enter spiral width (um): ");
    gets(inp);
    w = atof(inp);

    printf("Which layer? ");
```

```

scanf( "%s", a);

fptr = fopen( "spiral.k", "w" );

fprintf(fptr, "(Symbol spiral.k);\n");
fprintf(fptr, "9 spiral.k;\nDS 0 1 1;\nL %s;\n", a);

/* Initialization */

rmax *= 5.0;
rmin *= 5.0;
w *= 5.0;
alpha = (rmax-rmin)/(2.0*M_PI*turnnum);

for (j=0; j<turnnum*4.0 ; j++)
{
    r1 = rmax - j * alpha * M_PI/2.0;
    theta1 = 0.0;
    theta2 = 0.0;
    x0 = r1 - 0.5;
    xin = r1 - w - 0.5;
    while (x0 > -1 && xin > 0)
    {
        y0f = getxy(x0, r1, 0);
        if (x0 > xin)
        {
            y1f = 0.0;
        }
        else
        {
            y1f = getxy(x0, r1, 1);
        }
        y0 = y0f + 0.5;
        y1 = y1f + 0.5;

        jj = j % 4;
        switch (jj)
        {
        case 0:
            xc = x0 * 200 + 100;
            yc = (y0 + y1) * 100;
            dx = 200;

```

```
    dy = (y0 - y1) * 200;
    break;
case 1:
    xc = (y0 + y1) * -100;
    yc = x0 * 200 + 100;
    dx = (y0 - y1) * 200;
    dy = 200;
    break;
case 2:
    xc = x0 * -200 - 100;
    yc = (y0 + y1) * -100;
    dx = 200;
    dy = (y0 - y1) * 200;
    break;
case 3:
    xc = (y0 + y1) * 100;
    yc = x0 * -200 - 100;
    dx = (y0 - y1) * 200;
    dy = 200;
    break;
default :
    printf("Cannot identify remainder: %d\n", jj);
} /* endswitch */
if (dx == dx0 && xc == xc0)
{
    if (yc0>yc) {
        yc0 -= dy /2;
    } else {
        yc0 += dy /2;
    }
    dy0 += dy;
}
else
{
    if (dy == dy0 && yc == yc0)
    {
        if (xc0>xc) {
            xc0 -= dx /2;
        } else {
            xc0 += dx /2;
        }
        dx0 += dx;
    }
}
```

```

        else
        {
            fprintf(fptr, "B %d, %d, %d, %d;\n", dx0, dy0,
xc0, yc0);
            dy0 = dy;
            dx0 = dx;
            xc0 = xc;
            yc0 = yc;
        }
        x0 -= 1;
    }
}

fprintf(fptr, "B %d, %d, %d, %d;\n", dx0, dy0, xc0,
yc0);
fprintf(fptr, "DF;\nE");
fclose(fptr);

}

double getxy(x, rma, whe)
double rma;
int x, whe;
{
    double yf, dx, dtheta1, dtheta2;
    double r0, theta;
    double xx = rma;

    switch (whe) {
    case 0:
        r0 = rma;
        theta = theta1;
        break;
    case 1:
        r0 = rma - w;
        theta = theta2;
    }
}

```

```
        break;
    } /* endswitch */

dtheta1 = 0.5/r0;

while ((xx-x) > 0.5)
{
    thet += dtheta1;
    xx = (r0 - alpha * thet) * cos(theta);
}

dx = xx - (r0 - alpha * (thet-dtheta1)) *
cos(theta-dtheta1);

while ((x +0.5 -xx) > 1e-9 || (xx-x-0.5) > 1e-9)
{
    dtheta2 = dtheta1 * (x + 0.5 - xx)/dx;
    thet += dtheta2;
    xx = (r0 - alpha * thet) * cos(theta);
}

yf = (r0 - alpha * thet) * sin(theta);

switch (whe) {
case 0:
    theta1 = thet;
    break;
case 1:
    theta2 = thet;
    break;
} /* endswitch */

return (yf);
}
```

B.2 Rotated-Box Archimedean Spiral

This program generates a KIC file of an Archimedean spiral with rotated boxes, the dimensions are specified by the user.

```
/*      This program generate a number of four-sided
*
*      polygons to make up an achemidean spiral.
*      The user will input
*          spiral outer radius,
*          spiral inner radius,
*          beam width, and
*          number of turns.
*
*      This program also calculate the spiral length and
*      spring constants with given parameters.
*
*      Written by William C. Tang (tang@resonance)
*      University of California, Berkeley
*      10/23/89
*/
#include <stdio.h>
#include <math.h>

double w, t, y, r, ri, ro, alpha, theta;
double scaler, nt, nb, gap;
double l = 0.0;
double ktheta, k;
double dr, dr2, dc, dx;
double x, xa, xb, xc, xd;
double y, ya, yb, yc, yd;
double dtheta;

int xai, xbi, xci, xdi;
int yai, ybi, yci, ydi;
int i, n;
int count;

char a[10], b[10], c[10], d[10];

FILE *fptr;
```

```

main ()
{
    scaler = 1.0;
    printf("\n\nA clockwise archimedean spiral will be created
using 4-sided polygons.\n");
    printf("A file with specified name will be created or
overwritten if exists.\n\n");
    printf("Enter outer radius (um): ");
    scanf("%F", &ro);
    printf("Enter inner radius (um): ");
    scanf("%F", &ri);
    printf("Enter beam width (um):      ");
    scanf("%F", &w);
    printf("Enter # of turns:           ");
    scanf("%F", &nt);

    if (nt>0.999)
    {
        gap = (ro - ri)/nt - w;
        printf("\nGap between beams are %6.2f um.\n", gap);
    }

    printf("\nEnter thickness (um):      ");
    scanf("%F", &t);
    printf("Enter Young's modulus (N/um2, e.g., 0.15):      ");
    scanf("%F", &y);
    printf("Enter number of simulation points (e.g. 500): ");
    scanf("%d", &i);

    /* Initialization */

    dr      = (ro-ri)/i;
    dr2     = dr * dr;

    /* numerical integration */

    for (n=0; n<(i+1); n++)
    {
        r  = ro - dr * n;
        dc = (r * 2 * M_PI * nt) / i;
        dx = sqrt(dc*dc + dr2);
        l += dx;
    }
}

```

```

/* output */

printf("\nLength of Sprial is %8.2f um\n", l);
ktheta = (M_PI * y * t * w * w * w) /(l*0.002160);
k      = ktheta * 180 / (M_PI * ro * ro);
printf("k-theta is %11.4e (uN-um)/deg.\n", ktheta);
printf("k is      %11.4e uN/um\n", k);

/* continue */

printf("\nWhich layer for structure? ");
scanf("%s", a);
printf("Enter file name :           ");
scanf("%s", b);
printf("Enter increment angle (deg): ");
scanf("%F", &dtheta);
dtheta *= M_PI/180.0;

/* Open a file */

fptr = fopen(b, "w");
fprintf(fptr, "(Symbol %s);\n9 %s;\nDS 0 1 1;\nL
%s;\n", b, b, a);

/* Calculate initial parameters */

ri *= 1000.0/scaler;
ro *= 1000.0/scaler;
w *= 1000.0/scaler;
nb = nt*2*M_PI / dtheta;
dr = (ro - ri) / nb;

r = ro + dr;

xb = 0.0;
yb = r;

for (count=1; count<nb+2; count++)
{
    xa = xb; ya = yb;
    r -= dr;
}

```

```

x = xa; y = ya; turn(); xb = x; yb = y;

/* calculate alpha */

x = xb - xa;
y = yb - ya;

if (x > -0.1 && x < 0.1)
{
    if (y > 0.0) {alpha = M_PI /2.0;}
    else {alpha = -1.0* M_PI/ 2.0;}
}
else
{
    {
        alpha = atan(y/x);
        if (x < -0.1)
        {
            alpha += M_PI;
        }
    }
}

xc = xb + w * sin(alpha);
yc = yb - w * cos(alpha);

xd = xa + xc - xb;
yd = ya + yc - yb;

output();
}

/* closing lines */

fprintf(fptr, "DF;\nE\n");
fclose(fptr);
printf("Done!\n\n");
}

turn()

{
if (x > -0.1 && x < 0.1)
{

```

```
    if (y > 0.0) {theta = M_PI /2.0;}
    else {theta = -1.0* M_PI/ 2.0;}
}
else
{
    theta = atan(y/x);
    if (x < -0.1)
    {
        theta += M_PI;
    }
    theta -= dtheta;
    x = r * cos(theta);
    y = r * sin(theta);
}

output()
{
double fl;

if (xa < -0.1) {fl = -0.5;} else {fl = 0.5;}
xai = xa + fl;
if (xb < -0.1) {fl = -0.5;} else {fl = 0.5;}
xbi = xb + fl;
if (xc < -0.1) {fl = -0.5;} else {fl = 0.5;}
xci = xc + fl;
if (xd < -0.1) {fl = -0.5;} else {fl = 0.5;}
xdii = xd + fl;

if (ya < -0.1) {fl = -0.5;} else {fl = 0.5;}
yai = ya + fl;
if (yb < -0.1) {fl = -0.5;} else {fl = 0.5;}
ybi = yb + fl;
if (yc < -0.1) {fl = -0.5;} else {fl = 0.5;}
ycli = yc + fl;
if (yd < -0.1) {fl = -0.5;} else {fl = 0.5;}
ydi = yd + fl;

xai *= scaler;
xbi *= scaler;
xci *= scaler;
xdii *= scaler;
```

```
yai *= scaler;
ybi *= scaler;
yci *= scaler;
ydi *= scaler;

fprintf(fptr, "P %d %d %d %d %d %d %d;\n", xai, yai,
xbi, ybi, xci, yci, xdi, ydi);
}
```

B.3 Rotated-Box Concentric Comb Drive

This program generates a KIC file of a concentric comb drive with rotated boxes, the dimensions are specified by the user.

```
/*
 *      This program generate a number of four-sided
 *      polygons to make up a concentric comb fingers.
 *      The user will input
 *          # of fingers,
 *          overlap of the outer finger
 *          finger gap,
 *          finger width, and
 *          radius of curvature.
 *
 *      Written by William C. Tang (tang@janus)
 *      University of California, Berkeley
 *      10/17/89
 */

#include <stdio.h>
#include <math.h>

double w, w0, g, o, l, 10, r, r0, width, theta, alpha,
angle;
double scaler;
double x, xa, xb, xc, xd;
double y, ya, yb, yc, yd;

int nf, nt;
int xai, xbi, xci, xdi;
int yai, ybi, yci, ydi;
int count, count0;

char a[10], b[10], c[10], d[10];

FILE *fptr;

main ()
{
```

```

printf("A set of concentric comb finger will be created
using 4-sided\n");
printf("polygons. A file with specified name will be
created or\n");
printf("overwritten if exists.\n\n");
printf("Enter number of fingers:
");
scanf("%d", &nf);
printf("Enter finger length [out finger, 4 multiple] (um):
");
scanf("%F", &l);
printf("Enter finger overlap [out finger] (um):
");
scanf("%F", &o);
printf("Enter finger width (um):
");
scanf("%F", &w);
printf("Enter finger gap (um):
");
scanf("%F", &g);
width = (g *2 + w + 4)*(nf-1) + w;
printf("\nTotal comb width is %f um.\n\n", width);
printf("Enter radius of curvature [outmost finger] (um):
");
scanf("%F", &r);
/* printf("Enter minimum resolution (1 or multiple of 2 or
5): ");
scanf("%F", &scaler); */
scaler=1.0;

printf("\nWhich layer for structure?      ");
scanf("%s", a);
printf("Which layer for anchor?      ");
scanf("%s", c);
printf("Which layer for ground?      ");
scanf("%s", d);
printf("Enter file name :      ");
scanf("%s", b);
printf("\n\n");

/* Open a file */
```

```

fptr = fopen(b, "w");
fprintf(fptr, "(Symbol %s);\n9 %s;\nDS 0 1 1;\nL
%s;\n", b, b, a);

/* Calculate initial parameters */
```

$$\theta = 4.0 / r;$$

$$\alpha = (l-o) / r;$$

$$nt = l/4;$$

$$r *= 1000.0/scaler;$$

$$w *= 1000.0/scaler;$$

$$g *= 1000.0/scaler;$$

$$o *= 1000.0/scaler;$$

$$l *= 1000.0/scaler;$$

$$w0 = 4000.0/scaler;$$

$$r0 = r + w + w0 + 2*g;$$

$$/* printf("\nr0 is %f\n", r0); */$$

$$/* Generate movable fingers */$$

$$\text{for (count0=1; count0<(nf + 1); count0++)}$$

$$\{$$

$$r0-= (w + 2 * g + w0);$$

$$l0 = l * r0/(r*1000);$$

$$\text{printf("Finger #d is %f um\n", count0, l0);}$$

$$xa = 0.0;$$

$$ya = r0;$$

$$xb = r0 * sin(theta);$$

$$yb = ya - r0 * (1 - cos(theta));$$

$$xc = xb - w * (1-cos(theta))/(sqrt(2 - 2 * cos(theta)));$$

$$yc = yb - w * sin(theta) / (sqrt(2 - 2 * cos(theta)));$$

$$xd = xa - xb + xc;$$

$$yd = ya - yb + yc;$$

$$\text{output();}$$

$$\text{for (count=1; count<nt; count++)}$$

```

{
    angle = -1 * theta;
rotate();
output();
}
}

/* Generate stationary fingers */

r0 = r + w0*2 + w + g*3;
for (count0=1; count0<(2+nf); count0++)
{
    r0-= (w + 2 * g + w0);

    xa = 0.0;
    ya = r0;

    xb = r0 * sin(theta);
    yb = ya - r0 * ( 1 - cos(theta));

    xc = xb - w0 * (1-cos(theta))/(sqrt(2-2 * cos(theta)));
    yc = yb - w0 * sin(theta) / (sqrt(2-2 * cos(theta)));

    xd = xa - xb + xc;
    yd = ya - yb + yc;

    angle = -1* alpha;
rotate();
output();

for (count=1; count<nt; count++)
{
    angle = -1 * theta;
rotate();
output();
}
}

/* Generate anchors */

xa = 0.0;
ya = r + g + w0 * 2;

xb = 28000.0/scaler;

```

```

yb = ya;

xc = xb;
yc = ya - (nf + 1) * (w + 2 * g + w0) - w0 + g;

xd = 0.0;
yd = yc;

angle = (o - 2*l)/r;
rotate();
output();

fprintf(fptr, "L %s;\n", c);

xa = 4000.0/scaler;
ya = r + g + w0 * 2 - 4000.0/scaler;

xb = 24000.0/scaler;
yb = ya;

xc = xb;
yc = ya - (nf+1) * (w+2*g+w0) - w0 + g + 8000.0/scaler;

xd = xa;
yd = yc;

angle = (o - 2*l)/r;
rotate();
output();

/* generate ground */

fprintf(fptr, "L %s;\n", d);

theta = (l*2-o-10)/(20*r);
xa = (r + g + w0*2) * sin(theta);
ya = (r + g + w0*2) * cos(theta);

xb = xa;
yb = ya - (nf + 1) * (w + 2 * g + w0) - w0 + g;

xc = -1 * xa;

```

```

yc = yb;

xd = xc;
yd = ya;

output();

for (count=1; count<8; count++)
{
    angle = -2 * theta;
    rotate();
    output();
}

/* closing lines */

printf("\n\n");
fprintf(fptr, "DF;\nE\n");
fclose(fptr);
}

rotate()

{
x = xa; y = ya; turn(); xa = x; ya = y;
x = xb; y = yb; turn(); xb = x; yb = y;
x = xc; y = yc; turn(); xc = x; yc = y;
x = xd; y = yd; turn(); xd = x; yd = y;
}

turn()

{
double radius, gamma;
radius = sqrt(x*x + y*y);
if (x > -0.1 && x < 0.1)
{
    if (y > 0.0) {gamma = M_PI /2.0;}
    else {gamma = -1.0* M_PI/ 2.0;}
}
else
{
}
}

```

```
gamma = atan(y/x);
if (x < -0.1)
{
gamma += M_PI;
}
}
gamma += angle;
x = radius * cos(gamma);
y = radius * sin(gamma);

}

output()
{
double fl;

if (xa < -0.1) {fl = -0.5;} else {fl = 0.5;}
xai = xa + fl;
if (xb < -0.1) {fl = -0.5;} else {fl = 0.5;}
xbi = xb + fl;
if (xc < -0.1) {fl = -0.5;} else {fl = 0.5;}
xci = xc + fl;
if (xd < -0.1) {fl = -0.5;} else {fl = 0.5;}
xdci = xd + fl;

if (ya < -0.1) {fl = -0.5;} else {fl = 0.5;}
yai = ya + fl;
if (yb < -0.1) {fl = -0.5;} else {fl = 0.5;}
ybi = yb + fl;
if (yc < -0.1) {fl = -0.5;} else {fl = 0.5;}
yci = yc + fl;
if (yd < -0.1) {fl = -0.5;} else {fl = 0.5;}
ydi = yd + fl;

xai *= scaler;
xbi *= scaler;
xci *= scaler;
xdci *= scaler;

yai *= scaler;
ybi *= scaler;
yci *= scaler;
```

```
ydi *= scaler;  
  
fprintf(fptr, "P %d %d %d %d %d %d %d %d;\n", xai, yai,  
xbi, ybi, xci, yci, xdi, ydi);  
}
```

B.4 Manhattan Lateral Comb Drive

This program generates a KIC file of a lateral comb drive with Manhattan boxes, the dimensions are specified by the user.

```
/*      This program generate a kic file of lateral
*      structures with specified comb dimensions.
*      The user will input
*              # of comb fingers,
*              finger length, width, and gap.
*
*      Written by William C. Tang (tang@resonance)
*      University of California, Berkeley
*      10/24/89
*/
#include <stdio.h>
#include <string.h>
#include <math.h>

int num, length, width, gap;
int num1, num2;
int xc, yc, xd, yd, xc2, xd2;
int count;

char anum[20], alength[10], awidth[10], agap[10];
char alen1, alen2;
char all[50];

FILE *fptr;

main ()
{
    printf("Enter number of fingers (even # only): ");
    scanf("%s", anum);
    printf("Enter finger length (x10um): ");
    scanf("%s", alength);
    printf("Enter finger width (um): ");
    scanf("%s", awidth);
    printf("Enter finger gap (um): ");
}
```

```

scanf( "%s", agap);

/* Initialize */

num = atoi(anum);
length = atoi(alength);
width = atoi(awidth);
gap = atoi(agap);

num1 = num / 10;
num2 = num % 10;

strcat(all,"f");
strcat(all,anum);
strcat(all,"l");
strcat(all,alength);
strcat(all,"w");
strcat(all,awidth);
strcat(all,"g");
strcat(all,agap);
strcat(all,".k");

fptr = fopen(all,"w");
fprintf(fptr, "(Symbol %s);\n9 %s;\nDS 0 1 1;\n",all,
all);

/* Generate core */

fprintf(fptr, "9 ladimple.k;\nC 0 T 0 0;\n");
fprintf(fptr, "9 beam200.k;\nC 0 T 0 0;\n");
fprintf(fptr, "9 F.k;\nC0 T 280000 14000;\n");
fprintf(fptr, "9 a%d.k;\nC 0 T 298000 14000;\n", num1);
fprintf(fptr, "9 a%d.k;\nC 0 T 312000 14000;\n", num2);
fprintf(fptr, "9 L.k;\nC0 T 336000 14000;\n");
fprintf(fptr, "9 a%s.k;\nC 0 T 352000 14000;\n", alength);
fprintf(fptr, "9 W.k;\nC0 T 376000 14000;\n");
fprintf(fptr, "9 a%s.k;\nC 0 T 410000 14000;\n", awidth);
fprintf(fptr, "9 G.k;\nC 0 T 434000 14000;\n");
fprintf(fptr, "9 a%s.k;\nC 0 T 456000 14000;\n", agap);

yc = ( (num-1) * (4+2*gap+width) + 10 + width ) * 500;

fprintf(fptr, "9 marku.k;\nC 0 T 0 %d;\n", yc);

```

```

fprintf(fptr, "9 mark1.k;\nC 0 T 0 -%d;\n", yc);

/* Generate NI */

fprintf(fptr, "L NI;\n");

xd = 1000 * (1 + 15 * (length -1));
xc = 62000 + xd/2;
xd2 = 128000 + xd;
xc2 = 62000 + xd2/2;

yc += (gap + 8) * 1000;
if (yc > 94000)
{
    yc += 10000;
    fprintf(fptr, "B %d 20000 %d %d;\n", xd2, xc2, yc);
    fprintf(fptr, "B %d 20000 -%d %d;\n", xd2, xc2, yc);
    fprintf(fptr, "B %d 20000 %d -%d;\n", xd2, xc2, yc);
    fprintf(fptr, "B %d 20000 -%d -%d;\n", xd2, xc2, yc);
}
else
{
    yd = 114000 - yc;
    yc += yd/2;
    fprintf(fptr, "B %d %d %d %d;\n", xd2, yd, xc2, yc);
    fprintf(fptr, "B %d %d -%d %d;\n", xd2, yd, xc2, yc);
    fprintf(fptr, "B %d %d %d -%d;\n", xd2, yd, xc2, yc);
    fprintf(fptr, "B %d %d -%d -%d;\n", xd2, yd, xc2, yc);
}

fprintf(fptr, "B %d 228000 %d 0;\n", xd, xc);
fprintf(fptr, "B %d 228000 -%d 0;\n", xd, xc);

xc += xd/2 + 78000;

fprintf(fptr, "B 100000 100000 %d 64000;\n", xc);
fprintf(fptr, "B 100000 100000 -%d 64000;\n", xc);
fprintf(fptr, "B 100000 100000 %d -64000;\n", xc);
fprintf(fptr, "B 100000 100000 -%d -64000;\n", xc);

/* Generate ND */

fprintf(fptr, "L ND;\n");

```

```

fprintf(fptr, "B 60000 12000 0 0;\n");
fprintf(fptr, "B 14000 44000 37000 0;\n");
fprintf(fptr, "B 14000 44000 -37000 0;\n");

yd = ( (num - 1) * (4+2*gap+width) + 6 + width ) * 1000;

fprintf(fptr, "B 10000 %d 49000 0;\n", yd);
fprintf(fptr, "B 10000 %d -49000 0;\n", yd);

yd += (8 + 2 * gap) * 1000;
xc = (62 + length * 15) * 1000;

fprintf(fptr, "B 16000 %d %d 0;\n", yd, xc);
fprintf(fptr, "B 16000 %d -%d 0;\n", yd, xc);

xc += 82000;

fprintf(fptr, "B 150000 16000 %d 0;\n", xc);
fprintf(fptr, "B 150000 16000 -%d 0;\n", xc);

/* Generate fingers */

xc = (54 + length * 5) * 1000;
xc2 = xc + length * 5000;

fprintf(fptr, "B %s0000 4000 %d 0;\n", alength, xc2);
fprintf(fptr, "B %s0000 4000 -%d 0;\n", alength, xc2);

for (count=0; count < num/2; count++)
{
    yc = (4+2*gap+width+2*count * (4+2*gap+width) ) * 500;
    fprintf(fptr, "B %s0000 %s000 %d %d;\n", alength, awidth,
            xc, yc);
    fprintf(fptr, "B %s0000 %s000 %d -%d;\n", alength,
            awidth, xc, yc);
    fprintf(fptr, "B %s0000 %s000 -%d %d;\n", alength,
            awidth, xc, yc);

    yc += (2*gap + 4 + width) * 500;
    fprintf(fptr, "B %s0000 4000 %d %d;\n", alength, xc2,
            yc);
}

```

```
    fprintf(fptr, "B %s0000 4000 %d -%d;\n", alength, xc2,
yc);
    fprintf(fptr, "B %s0000 4000 -%d %d;\n", alength, xc2,
yc);
    fprintf(fptr, "B %s0000 4000 -%d -%d;\n", alength, xc2,
yc);
}

/* Generate NM */

fprintf(fptr, "L NM;\n");

xc = (142 + length * 15) * 1000;
fprintf(fptr, "B 158000 8000 %d 0;\n", xc);
fprintf(fptr, "B 158000 8000 -%d 0;\n", xc);

yd = ( (num-1) * (4+2*gap+width) + 6 + width ) * 1000;
yd += (2 * gap - 4) * 1000;
xc = (62 + length * 15) * 1000;

fprintf(fptr, "B 8000 %d %d 0;\n", yd, xc);
fprintf(fptr, "B 8000 %d -%d 0;\n", yd, xc);

/* Closing lines */

fprintf(fptr, "DF;\nE\n");
fclose(fptr);
}
```

B.5 Manhattan-to-Rotated-Box Conversion

This program generates a KIC file of the rotated results of a layout with Manhattan boxes.

```
/*
 *      This program generate a number of four-sided
 *      polygons to represent the rotated results of
 *      a kic file.
 *
 *      Written by William C. Tang (tang@resonance)
 *      University of California at Berkeley
 *      4/7/89
 *      11/14/89
 */

#include <stdio.h>
#include <math.h>

double ang, angle;
double x, x1, x2, x3, x4;
double y, ya, y2, y3, y4;

int xc, yc, dx, dy;
int xli, x2i, x3i, x4i;
int yli, y2i, y3i, y4i;
int ni, count;
int xln, x2n, x3n, x4n;
int yln, y2n, y3n, y4n;

char a[20];
char b[20];
char line[512];
char key[16], semi[16];

FILE *fptri, *fptro;

main ()
{
    printf("A set of polygons representing the rotated results
of\n");
    printf("a kic file will be created and written to a
specified file.\n");
}
```

```

printf("Enter input file name:   ");
scanf("%s", a);
fptri = fopen(a, "r");

printf("Enter output file name:  ");
scanf("%s", a);
fptro = fopen(a, "w");

printf("Enter increment angle (deg):  ");
scanf("%F", &angle);
angle *= M_PI/180.0;

printf("Enter # of increments:           ");
scanf("%d", &ni);

/* printf("Enter layer name:           ");
scanf("%s", b); */

/* initialize */

fprintf(fptro, "(Symbol %s);\n9 %s;\nDS 0 1 1;\n", a, a);

fgets(line,512,fptri);
fgets(line,512,fptri);
fgets(line,512,fptri);

while(fgets(line,512,fptri) != NULL)
{
    if (line[0] == 'P')
    {
        polytran();
        for (count=1; count<(ni+1); count++)
        {
            rotate();
            output();
        }
    }

    else if (line[0] == 'B')
    {
        translate();
        for (count=1; count<(ni+1); count++)
    }
}

```

```

        {
        rotate();
        output();
        }
    }

else
{
fprintf(fptro, "%s", line);
}
}

/* fprintf(fptro, "DF;\nE\n" ); */

fclose(fptro);

printf( "\n          Done! \n" );

}

translate( )

{

sscanf(line, "%s %d %d %d %d %s", key, &dx, &dy, &xc, &yc,
semi);
x1 = xc + dx/2;
ya = yc + dy/2;

x2 = x1;
y2 = yc - dy/2;

x3 = xc - dx/2;
y3 = y2;

x4 = x3;
y4 = ya;

}

polytran( )

```

```

{

    sscanf(line, "%s %d %d %d %d %d %d %s", key, &xln,
    &yln, &x2n, &y2n, &x3n, &y3n, &x4n, &y4n, semi);
/*   printf("line is %s %d %d %d %d %d %d %d%s", key, xln,
yln, x2n, y2n, x3n, y3n, x4n, y4n, semi);
*/
}

x1 = xln ; ya = yln;
x2 = x2n ; y2 = y2n;
x3 = x3n ; y3 = y3n;
x4 = x4n ; y4 = y4n;
}

rotate()

{
    x = x1; y = ya; turn(); x1 = x; ya =y;
    x = x2; y = y2; turn(); x2 = x; y2 =y;
    x = x3; y = y3; turn(); x3 = x; y3 =y;
    x = x4; y = y4; turn(); x4 = x; y4 =y;
}

turn( )

{
double radius, gamma;
    radius = sqrt (x*x + y*y);
    if (x > -0.1 && x < 0.1)
    {
        if (y > 0.0) {gamma = M_PI /2.0;}
        else {gamma = -1.0* M_PI/ 2.0;}
    }
    else
    {
        gamma = atan(y/x);
        if (x < -0.1)
        {
            gamma += M_PI;
        }
    }
}

```

```
gamma += angle;
x = radius * cos(gamma);
y = radius * sin(gamma);
}

output()
{
    double fl;

    if (x1 < -0.1) {fl= -0.5;} else {fl=0.5;}
    x1i = x1 + fl;
    if (x2 < -0.1) {fl= -0.5;} else {fl=0.5;}
    x2i = x2 + fl;
    if (x3 < -0.1) {fl= -0.5;} else {fl=0.5;}
    x3i = x3 + fl;
    if (x4 < -0.1) {fl= -0.5;} else {fl=0.5;}
    x4i = x4 + fl;

    if (ya < -0.1) {fl= -0.5;} else {fl=0.5;}
    y1i = ya + fl;
    if (y2 < -0.1) {fl= -0.5;} else {fl=0.5;}
    y2i = y2 + fl;
    if (y3 < -0.1) {fl= -0.5;} else {fl=0.5;}
    y3i = y3 + fl;
    if (y4 < -0.1) {fl= -0.5;} else {fl=0.5;}
    y4i = y4 + fl;

    fprintf(fptro, "P %d %d %d %d %d %d %d %d;\n", x1i, y1i,
x2i, y2i, x3i, y3i, x4i, y4i);
}
```

B.6 Rotated-Box Sawtooth

This program generates a KIC file of a set of sawtooth for resonant micromotors, the dimensions are specified by the user.

```
/*      This program generate a number of four-sided
*      polygons to make up the sawteeth of a circular
*      blate. The user will input
*          # of teeth,
*          half distance between the tips of two
*          adjacent teeth (stroke),
*          tooth top flat width, and
*          outer and inner radii of supporting ring.
*      The program then report the corresponding
*          addendum radius,
*          dedendum radius, and
*          tooth height.
*      The user will then be asked to decide whether to
*      continue with the generation.
*
*      Written by William C. Tang (tang@janus)
*      University of California, Berkeley
*      4/5/89
*/
#include <stdio.h>
#include <math.h>

double ra, rd, stroke, height, theta, alpha, flat, angle;
double x, xa, xb, xc, xd, xe, xf, xg;
double y, ya, yb, yc, yd, ye, yf, yg;
double xh, xi, xj, xk;
double yh, yi, yj, yk;
double rin, rout, scaler;

int nt, ns;
int xai, xbi, xci, xdi, xei, xfi, xgi;
int yai, ybi, yci, ydi, yei, yfi, ygi;
int xhi, xii, xji, xki;
int yhi, yii, yji, yki;
int count;
```

```

char a[10], b[10];

FILE *fptr;

main ()
{
    printf("A set of sawteeth will be generated using rectangular\n");
    printf("polygons. A file with specified name will be created or\n");
    printf("overwritten if exists.\n\n");
    printf("Enter number of teeth (multiple of 4 only): ");
    scanf("%d", &nt);
    printf("Enter stroke length (um): ");
    scanf("%F", &stroke);

    /* Calculate initial parameters */ /*

    theta = 2 * M_PI / nt;
    ra = stroke / sin(theta);
    rd = stroke / tan(theta);
    height = ra - rd;

    printf("\n\n stroke is (um) %f \n", stroke);
    printf("\n\n Addendum radius is (um) %f \n", ra);
    printf(" Dedendum radius is (um) %f \n", rd);
    printf(" theta is %f \n", theta);
    printf(" Tooth height is (um) %f \n\n", height);
    printf(" ctrl-c to quit.\n\n");
    printf("Enter tooth flat top width (um): ");
    scanf("%F", &flat);
    printf("Enter ring outer radius (um): ");
    scanf("%F", &rout);
    printf("Enter ring inner radius (um): ");
    scanf("%F", &rin);
    printf("Enter number of spokes: ");
    scanf("%d", &ns);
/* printf("Enter minimum resolution (1 or multiple of 2 or 5): ");
 */
    scanf("%F", &scaler); */

    scaler=1.0;
}

```

```
printf("\nWhich layer? ");
scanf("%s", a);
printf("\nEnter file name :");
scanf("%s", b);

/* Open a file */  

fptr = fopen(b,"w");
fprintf(fptr, "(Symbol %s);\n9 %s;\nDS 0 1 1;\nL
%s;\n",b, b, a);

/* Calculate first teeth coordinates */  

ra *= 1000.0/scaler;
rd *= 1000.0/scaler;
flat *= 1000.0/scaler;
rin *= 1000.0/scaler;
rout *= 1000.0/scaler;

xa = ra;
ya = 0.0;

xb = ra;
yb = -1.0 * flat;

xc = 0.9 * rd;
yc = -1.0 * flat;

xd = 0.9 * rd;
yd = 0.0;

output();

for (count=1; count<nt; count++)
{
    angle = theta;
    rotate();
    output();
}

xc = rd * cos(theta);
yc = -rd * sin(theta);
```

```
xb = ra;
yb = -1.0 * flat;

xa = ra - flat * (yb-yc) / (xb-xc);
ya = 0.0;

xc -= (xb - xc)/2;
yc -= (yb - yc)/2;

xd = xc + xa - xb;
yd = yc + ya - yb;

output();

for (count=1; count<nt; count++)
{
    angle = theta;
rotate();
output();
}

xc = rd * 0.9;
yc = 0.0;

angle = theta;
x = xc; y = yc; turn(); xd = x; yd = y;

xb = rd * 0.99;
yb = (xc - xd) * (xb - xc) / yd;

xa = xb - xc + xd;
ya = yb + yd;

output();

for (count=1; count<nt; count++)
{
    angle = theta;
rotate();
output();
}

/* add ring */
```

```

xb = rout;
yb = 0.0;

xa = rout * cos(M_PI/18.0);
ya = rout * sin(M_PI/18.0);

xc = rin;
yc = (xa - xb) * (xb - xc) / ya;

xd = xc + xa - xb;
yd = ya + yc;

output();

for (count=1; count<36; count++)
{
    angle = M_PI/18.0;
rotate();
output();
}

/* add spokes */

xb = rd;
yb = 0.0;

ya = 5000.0/scaler;
xa = sqrt(rd * rd - ya * ya);

xc = (rout + rin) / 2.0;
yc = (xa - xb) * (xb - xc) / ya;

xd = xc + xa - xb;
yd = ya + yc;

output();

for (count=1; count<ns; count++)
{
    angle = 2.0 * M_PI/ns;
rotate();
output();
}

```

```
/* closing lines */

    fprintf(fptr, "DF;\nE\n");
    fclose(fptr);
}

rotate()

{
    x = xa; y = ya; turn(); xa = x; ya = y;
    x = xb; y = yb; turn(); xb = x; yb = y;
    x = xc; y = yc; turn(); xc = x; yc = y;
    x = xd; y = yd; turn(); xd = x; yd = y;
}

turn()

{
    double radius, gamma;
    radius = sqrt(x*x + y*y);
    if (x > -0.1 && x < 0.1)
    {
        if (y > 0.0) {gamma = M_PI /2.0;}
        else {gamma = -1.0* M_PI/ 2.0;}
    }
    else
    {
        gamma = atan(y/x);
        if (x < -0.1)
        {
            gamma += M_PI;
        }
    }
    gamma += angle;
    x = radius * cos(gamma);
    y = radius * sin(gamma);

}

output()
{
    double fl;
```

```
if (xa < -0.1) {fl = -0.5;} else {fl = 0.5;}
xai = xa + fl;
if (xb < -0.1) {fl = -0.5;} else {fl = 0.5;}
xbi = xb + fl;
if (xc < -0.1) {fl = -0.5;} else {fl = 0.5;}
xci = xc + fl;
if (xd < -0.1) {fl = -0.5;} else {fl = 0.5;}
xdii = xd + fl;

if (ya < -0.1) {fl = -0.5;} else {fl = 0.5;}
yai = ya + fl;
if (yb < -0.1) {fl = -0.5;} else {fl = 0.5;}
ybi = yb + fl;
if (yc < -0.1) {fl = -0.5;} else {fl = 0.5;}
yci = yc + fl;
if (yd < -0.1) {fl = -0.5;} else {fl = 0.5;}
ydi = yd + fl;

xai *= scaler;
xbi *= scaler;
xci *= scaler;
xdii *= scaler;

yai *= scaler;
ybi *= scaler;
yci *= scaler;
ydi *= scaler;

fprintf(fptr, "P %d %d %d %d %d %d %d %d;\n", xai, yai, xbi,
ybi, xci, yci, xdii, ydi);
}
```